Engineering the electronic structure of lanthanide based materials

Edith Rogers

Engineering the electronic structure of lanthanide based materials

Proefschrift

ter verkrijging van de graad van doctor

aan de Technische Universiteit Delft,

op gezag van de Rector Magnificus prof. ir. K.C.A.M. Luyben,

voorzitter van het College voor Promoties,

in het openbaar te verdedigen op dinsdag 18 december 2012 om 15.00 uur

door Edith Grace ROGERS

Master in Physics, University of Wales

geboren te Newtown, Verenigd Koninkrijk.

Dit proefschrift is goedgekeurd door de promotor:

Prof. dr. P. Dorenbos

Copromotor   Dr. ir. E. van der Kolk

Samenstelling promotiecommissie:

Rector Magnificus,   voorzitter

Prof. dr. P. Dorenbos,	Technische Universiteit Delft, promotor
Dr. ir. E. van der Kolk,	Technische Universiteit Delft, copromotor
Prof. dr. D. Poelman,	Universiteit van Gent, België
Prof. dr. A. Meijerink,	Universiteit Utrecht
Prof. dr. F.M. Mulder,	Technische Universiteit Delft
Prof. dr. LDA Siebbeles,	Technische Universiteit Delft
Dr. H.J.T.M. Hintzen,	Technische Universiteit Eindhoven

For my Family

Contents

Chapter 1: Introduction

1.1. Motivation

We live in a world of electronics. Our lives are augmented (or not) by information collected, processed and displayed on an ever increasing array of devices, everything from radios, to televisions, to mobile phones and personal computers of varying size and type. These devices need to be powered, frequently need complex electronics and often have screens and speakers. Many of these things currently contain or could in future contain lanthanide based compounds. The lanthanides, the elements Lanthanum (La), Cerium (Ce), Praseodymium (Pr), Neodymium (Nd), Promethium (Pm), Samarium (Sm), Europium (Eu), Gadolinium (Gd), Terbium (Tb), Dysprosium (Dy), Holmium (Ho), Erbium (Er), Thulium (Tm), Ytterbium (Yb) and Lutetium (Lu), are elements with a nominally 3+ valency, although compounds containing 4+, notably Ce, and 2+, notably Eu, ions are also found. Lanthanides are found in phosphors used in light emitting diodes (LEDs) and cathode ray tube (CRT) monitors, and in rare earth magnets used in headphones and speakers and hard drives. Certain lanthanide based compounds are potential spintronics materials, which could have future uses in computer memories [1, 2], while others could be used to increase the efficiency of solar cells [3]. An important, if less everyday use for lanthanide based materials is for use in scintillators for radiation detection, whether this is for medical imaging, security or scientific purposes.

However, and partly because of, their usefulness, the lanthanides are quite expensive. In addition compounds, particularly those with unusual Ln ion valencies, can be difficult and time consuming to produce. Therefore it is important to be able to model the optical properties and electronic structures of lanthanide based materials, so as to be able to screen these properties, so that research may be focused on materials with the desired properties, rather than through pure trial and error.

The optical properties of lanthanide based compounds have been investigated experimentally and various diagrams and models have been developed in order to characterize them. The empirical model described in references [4] and [5] can successfully predict the energy of interband optical transitions of lanthanide doped compounds used as phosphors and scintillators [4, 5]. In 2006 the model was applied to the binary lanthanide oxides and the lanthanide monosulfides [6]. It was shown that given relatively little information on one compound in a series, i.e. the lanthanide sesquioxides: La_2O_3, Ce_2O_3… Yb_2O_3, Lu_2O_3, it was possible not only to predict the optical bandgap of a compound but to determine what transition was responsible. The model could also predict whether a material will be a semiconductor or a metal, or if it is theoretically stable.

In this thesis, the motivation is to explore this relationship between optical and material properties still further, by showing that it is possible to predict material properties of new lanthanide materials from the optical properties of existing ones. The motivation was then to understand how we can manipulate the electronic structure by exploiting the crystal field splitting of the lanthanide 5d band and changing the 4f→5d optical gap, in particular looking at switchable materials such as SmS whose material properties and optical spectra change due to changes in the electronic structure caused by a perturbation in the material's environment. Scientifically the motivation was to try to understand these compounds further through knowledge of the change in their optical properties and thus electronic structure. Technologically the aim was to show that by manipulating their electronic structure, compounds such as SmS could be applied as energy-saving devices or as switchable glazing.

1.2. Bandgaps in Ln based compounds

The optical properties of binary lanthanide based materials are dominated by the anion mp band (m=2, 3, 4 or 5) and the lanthanide 4f and 5d bands. The

anion mp band, where m is 2 for F, O and N, 3 for Cl, S and P, 4 for Br, Se and As, and 5 for I, Te and Sb, makes up the valence band (VB) of most lanthanide based materials. As m increases, that is, we go down the columns of the periodic table, the electronegativity of the anion decreases. In chapter four it will be shown that this causes the mp→5d and the mp→4f bandgaps to decrease in energy.

The 4f bands of lanthanide (Ln) based compounds are well shielded and are not affected by the crystalline environment. The 5d band forms the conduction band (CB) of the lanthanide based materials studied. Unlike the 4f band, it is strongly affected by the crystalline environment.

In figure 1.1 a scheme is shown that displays the relative energies of the F 2p valence band at energy 0 and the lanthanide 4f and 5d bands as a function of the lanthanide ion for LnF_3. The diagram shows the relative energy difference between the top of the F 2p valence band and the top of the occupied Ln 4f(3+) ground state, the top of the unoccupied Ln 4f(2+) ground state and the bottom of the Ln 5d conduction band. A more detailed explanation of the construction and evaluation of the scheme can be found in chapters 2 and 3.

Four different types of transition are shown in the figure. The first type, seen for LaF_3, GdF_3 and LuF_3, is the 2p→5d transition (solid red arrow), where an electron is excited from the valence band to the 5d conduction band. This transition is observed in compounds with a nominal Ln(3+) ion such as GdF_3, Lu_2S_3 and LaN. The second transition observed is the lanthanide $4f^n$→$4f^{n-1}5d^1$ transition (dashed blue arrow), seen here for CeF_3, PrF_3, NdF_3, PmF_3, TbF_3, DyF_3, HoF_3 and ErF_3. This transition is seen for lanthanide compounds with either a 2+ or a 3+ valency. It is this transition that is of interest for much of this thesis. The third type of transition seen is a 2p→4f(2+) transition (dotted green arrow), where an electron is excited from the 2p valence band to the $4f^n$ shell of Ln^{3+} to create the $4f^{n+1}$ ground state of Ln^{2+} denoted as 4f(2+). In the case of the fluorides, this transition is seen for EuF_3 and YbF_3. More generally, this transition is found in series of compounds with either a nominally Ln 3+ or

4+ valency. The final transition shown for the lanthanide fluorides is a possible interlanthanide charge transfer $Sm^{3+}+Sm^{3+}\rightarrow Sm^{4+}Sm^{2+}$ transition (dot-dashed violet arrow), which is shown for SmF_3 and TmF_3. This transition is not to be confused with the spin forbidden intralanthanide 4f→4f transition seen in many lanthanide compounds.
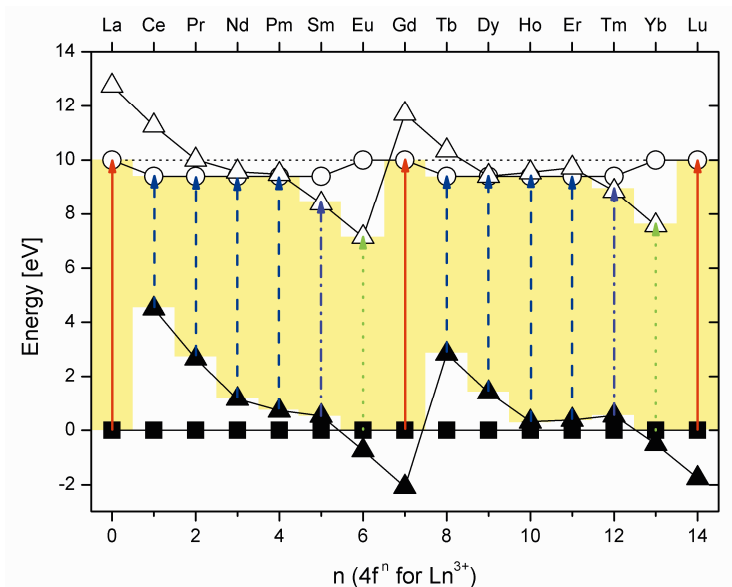
Figure 1.1. Predicted electronic structures of the Ln trifluorides (LnF_3) from [7]: yellow shading = optical bandgap, squares = 2p-VB, circles = 5d-CB, and triangles = 4f ground state. Filled symbols indicate an occupied band. Red arrows indicate a 2p→5d transition, blue dashed (---) arrows indicate a 4f→5d transition, green dotted (⋯) arrows indicate a 2p→4f transition and purple dot-dash arrows (·-·-) indicate a 4f→4f transition

Changes in the crystalline environment affect the energy difference between the mp, 4f and 5d bands. As can be seen in figure 1.1, as we change the Ln ion, the 5d band remains fairly constant in energy relative to the valence band, but the 4f levels follow a distinctive zigzag pattern. This is because a 4f electron is well shielded from its crystalline environment and the zig-zag pattern is entirely due to interactions within the 4f shell. However a 5d electron has a very strong interaction with its crystalline environment, yet for each lanthanide

it is about the same, which leads to a fairly constant energy with change of lanthanide.

As we change anion, the energy difference between the valence band and the 4f and 5d bands changes. As the electronegativity decreases (period (*m*) increases, group decreases), the energy difference between the *m*p and the 4f or 5d bands also decreases. This is shown in more detail in chapter 4.

The difference between the 4f and the 5d bands shows different behaviour. The first consideration is due to the nephelauxetic effect. That is the energy of the d-electron decreases as the ability to form covalent bonds between the ligand and the metal ion increases. This leads to a decrease in the energy difference between the 5d and *m*p bands.

The second consideration is the crystal field splitting. The 5d band energy is strongly affected by its crystalline environment. This causes the otherwise degenerate energy levels to split, depending on the crystal field symmetry. By altering the crystalline environment, the crystal field splitting of the 5d band is altered, so that the energy of the bottom of the 5d band shifts relative to the 4f ground state.

It is the crystal field splitting that is most important regarding switchable lanthanide based materials. These materials, notable examples being SmS and TmTe, have been of both scientific and technological interest for over forty years now. These materials can exhibit a valence change after a perturbation in their environment due to the proximity of their $4f^n$ ground state to the 5d conduction band.

1.3. Ln based switchable materials

The proximity of the 4f(2+) ground state to the bottom of the 5d band of a lanthanide based switchable material affects how easily it switches under pressure. By altering the crystal field splitting of a Ln ion we can change the 4f→5d energy gap and therefore the perturbation required in order to switch a compound from the semiconducting to the metallic state. Figure 1.2 shows the bandgap of several lanthanide compounds that exhibit switching between a

semiconductor and a metal under pressure. There is no general correlation between bandgap and switching pressure. However, the most comprehensively investigated of the switchable materials shown, the Sm monochalcogenides, SmS, SmSe and SmTe, show an increase in the pressure required to switch from the semiconducting to the metallic phase with bandgap [8]. TmTe appears to be quite similar in its behaviour [9]. Of the Sm and Tm monochalcogenides, only SmS undergoes a discontinuous phase transition between the semiconducting and a metallic phase. Also shown are CeP and NdI_2, two other switchable materials, although both quite different to the Sm and Tm monochalcogenides. CeP has the same face centred cubic (FCC) NaCl type structure as SmS and also undergoes a discontinuous change in valence under pressure; however, the change is from the 3+ to the 4+ state of the Ce ion and occurs at much higher pressures [10, 11]. The Nd ion in NdI_2 switches from a 2+ to a 3+ state under pressure, probably discontinuously, but this time the transition is not isostructural [12]. EuO and the Ytterbium monochalcogenides (not shown) also undergo a continuous semiconductor to metal phase transition under pressure but the pressures required are far higher, and the transition range is longer [13].

Other compounds may be switchable but have not been studied in this way, or display unusual behaviour that might suggest a valence transition. Of these, DyI_2 is the compound for which there is the most evidence to suggest that it is switchable. In 1980 a paper was published by Friedt *et al* that showed some unusual behaviour in samples of DyI_2 contaminated by traces of DyI_3 and DyOI [14]. This sample, unlike pure DyI_2, appeared metallic at room temperature, but upon cooling to 260K became semiconducting.

PrI_2, most probably has an interconfigurational valence but, depending on synthesis conditions, both semiconducting and metallic versions have been synthesized [15]. $NdCl_2$ and $NdBr_2$, as will be shown later on in this thesis, have very similar electronic structures to NdI_2, and $DyCl_2$ and $DyBr_2$ are likewise similar in electronic structure to DyI_2. It is possible, although

structural considerations have to be taken into account, that these compounds might also be switchable under the right conditions.
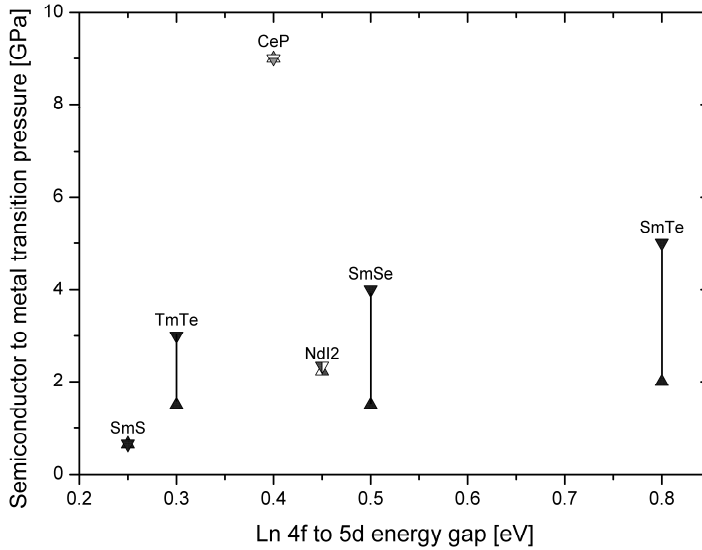
Figure 1.2. 4f→5d optical bandgap versus semiconductor to metal transition pressure of: the Sm and Tm monochalcogenides- SmS, SmSe, SmTe and TmTe [8, 9], CeP [11], NdI$_2$ [12]. 4f→5d energies are from [7].

1.3.1 Switching in SmS

Of all the compounds mentioned above, SmS is the most famous as a switchable material. The valence change under pressure was first observed, along with those of SmSe and TmSe, by Jayaraman in 1970 [8], although Zhuze *et al* had already noticed that when polished, the surface of SmS crystals turned a golden colour, back in 1964 [16].

SmS, in its bulk form, is a black semiconductor with a NaCl type structure. It has a lattice constant of 597pm and a bandgap of around 0.25eV. Upon the application of hydrostatic pressure it switches discontinuously and isostructurally to a metallic form with a lattice constant of only 563pm. With the change in valency, the electrical, magnetic, thermal and optical properties also change. In chapter five the change in lattice constant and optical

absorption and transmission between semiconducting and metallic SmS in thin film form will be discussed in more detail.

1.4. Aims

The aim of this thesis is to explore how the optical properties and electronic structures of binary lanthanide based compounds can be predicted using an empirical model, studied using optical spectroscopy and manipulated by changing the environment of a compound, so that the 4f to 5d energy gap is reduced.

1.5. Thesis outline

In chapters 2 to 4 of this thesis the optical properties and electronic structure of binary lanthanide based compounds will be examined using an empirical model. In chapter 2 the model will be introduced while in chapter 3 the results from applying the model to the binary lanthanide halide, chalcogenides and pnictides with 2+, 3+ and 4+ valencies, will be shown and discussed. Finally in chapter 4, trends in the data modelled for these compounds will be discussed.

In chapter 5 we will look at one of the families of compounds studied in chapters 2 to 4, the lanthanide diiodides, in more detail, by measuring their optical $4f{\rightarrow}5d$ bandgaps and comparing the results with the predictions of the empirical model.

In chapters 6, 7 and 8, the emphasis changes more towards manipulation of the 4f to 5d energy gap. In chapter 6, we will look at how increasing the level of EuN dopants in $EuO_{1-x}N_x$ affects the lattice constant and $4f{\rightarrow}5d$ bandgap, while in chapter 7 we will look at the temperature dependent metal to semiconductor phase transition of the switchable lanthanide based material, SmS.

Finally in chapter 8 we will look at the fabrication of SmS thin films by the RF magnetron co-sputtering of Sm and Sm_2S_3 and show how changes in the sputtering conditions affects the lattice parameters and Sm valency of the films.

References

[1]   Gregg J F 2007 *Nature Materials* **6** 798-9

[2]   Schmehl A, Vaithyanathan V, Herrnberger A, Thiel S, Richter C, Liberati M, Heeg T, Röckerath M, Kourkoutis L F, Mühlbauer S, Böni P, Muller D A, Barash Y, Schubert J, Idzerda Y, Mannhart J and Schlom D G 2007 *Nature Materials* **6** 882-7

[3]   ten Kate O M, Hintzen H T, Dorenbos P and van der Kolk E 2011 *J. Mater. Chem.* **21** 18289-94

[4]   Dorenbos P 2003 *Journal of Physics: Condensed Matter* **15** 8417-34

[5]   Dorenbos P, Krumpel A H, van der Kolk E, Boutinard P, Bettinelli M and Cavalli E 2010 *Optical Materials*

[6]   van der Kolk E and Dorenbos P 2006 *Chemistry of Materials* **18** 3458-62

[7]   Rogers E, Dorenbos P and van der Kolk E 2011 *New Journal of Physics* **13** 093038

[8]   Jayaraman A, Narayanamurti V, Bucher E and Maines R G 1970 *Physical Review Letters* **25** 1430-3

[9]   Chatterjee A, Singh A K and Jayaraman A 1972 *Physical Review B* **6** 2285-91

[10]   Jayaraman A, Lowe W, Longinotti L D and Bucher E 1976 *Physical Review Letters* **36** 366-8

[11]   Léger J-M, Vedel I and Redon A-M 1987 *Journal of Magnetism and Magnetic Materials* **63-64** 49-51

[12]   Beck H P and Schuster M 1992 *Journal of Solid State Chemistry* **100** 301-6

[13]   Jayaraman A, Singh A K, Chatterjee A and Devi U S 1974 *Physical Review B* **9** 2513-20

[14]   Friedt J M, MacCordick J, Sanchez J P and Rebizant J 1980 *Solid State Communications* **35** 1021-4

[15]   Gerlitzki N, Meyer G, Mudring A-V and Corbett J D 2004 *Journal of Alloys and Compounds* **380** 211-8

[16]   Smirnov I A and Oskotskii V S 1978 *Soviet Physics Uspekhi* **21** 117-40

Chapter 2: An empirical model for the optical and electronic properties of binary Lanthanide compounds

*This chapter has been published as part of E. Rogers, P. Dorenbos, E. van der Kolk, Systematics in the optical and electronic properties of the binary lanthanide halide, chalcogenide and pnictide compounds – an overview, New Journal of Physics, **13**, 093038, 2011*

2.1. Introduction

The binary lanthanide compounds have been the subject of numerous theoretical and experimental investigations because they show a rich variation in electrical, optical and magnetic properties. The technological importance of lanthanide based materials is apparent from a multitude of applications ranging from catalysts [1, 2] and magnets [3] to laser host crystals [4], transparent ceramics [5-9] and phosphors [9-13], while more recently binary materials such as $CeBr_3$ have shown the potential to become excellent scintillator materials for the detection of ionizing radiation [14-16]. They have also been considered for future applications based on spintronics [17, 18] or for high-density optical or magnetic data storage [19]. Binary lanthanide compounds also serve as precursors in the synthesis of more complex ternary or quaternary lanthanide materials that have found applications in a variety of photonic applications such as lasers [20], wide bandgap electroluminescent devices [21], light emitting diode phosphors [22] and scintillation detectors [23].

Scientifically they have earned notoriety because of the unusual behaviour of certain materials such as CeN, which displays valence fluctuations [24] and SmS, which shows a first order metal to insulator transition [25]. The Eu chalcogenides (O, S, Se, Te) were some of the earliest known ferromagnetic insulators [26, 27] and EuO displays giant magnetoresistant behaviour [28, 29].

Also the mixing of on the one hand strongly correlated 4f-electrons, and on the other delocalized 5d electrons, constitutes a pronounced computational challenge and therefore the binary lanthanides have served as test cases for new computational methods [30, 31]. Outside of the binary Lanthanides, Ln based materials are the focus of solid state research into a variety of fundamental phenomena such as metal-insulator transitions, colossal magnetoresistance, and valence transitions or charge ordering [27, 32-35].

Ln ions either have a $[Xe]4f^n$ or a $[Xe]4f^{n-1}5d^1$ ground state electron configuration. The $4f^n$ configuration has n strongly correlated and localized core-like 4f electrons. The $4f^n$ energy levels are in a good approximation unaffected by the Ln-ion crystalline environment but strongly change as a function of n. The 5d-electrons have an entirely different character. Their energy strongly depends on the crystalline environment but not on n. In addition the 5d-orbitals are highly delocalized and form the conduction band (CB).

Despite the fact that the lanthanide ions are chemically very similar due to the well shielded nature of the $4f^n$ valence electrons by filled $5p^6$ and $6s^2$ orbitals, Ln materials often show a strong change in behaviour when we move just one position in the periodic table. While TmS is a metal, YbS is a small bandgap insulator [36-38], while La_2O_3 is a transparent insulator, Ce_2O_3 is a yellow semiconductor and while CeF_4 and PrF_4 are stable compounds, NdF_4 is not [39]. Even when the lanthanide ion remains the same, material properties can change considerably when the type of ligand changes. For example CeF_4 is a stable compound but the other Ce-tetrahalides are not [39] and while SmO is metallic, the other Sm monochalcogenides are semiconductors [40, 41].

It would be very useful to have a universally applicable model that is able to explain all of these variations in material properties in a systematic fashion. Many reviews have appeared that have attempted to do so for a subclass of lanthanide materials [26, 42-44]. Others reported systematic variation as a function of the type of Ln ion. For example Hulliger's review of the changes in conductivity behaviour of lanthanide compounds and Kim and Oishi's work on

the enthalpy of formation and stability of Ln dihalides both note that the systematic behaviour is related to the binding energy of the 4f electrons in the lanthanides [45, 46].

Other work addresses the behaviour of a specific lanthanide such as Ce, Sm, or Yb and describes behaviour as a function of the type of ligand. For example Cho compares the electronic structures of trivalent insulating Sm and Gd compounds such as SmF_3 and GdF_3 [47], Wachter describes the optical properties of Eu chalcogenides [26], Weaver discusses 4f localization in Ce compounds [48] and Temmerman *et al.* consider the electronic configuration of Yb compounds [49]. Recently Petit *et al.* used *ab initio* methods to study the electronic structures of Ln monopnictides and monochalcogenides LnX (X= N, P, As, Sb, Bi, O, S, Se Te, Po) [50].

Ab initio models however are computationally heavy and require a lot of specialist knowledge before they can be applied. A model that can calculate the electronic structure of Ln compounds quickly and simply could be beneficial for the material sciences community. In a previous paper [51] we have shown that the change in the $4f^n$ ground state energy with n (the type of lanthanide) appears to be independent of the type of compound while the energy difference between the top of the mp valence band (mp-VB) and the bottom of the 5d derived conduction band (5d-CB) appears to a good approximation to be independent of n. It also appears that the wide variety in the electrical and optical properties of Ln- materials is to a large extent controlled by the energies of these states relative to each other, meaning that in order to predict these properties for Ln-materials we need to establish the positions of the 4f, 5d-CB and mp-VB energies.

This universal behaviour was used to construct an empirical model that was applied to the well-known Ln oxides LnO, Ln_2O_3, and LnO_2 for which it correctly predicts insulating, semiconducting, or metallic behaviour, nature, and magnitude of bandgap energies, and chemical stability of Ln materials as well as valence and valence changes of Ln ions.

In this chapter the model is introduced and an explanation is given to the data used and the construction of the schemes. In chapter three the model is applied to the binary lanthanide halides, chalcogenides and pnictides, before the various trends in properties are discussed in chapter four. In chapter five the model is compared to experiment for the lanthanide diiodides.
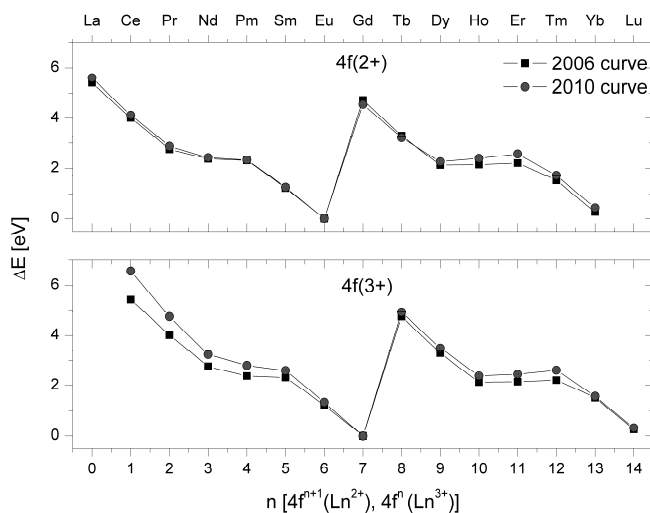
Figure 2.1. Variations in the divalent (top panel) and trivalent (bottom panel) 4f ground state energies as a function of the type of lanthanide. The curves indicate the 2006 version (squares) [51] and the version used in this chapter (circles) [53]

2.2. Application of the empirical model

The method used to position the energy of the 4f ground state and the bottom of the 5d conduction band of the lanthanide ions with respect to the top of the valence band in pure lanthanide compounds has evolved from an empirical method developed for lanthanide doped inorganic compounds, see e.g. [52] and [53] and references therein. In a previous work [5] it was shown that the basic optical, electrical and some chemical properties of the binary Ln oxides and the Ln monosulfides are determined by the energy of the ligand $m\text{p}^6$ derived valence band (where m=2 for F, O and N, m=3 for Cl, S and P, m=4 for Br, Se and As and m=5 for I, Te and Sb), the Ln 5d-CB and the localized 4f^n ground states of the 2+, 3+ or 4+ lanthanides relative to each other. It was

demonstrated that as soon as the energies of the mp-VB, 5d-CB and $4f^n$ states relative to each other are established experimentally for one specific Ln-material, e.g. EuO, then the energies of those states in all other compounds of that series, e.g. LnO (Ln= La…Yb), can be predicted using a simple empirical model. Within this model the energy difference between the top of the mp-VB and the bottom of the 5d-CB is assumed constant as a function of the type of Ln-ion. It is also assumed that the energy of the $4f^n$ ground state as function of the number of electrons n follows a characteristic double zigzag pattern which is independent of the type of compound. Figure 2.1 shows these energies and patterns for the 2+ and 3+ Ln-ions as used in the 2006 paper [51] (square data symbols) and the energies that will be used in this paper (circular data symbols) [53]. The differences between these two sets of energies are the result of including more and new experimental data. These changes have little impact on the properties predicted by the schemes in the original paper, with the exception of an improvement in the LnO_2 scheme which will be discussed further on in this paper. Thus when reliable experimental data on a few crucial or pinning compounds are available the mp-VB, $4f^n$ ground states and the 5d-CB energies can be plotted as a function of n, which results in the typical schemes that were presented in our earlier work on the Ln oxides (LnO, Ln_2O_3, LnO_2) and which will be presented in this work for all of the other binary Ln-halides, chalcogenides and pnictides (see figures 2.2, and 3.1 to 3.11). From here on we will denote the zigzag curve that connects the lowest energy $4f^n$ level of the trivalent lanthanides in the level schemes as 4f(3+). Likewise the curve for the divalent lanthanides is denoted as 4f(2+).

Although several types of experimental data have been used to construct the schemes in figure 2.2 and chapter 3, they can be divided into two categories: photoelectron emission and optical data. The experimental data used is compiled and referenced in tables 2.1, 3.1, 3.2 and 3.3. Valence band X-ray photoelectron spectroscopy (XPS) and Ultraviolet Photoelectron Spectroscopy (UPS) were used to determine the energy difference between the mp-VB and

the $4f^n$ ground states by using the difference between the lower energy edges of the anion mp peak and the lanthanide $4f^n$ peak in XPS or UPS spectra. Examples of data obtained using XPS are (i) the $LnBr_3$ $4f(3+)$ ground state which was positioned using data from the paper of Sato on $CeBr_3$ [54], (ii) the LnS occupied $4f(2+)$ ground state curve which was positioned using data on SmS from the papers by Gudat *et al.* and Chainani *et al.* [55, 56], and (iii) the LnN occupied $4f(3+)$ curve which was positioned using data on CeN from the paper by Baer *et al.* [57].

Optical data was used to obtain the energy difference between occupied and unoccupied levels in particular the transition energy from the 4f ground state to the 5d-CB, the transition energy from the mp-VB to the 5d-CB and the charge transfer (CT) energy from the mp-VB to a trivalent or tetravalent lanthanide. This latter transition has as final state the 2+ or 3+ 4f ground state of that lanthanide and provides a pinning point for the respective $4f(2+)$ or $4f(3+)$ zigzag curves in our schemes. Luminescence excitation spectroscopy was of most use for wide bandgap materials such as LnF_3 and $LnCl_3$ [58-60]. Because narrow bandgap materials such as EuS do not luminesce, absorption, transmission or diffuse reflectance data were also used. For instance, the $4f^6$-$4f^5 5d^1$ transition energy of SmS as published by Batlogg *et al.* was used to position the LnS 5d-CB relative to the $4f(2+)$ curve [41]. Diffuse reflectance was very useful for determining the bandgaps of narrow bandgap powder samples. For example for LnP the 3p-VB to 5d-CB bandgap was placed using data on the 3p to 5d-CB transitions of NdP, SmP and HoP from diffuse reflectance spectra measured by Meng and Ren [61, 62]. For all of the optical measurements we used the absorption edge in order to calculate the transition energy.

For cases where the $4f^n$ to 5d-CB transition for all compounds in a series, for example the LnI_2 series, were unknown, the $4f^n$ to 5d luminescence excitation energy of an isostructural Ln doped inorganic compound such as SrI_2:Eu was used (see table 3.1 and references therein). In situations where the energy

difference between the mp–VB and 5d–CB was unknown for any compounds in a series (i.e. LnF_2), we used the energy difference known for the trivalent compounds (i.e. LnF_3). This is not necessarily correct but as will be apparent later, the precise location of the valence band does not affect the material properties of these types of compounds. For situations where no information on the $4f^n$ to 5d-CB energy for either the compound or its doped equivalent could be found, e.g. Ln_2Te_3, trends seen in the decrease of the mp to 4f energy for the other series of compounds for that period of the periodic table (i.e. O, S, Se…) were used to place the curves.

Table 2.1 presents all the data used to construct the energy level schemes for the lanthanide oxides with 2+, 3+ and 4+ ions presented in figure 2.2. Energies that were estimated have also been compiled in the table.

Table 2.1. Sources of the photoelectron (XPS, UPS) and optical (transmission, reflection, luminescence) experimental data for the 2+, 3+ and 4+ binary lanthanide oxides used in this work to construct the energy level diagram presented in figure 2.2. "?" means that no information on the transition was available, est. means that the transition was estimated, while "n/a" means not applicable, meaning that the transition is not meaningful in that scheme.

	Ln^{x+} (x=)	mp to 2+ 4f	mp to 3+ 4f	mp to 5d	4f-5d
LnO	2	3eV EuO (average) [63-65]	n/a	?	1.33eV EuO [26]
Ln_2O_3	3	4.1 Eu_2O_3 [66]	3.4eV Ce_2O_3 [67]	5eV La_2O_3 [66]	3.6eV Pr_2O_3 [66]
LnO_2	4	n/a	3.1eV CeO_2 [68]	5eV est.	n/a

How the results will be presented and how the presented schemes should be interpreted will now be explained. In each of the energy level schemes presented here and in chapter 3, the mp-VB is plotted using square data symbols, while the 5d-CB is represented by round data symbols. $4f^n$ ground state levels are represented by triangular data symbols. Generally, occupied states (donor states) are represented by solid data symbols while unoccupied states (acceptor states) are represented by empty data symbols. The data

symbols as function of *n* will be connected with solid lines like in Figure 2.1. Both the resulting 4f(2+) and 4f(3+) curves make a characteristic double zigzag pattern. The experimental data used to position the 4f(2+) and 4f(3+) curves relative to the VB-curve and/or CB-curve are represented by star shaped data symbols with an arrow indicating the corresponding transition.
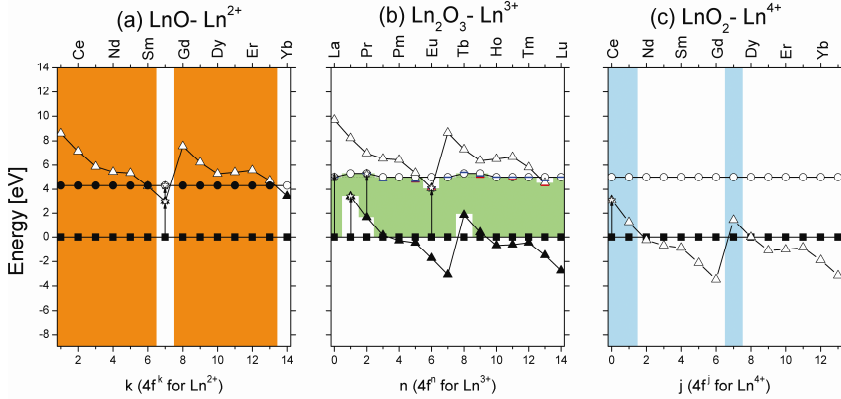
Figure 2.2. Predicted electronic structures of the binary Ln oxides (Ln=La to Lu): a) Ln monoxides (LnO): orange shading = metallic compounds; b) Ln sesquioxides (Ln_2O_3): light green shading = optical bandgap. Blue and red horizontal bars indicate the bandgaps measured by Borchardt [66] and White [69] respectively. c) Ln dioxides (LnO_2): Light blue vertical bands = stable compounds. In all figures squares = 2p-VB, circles = 5d-CB, and triangles = 4f ground state. Filled symbols indicate an occupied band. Stars and arrows indicate the experimental data used.

2.3. The Lanthanide Oxides

As an example, the energy level scheme of the binary Ln oxides that have 2+ Ln-ions (from here on referred to as a divalent scheme) show the data symbols pertaining to the mp-VB, 4f(2+) ground state and the 5d–CB energy for each of the compounds in the lanthanide monoxide series (see Figure 2.2a). When the 4f(2+) ground state is below the conduction band it will be occupied and denoted as a solid triangle in our schemes, while the 5d-CB states are unoccupied (open circle) so that consequently the compound is insulating or semiconducting with the electronic configuration $4f^n5d^0$. This is the case for EuO and YbO in Figure 2.2a. When the 4f(2+) ground state is above the

bottom of the conduction band, the 4f electron is donated to the conduction band. The 4f(2+) data symbol will in this case be shown as an open triangle and the 5d-CB data symbol as solid circle. The lanthanide ion becomes trivalent and the material becomes metallic with the electronic configuration $4f^{n-1}5d^1$. When compounds are metallic this is indicated in the schemes by vertical orange bands. Apart from EuO and YbO this is the case for all LnO compounds, see Figure 2.2a. Some materials have the 4f(2+) ground state level lying just below or overlapping with the bottom of the conduction band. We consider these materials to be critical as they show unique properties and the correct prediction of these properties provides an indication of the accuracy of our model. When the 4f(2+) ground state lies just below the 5d-CB, as is seen for SmS and TmTe, the material is usually switchable in the sense that a small perturbation, such as pressure, is enough to shift the bottom of the 5d-CB to below the 4f levels leading to metallic behaviour. The other situation leads to a mixed valence compound such as TmSe or SmO. In this case the $4f^n$ levels lie so close above the bottom of the 5d band leading to interconfigurational valence behaviour where lanthanide ions fluctuate rapidly between a 2+ and a 3+ configuration so that the valence appears to be somewhere between 2+ and 3+.

The energy level scheme of the binary Ln oxides that have 3+ Ln-ions (from here on referred to as trivalent schemes) such as the one for Ln_2O_3 shown in Figure 2.2b, show curves that connect the data symbols of the mp–VB (solid squares), the 4f(3+) ground state (solid triangles), the position of the divalent 4f(2+) ground state (open triangles) and the 5d-CB (open circles). One obvious property that can be derived from trivalent compounds such as Ln_2O_3 is the change in bandgap energy when going through the series from La to Lu. The bandgap energy is in this case that of the lowest dipole allowed transition, i.e. mp-VB to the 5d-CB, mp-VB to the 4f(2+) ground state or from the 4f(3+) ground state to the 5d-CB. Light green shading has been used to indicate what levels determine the optical bandgap of each compound in a series. Figure 2.2b

shows that 2p-VB to 5d-CB transitions determine the bandgap for La_2O_3, Nd_2O_3, Pm_2O_3, Sm_2O_3, Gd_2O_3, Ho_2O_3, Er_2O_3, Tm_2O_3 and Lu_2O_3, while 4f(3+) ground state to 5d-CB transitions apply for Ce_2O_3, Pr_2O_3, Tb_2O_3 and Dy_2O_3, and finally mp-VB to 4f(2+) ground state transitions apply for Eu_2O_3 and Yb_2O_3.

The energy level scheme of the binary Ln oxides that have 4+ Ln-ions (from here on referred to as tetravalent schemes) show curves corresponding to a filled mp-VB (solid squares), an empty 4f(3+) ground state (open triangles) and a 5d–CB (open circles), see Fig. 2.2c. For these compounds the schemes can be used to predict whether a compound can in principle be stable. An unoccupied 4f(3+) acceptor state below the filled mp-VB is energetically impossible because it will capture an electron from the higher energy mp-VB. Those compounds therefore do not exist. In addition we will conclude, that the closer the empty 4f(3+) ground state is above the valence band, the less stable the compound will be. Those compounds that energetically can exist are indicated by vertical light blue bands in the schemes.

Although the mp-VB to 5d-CB energy difference is considered constant as a function of n there are some exceptions. We noticed that compounds with the $4f^n$ ground state located between the mp-VB and the 5d-CB showed a different mp-VB to 5d-CB energy, depending on which method was used to determine it. The energy can be derived from the sum of the mp-VB to $4f^n$ energy obtained for one lanthanide compound and the 4f to 5d transition energy estimated from another lanthanide compound of the same series. It can also be obtained from the directly measure mp-VB to 5d-CB of one specific lanthanide compound of the series. For example, if an electron is excited from the 2p-VB to the 5d-CB like in La_2O_3 the energy difference is 5eV, and this difference in first approximation holds in Fig. 2b for all Ln_2O_3 compounds. If we next consider Ce_2O_3, the energy difference between the 2p-VB and the $4f^1$ Ce^{3+} ground state is 3.4 eV. With the 4f(3+) curve we then predict a 2p-VB to $4f^2$ Pr^{3+} ground

state energy difference of 1.7 eV. From data on Pr_2O_3 the energy difference between the $4f^2$ Pr^{3+} ground state and the 5d-CB is 3.6 eV and we then get a 5.3eV energy difference between the 2p-VB and 5d-CB for Pr_2O_3. We believe that the 0.3 eV difference between the value of 5.0 eV based on La_2O_3 and the value of 5.3 eV found indirectly for Pr_2O_3 is due to lattice relaxation after an optical transition has taken place.

In this thesis it was decided to show these different values in the schemes. If the 4f levels lie below the mp-VB or above the 5d-CB, the mp-VB to 5d-CB energy is used to place the 5d-CB. If the 4f levels lie above the mp–VB and below the 5d-CB the summation of the mp to 4f energy and the 4f to 5d-CB energy is used to place the 5d-CB. This can be seen in figure 2b, where the 5d-CBs of Ce_2O_3, Pr_2O_3, Tb_2O_3 and Dy_2O_3 are shown at higher energy than the 5d-CBs of the other Ln sesquioxides.

2.4. Sources of error and the accuracy of the empirical model

As this model is empirical and therefore relies upon experimental data, most errors arise from experimental errors or the ambiguity of the interpretation. For example by using the absorption edge to establish an energy value, errors can be introduced due to the presence of impurities and therefore change from sample to sample. From our comprehensive analysis of experimental data we estimate the error to be in the range of 0.3 eV.

In addition as we use data collected by different methods such as X-ray photoelectron spectroscopy and luminescence excitation spectroscopy, systematic errors may be present too. Throughout this work we have tried to use as much as possible the same experimental technique for a specific p-f, f-d or p-d transition. In order to be consistent we have used the absorption edge of band features to derive energy values for our schemes. As seen with the lanthanide oxides shown above, and as will be shown in chapter 3, the results obtained by this model can be successfully used not only to predict the optical bandgap of materials, but the valencies of their Ln ions and even their existence.

References

[1] Skorodumova N V, Simak S I, Lundqvist B I, Abrikosov I A and Johansson B 2002 *Physical Review Letters* **89** 166601

[2] Chueh W C, Falter C, Abbott M, Scipio D, Furler P, Haile S M and Steinfeld A 2010 *Science* **330** 1797-801

[3] Burzo E 1998 *Reports on Progress in Physics* **61** 1099-266

[4] Jensen T, Ostroumov V G, Meyn J-P, Huber G, Zagumennyi A I and Shcherbakov I A 1994 *Applied Physics B* **58** 373-9

[5] Wisniewski D J, Boatner L A, Neal J S, Jellison G E, Ramey J O, North A, Wisniewska M, Payzant A E, Howe J Y, Lempicki A, Brecher C and Glodo J 2008 *IEEE Transactions on Nuclear Science* **55** 1501-8

[6] Kitaoka K, Takahara K, Kozuka H and Yoko T 1999 *Journal of Sol-Gel Science and Technology* **16** 183-93

[7] Fujihara S, Kato T and Kimura T 2003 *Journal of Sol-Gel Science and Technology* **26** 953-6

[8] Cherepy N J, Kuntz J D, Tillotson T M, Speaks D T, Payne S A, Chai B H T, Porter-Chapman Y and Derenzo S E 2007 *Nuclear Instruments and Methods in Physics Research A* **579** 38-41

[9] Gorokhova E I, Demidenko V A, Khristich O A, Mikhrin S B and Rodnyĭ P A 2003 *Journal of Optical Technology* **70** 693-8

[10] Wang F and Liu X 2009 *Chemical Society Reviews* **38** 976-89

[11] Rambabu U, Munirathnam N R, Prakash T L and Buddhudu S 2002 *Materials Chemistry and Physics* **78** 160-9

[12] Nishimura M, Nanai Y, Bohda T and Okuno T 2009 *Japanese Journal of Applied Physics* **48** 072301

[13] Balaji T and Buddhudu S 1993 *Materials Chemistry and Physics* **34** 310-2

[14] Shah K S, Jaroslaw G, Higgins W, van Loef E V D, Moses W W, Derenzo S E and Weber M J 2005 *IEEE Transactions on Nuclear Science* **52** 3157-9

[15] Ra S, Kim S, Kim H J, Park H, Lee S, Kang H and Doh S-H 2008 *IEEE Transactions on Nuclear Science* **55** 1221-4

[16] Drozdowski W, Dorenbos P, Bos A J J, Bizarri G, Owens A and Quarati F G A 2008 *IEEE Transactions on Nuclear Science* **55** 1391-6

[17] Le Clair P, Ha J K, Swagten H J M, Kohlhepp J T, van de Vin C H and de Jonge W J M 2002 *Applied Physics Letters* **80** 625-7

[18] Schmehl A, Vaithyanathan V, Herrnberger A, Thiel S, Richter C, Liberati M, Heeg T, Röckerath M, Kourkoutis L F, Mühlbauer S, Böni P, Muller D A, Barash Y, Schubert J, Idzerda Y, Mannhart J and Schlom D G 2007 *Nature Materials* **6** 882-7

[19] Tsunashima S 2001 *Journal of Physics D: Applied Physics* **34** R87-R102

[20] Lage M M, Moreira R L, Matinaga F M and Gesland G-Y 2005 *Chemistry of Materials* **17** 4523-9

[21] Wang Y Q and Steckl A J 2003 *Applied Physics Letters* **82** 502-4

[22] Mueller-Mach R, Mueller G, Krames M R, Höppe H A, Stadler F, Schnick W, Juestel T and Schmidt P 2005 *Physica Status Solidi A* **202** 1727-32

[23] van Loef E V D, Dorenbos P, van Eijk C W E, Krämer K W and Güdel H U 2001 *Applied Physics Letters* **79** 1573-5

[24] Baer Y and Zuercher C 1977 *Physical Review Letters* **39** 956-9

[25] Jayaraman A, Narayanamurti V, Bucher E and Maines R G 1970 *Physical Review Letters* **25** 1430-3

[26] Wachter P 1972 *Critical Reviews in Solid State and Materials Sciences* **3** 189

[27] Steeneken P G, Tjeng L H, Elfimov I, Sawatzky G A, Ghiringhelli G, Brookes N B and Huang D-J 2002 *Physical Review Letters* **88** 47201

[28] Shapira Y, Foner S and Reed T B 1973 *Physical Review B* **8** 2299-315

[29] Oliver M R, Dimmock J O, McWhorter A L and Reed T B 1972 *Physical Review B* **5** 1078-98

[30] Strange P, Svane A, Temmerman W M, Szotek Z and Winter H 1999 *Nature* **399** 756-8

[31] Petit L, Svane A, Szotek Z and Temmerman W M 2005 *Physical Review B* **72** 205118

[32] Rao C N R, Arulraj A, Cheetham A K and Raveau B 2000 *Journal of Physics: Condensed Matter* **12** R83-R106

[33] Prellier W, Lecoeur P and Mercey B 2001 *Journal of Physics: Condensed Matter* **13** R915-R44

[34] Hoekstra A F T, Roy A S, Rosenbaum T F, Griessen R, Wijngaarden R J and Koeman N J 2001 *Physical Review Letters* **86** 5349-52

[35] Arvanitidis J, Papagelis K, Margadonna S, Prassides K and Fitch A N 2003 *Nature* **425** 599-602

[36] Bucher E, Andres K, di Salvo F J, Maita J P, Gossard A C, Cooper A S and Hull G W, Jr. 1975 *Physical Review B* **11** 500-13

[37] Wachter P, Kamba S and Grioni M 1998 *Physica B* **252** 178-85

[38] Matsunami M, Chainani A, Taguchi M, Eguchi R, Ishida Y, Takata Y, Okamura H, Nanba T, Yabashi M, Tamasaku K, Nishino Y, Ishikawa T, Senba Y, Ohashi H, Tsujii N, Ochiai A and Shin S 2008 *Physical Review B* **78** 195118

[39] Haschke J M 1979 *Handbook on the Physics and Chemistry of the Rare Earths: Volume 4 - Non-Metallic Compounds - II,* ed K A Gschneidner and L R Eyring (Amsterdam: North-Holland Publishing Company)

[40] Leger J M, Aimonino P, Loriers J, Dordor P and Coqblin B 1980 *Physics Letters A* **80** 325-7

[41] Batlogg B, Kaldis E, Schlegel A. and Wachter P 1976 *Physical Review B* **14** 5503-14

[42] Wilson J A 1977 *Structure and Bonding* **32** 57-91

[43] Prokofiev A V, Shelykh A I, Golubkov A V and Smirnov I A 1995 *Journal of Alloys and Compounds* **219** 172-5

[44] Ionova G V 1990 *Russian Chemical Reviews* **59** 39-51

[45] Hulliger F 1968 *Helvetica Physica Acta* **68** 945-54

[46]   Kim Y-C and Oishi J 1979 *Journal of the less common metals* **65** 199-210

[47]   Cho E J 2007 *Journal of the Korean Physical Society* **51** 1331-6

[48]   Weaver J H 1983 *Journal of the less common metals* **94** 17-22

[49]   Temmerman W M, Szotek Z, Svane A, Strange P, Winter H, Delin A, Johansson B, Eriksson O, Fast L and Wills J M 1999 *Physical Review Letters* **83** 3900-3

[50]   Petit L, Tyer R, Szotek Z, Temmerman W M and Svane A 2010 *New Journal of Physics* **12** 113041

[51]   van der Kolk E and Dorenbos P 2006 *Chemistry of Materials* **18** 3458-62

[52]   Dorenbos P 2004 *Journal of Luminescence* **108** 301-5

[53]   Dorenbos P, Krumpel A H, van der Kolk E, Boutinard P, Bettinelli M and Cavalli E 2010 *Optical Materials*

[54]   Sato S 1976 *Journal of the physical society of Japan* **41** 913-20

[55]   Gudat W, Alvarado S F and Campagna M 1978 *Solid State Communications* **28** 943-6

[56]   Chainani A, Kumigashira H, Ito T, Sato T, Takahashi T, Yokoya T, Higuchi T, Takeuchi T, Shin S and Sato N K 2002 *Physical Review B* **65** 155201

[57]   Baer Y, Hauger R and Zuercher C 1979 *Journal of Electron Spectroscopy and Related Phenomena* **15** 27-32

[58]   van Loef E V D, Dorenbos P, van Eijk C W E, Krämer K W and Güdel H U 2003 *Physical Review B* **68** 045108

[59]   Popma T J A, van der Weg W F and Thimm K 1981 *Journal of Luminescence* **24-25** 289-92

[60]   Olson C G, Piacentini M and Lynch D W 1978 *Physical Review B* **18** 5740-9

[61]   Meng J and Ren Y 1992 *Materials Chemistry and Physics* **30** 235-8

[62]   Meng J and Ren Y 1991 *Solid State Communications* **80** 485-8

[63]   Steeneken P G 2002 New light on EuO thin films. In: *PhD Thesis*:
       Rijksuniversiteit Groningen)

[64]   Eastman D E, Holtzberg F and Methfessel S 1969 *Physical Review
       Letters* **23** 226-9

[65]   Beukers J N, Kleibeuker J E, Koster G, Blank D H A, Rijnders G,
       Hilgenkamp H and Brinkman A 2010 *Thin Solid Films* **518** 5173-6

[66]   Borchardt H J 1963 *The Journal of Chemical Physics* **39** 504-11

[67]   Allen J W 1985 *Journal of Magnetism and Magnetic Materials* **47-48**
       168-74

[68]   Marabelli F and Wachter P 1987 *Physical Review B* **36** 1238-43

[69]   White W B 1967 *Applied Spectroscopy* **21** 167-71

Chapter 3: The application of an empirical model for the optical and electronic properties of the binary Lanthanide halide, chalcogenide and pnictide compounds

Abstract.

The basic optical, electrical and chemical properties of the binary divalent, trivalent and tetravalent lanthanide (Ln= La…Lu) halides (F, Cl, Br, I), chalcogenides (O, S, Se, Te) and pnictides (N, P, As, Sb) were studied using an empirical model that utilizes the systematic behaviour in the energy difference between the localized $4f^n$-states, the 5d-derived conduction band and the mp-derived valence band (m=2…5) over the Lanthanide series.

3.1. Introduction

By presenting the energy level schemes for the binary lanthanide oxides in chapter 2, we introduced how the schemes should be interpreted. The schemes show occupied and unoccupied states by means of solid and open data symbols. Transitions between them determine the size and nature of the bandgap of the material. Whether or not the $4f^n$ or the $4f^{n-1}5d$ state is occupied determines if the compound will be insulating/semi-conducting or metallic. In situations where unoccupied states are found below the valence band, materials energetically cannot exist. By means of the introduced colouring a rapid overview of the main properties of the materials can be observed. In the following we will present schemes for the other binary lanthanide compounds

in the same fashion as used for the Ln-oxides above. Each time we will briefly indicate the main sources of experimental data used and the characteristics derived from the presented schemes.

3.2. Lanthanide halides

The lanthanide halides have properties that range from those of wide bandgap insulators such as LaF_3, through semiconductors such as $SmBr_2$, to metals such as LaI_2. Because of their wide bandgaps, which range from around 10eV for LaF_3 to 3.9eV for LnI_3, the trivalent lanthanide trihalides have been used as scintillators and laser crystals. The lanthanide dihalides form both semiconducting compounds such as EuF_2, $SmCl_2$, $NdBr_2$ and DyI_2 and metallic compounds such as $LaBr_2$ and CeI_2. However the only tetravalent halides observed are CeF_4, PrF_4 and TbF_4.

A wide range of data was used in order to create the schemes. For the trivalent Lanthanide tri-fluorides, chlorides and bromides, complete sets of data were available, while for the lanthanide dichlorides, a scheme had to be estimated using $SrCl_2$: Eu, and the non-existent tetra-chlorides, bromides and iodides were estimated using information on the appropriate trihalide and the similar positioning of the Ce 4f energy of Ce_2O_3 and CeO_2.

Table 3.1 presents all the data used to construct the energy level schemes for the lanthanide halides presented in figures 3.1 to 3.4. Energies that were estimated have also been compiled in the table.

3.2.1. Lanthanide fluorides.

Lanthanide ions in binary lanthanide fluoride compounds exist in a divalent, trivalent and a tetravalent form. The energy level scheme for the lanthanide difluorides LnF_2 is plotted in figure 3.1a. The only usable experimental data available for the difluorides is the $4f^7$ to 5d-CB energy of EuF_2. This energy, listed in table 3.1, was used to position the 4f(2+) zigzag curve of the Ln^{2+}-ions relative to the 5d-CB as shown in Fig. 3.1a. As no data on the 2p-VB to 5d-CB

transition energy could be found, that energy was assumed to be the same as that of LaF_3. The resulting energy scheme predicts semiconducting behaviour for NdF_2, PmF_2, SmF_2, EuF_2, DyF_2, HoF_2, ErF_2, TmF_2 and YbF_2. Today only SmF_2, EuF_2 and YbF_2 are known to exist.[17-19] The other LnF_2 compounds, LaF_2, CeF_2, PrF_2, GdF_2 and TbF_2, are predicted to be metallic although they have not yet been synthesized.

Table 3.1. Sources of the photoelectron (XPS, UPS) and optical (transmission, reflection, luminescence) experimental data for the 2+, 3+ and 4+ binary lanthanide halides used in this work to construct the energy level diagrams presented in figures 3.1 to 3.4. "?" means that no information on that transition was available, est. means that the transition was estimate, while "n/a" means not applicable, meaning that the transition is not meaningful in that scheme.

	Ln^{x+} (x=)	mp to 2+ 4f	mp to 3+ 4f	mp to 5d	4f-5d
LnF_2	2	?	n/a	10eV est.	3eV EuF_2 [1]
$LnCl_2$	2	?	n/a	6.2eV est.	3eV $SrCl_2$:Eu [2]
$LnBr_2$	2	?	n/a	5.2eV est.	1.8eV $SmBr_2$ [3]
LnI_2	2	?	n/a	3.9eV est.	3.1eV EuI_2 [4]
LnF_3	3	7.14eV EuF_3 [5]	4.5eV CeF_3 [6, 7]	10eV LaF_3 [8, 9]	4.9eV CeF_3 [10]
$LnCl_3$	3	3eV $LaCl_3$:Eu [11]	1.5eV $CeCl_3$ [6]	6.2eV $LaCl_3$ [12]	4.2eV $LaCl_3$:Ce [13]
$LnBr_3$	3	4.96eV $PrBr_3$ [13]	1eV $CeBr_3$ [6]	5.2eV $LaBr_3$ [12]	3.9eV $LaBr_3$:Ce [12]
LnI_3	3	1.4eV EuI_3 est.	0.4eV CeI_3 [14]	3.9eV LaI_3 [14]	3.5eV LaI_3:Ce [15]
LnF_4	4	n/a	3.9 eV CeF_4 [16]	8eV CeF_4 [16]	n/a
$LnCl_4$	4	n/a	1.5eV $CeCl_4$ est.	6.2eV est.	n/a
$LnBr_4$	4	n/a	1eV $CeBr_4$ est.	5.2eV est.	n/a
LnI_4	4	n/a	0.4eV CeI_4 est.	3.9eV est.	n/a

The energy level scheme for the lanthanide trifluoride compounds (LnF_3) is shown in figure 3.1b. The lanthanide trifluorides are all wide bandgap insulators. The optical gap for La, Gd and LuF_3 is determined by the 2p-VB to a 5d-CB transition while for Ce, Pr, Nd, Pm, Sm, Tb and Dy, Ho, Er, and TmF_3 the transition is controlled by a $4f^n$ to 5d-CB transition and for Eu and YbF_3 a 2p-VB to $4f^{n+1}$ transition is predicted as can be seen in Fig. 3.1b where the variation in the optical bandgap is coloured light green. It is also possible that

SmF_3 and TmF_3 could show an inter lanthanide charge transfer, i.e. $Sm^{3+}+Sm^{3+} \rightarrow Sm^{4+}Sm^{2+}$. The vertical arrows indicate the available experimental data from table 3.1 that was used to construct the energy level scheme.
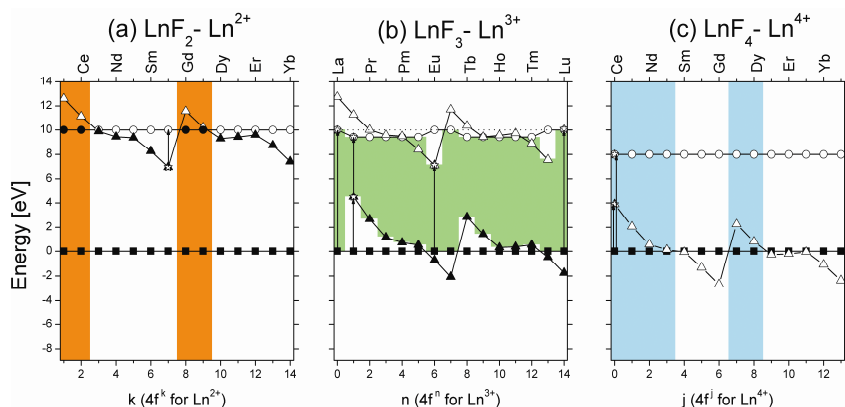
Figure 3.1. Predicted electronic structures of the binary Ln fluorides (Ln=La to Lu): a) Ln difluorides (LnF_2): orange shading = metallic compounds; b) Ln trifluorides (LnF_3): light green shading = optical bandgap; c) Ln tetrafluorides (LnF_4): Light blue vertical bands = stable compounds. In all figures squares = 2p-VB, circles = 5d-CB, and triangles = 4f ground state. Filled symbols indicate an occupied band. Stars and arrows indicate the experimental data used.

Figure 3.1c shows the energy level scheme for the tetravalent lanthanide fluoride compounds, LnF_4. As indicated by the arrow at j=0, data on CeF_4 was used to construct the level schemes. Figure 3.1c predicts that CeF_4, PrF_4 NdF_4, PmF_4, TbF_4 and DyF_4 have a 4f-ground state above the VB and could therefore in principle exist as stable compounds, indicated by blue vertical bands in the scheme. Of the LnF_4 compounds CeF_4, PrF_4 and TbF_4 are known to exist [18]. The scheme predicts that the energies of the unoccupied trivalent 4f states of NdF_4, PmF_4 and DyF_4 lie less than 1eV from the top of the valence band. In such cases it is easy to reduce Ln^{4+} to the trivalent charge state suggesting that such compounds are unstable and difficult or even impossible to synthesize.

3.2.2. Lanthanide chlorides.

Contrary to the lanthanide fluoride compounds, the lanthanide chloride compounds are only reported to exist in a divalent and a trivalent form. Semiconducting $NdCl_2$, $SmCl_2$, $EuCl_2$, $DyCl_2$, $TmCl_2$ and $YbCl_2$ have been prepared [18, 20]. However, no relevant data on the electronic structure could be found, so the level scheme in figure 3.2a was made using the 4f(2+) ground state to 5d-CB transition energy estimated from the excitation spectrum of Eu^{2+} doped $SrCl_2$ (see table 3.1 and references therein). The scheme predicts that, if they can be prepared, $PrCl_2$, $PmCl_2$, $HoCl_2$ and $ErCl_2$ should also be semiconducting while La, Ce, Gd and $TbCl_2$ would be metallic.

In figure 3.2b the energy level scheme for the lanthanide trichlorides ($LnCl_3$) has been plotted. Contrary to what is observed for the trifluorides where the optical gap is most often controlled by a 4f(3+) ground state to 5d-CB transition, the optical gap for most trichlorides is determined by a 3p-VB to 4f(2+) transition. Only for $CeCl_3$ is the bandgap energy determined by a 4f to 5d-CB transition while a 3p-VB to a 5d-CB transition is indicated for La, Gd and $LuCl_3$.

No lanthanide tetrachlorides are known to exist. Lanza and Fragalá conclude from an *ab-initio* study that $CeCl_4$ should thermodynamically be far less stable than CeF_4 [21]. A scheme has been predicted by assuming that the positions of the 4f levels in the tetravalent chlorides have similar energies to those of trivalent $LnCl_3$ (figure 3.2c). This can be assumed because this behaviour is also observed for the tetravalent oxides and fluorides. From this scheme we can see that of all the compounds in this series, only $CeCl_4$ might be stable. However, the 4f(3+) ground state lies about 1.5 eV above the 3p-VB whereas for CeF_4 the energy difference is 4 eV. This suggests, similarly to Lanza and Fragalá, that $CeCl_4$ will be much less stable than CeF_4.

Figure 3.2. Predicted electronic structures of the binary Ln chlorides (Ln=La to Lu): a) Ln dichlorides ($LnCl_2$): orange shading = metallic compounds; b) Ln trichlorides ($LnCl_3$): light green shading = optical bandgap; c) Ln tetrachlorides ($LnCl_4$): Light blue vertical bands = stable compounds. In all figures squares = 3p-VB, circles = 5d-CB, and triangles = 4f ground state. Filled symbols indicate an occupied band. Stars and arrows indicate the experimental data used.
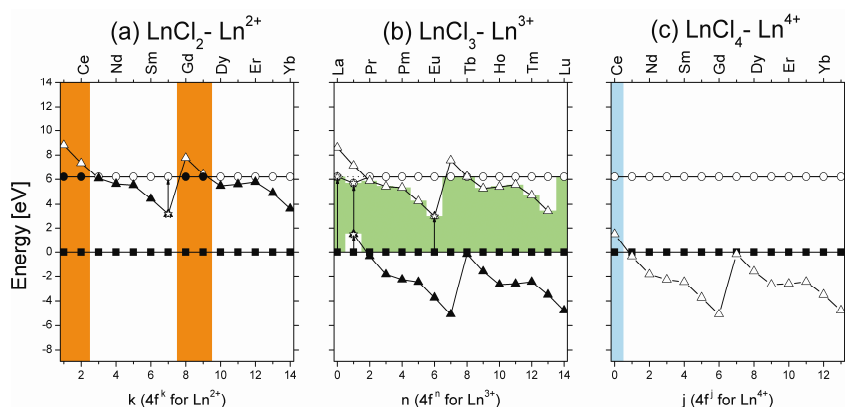
3.2.3. Lanthanide bromides.

In figure 3.3a the level scheme for the lanthanide dibromides ($LnBr_2$) is shown. As for the chlorides, useable experimental information on the electronic structure is scarce. The 4f(2+) ground state curve was placed using information from a lanthanide doped inorganic compound, in this case $SrBr_2$:Eu. The 5d-CB was placed relative to the VB by assuming that this energy difference is similar to the 4p-VB to 5d-CB energy of $LaBr_3$. $NdBr_2$, $SmBr_2$, $EuBr_2$, $DyBr_2$, $TmBr_2$ and $YbBr_2$ are all known to be semiconducting [3, 22-26] as is indeed predicted by our level scheme. Fig. 3.3a also predicts that $PrBr_2$, $HoBr_2$ and $ErBr_2$ could be prepared as semiconducting compounds. Metallic behaviour is predicted for $LaBr_2$, $CeBr_2$, $GdBr_2$ and $TbBr_2$. Of these only metallic $LaBr_2$ has been successfully prepared according to literature [18, 27].

The level scheme for the lanthanide tribromides ($LnBr_3$) is shown in figure 3.3b. The scheme is quite similar to that of the trichlorides, albeit with a shift to

lower energies of the divalent and trivalent 4f ground state energies and the 5d-CB energy, relative to the top of the 4p-VB.

No lanthanide tetrabromides are known exist. If the same assumptions are made for the tetrabromides as were made for $LnCl_4$, figure 3.3c can be drawn. As seen for the tetrachlorides, only $CeBr_4$ with the empty $4f^1$ state 1eV above the 4p-VB could possibly exist, although $CeBr_4$ would be even less stable than $CeCl_4$.

Figure 3.3. Predicted electronic structures of the binary Ln bromides (Ln=La to Lu): a) Ln dibromides ($LnBr_2$): orange shading = metallic compounds; b) Ln tribromides ($LnBr_3$): light green shading = optical bandgap; c) Ln tetrabromides ($LnBr_4$): Light blue vertical bands = stable compounds. In all figures squares = 4p-VB, circles = 5d-CB, and triangles = 4f ground state. Filled symbols indicate an occupied band. Stars and arrows indicate the experimental data used.
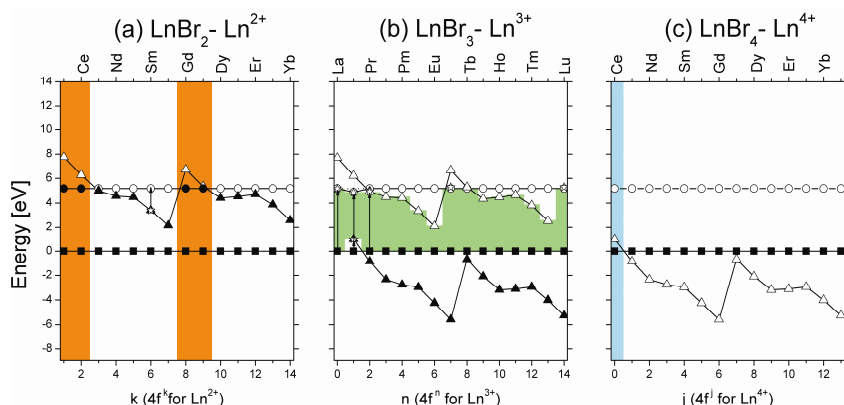
3.2.4. Lanthanide iodides.

The lanthanide iodides exist in both a divalent and a trivalent form. The energy level scheme for the lanthanide diiodides (LnI_2) is shown in figure 3.4a. The 4f(2+) ground state to 5d-CB energy was taken from optical data on EuI_2 as indicated by the vertical arrow at k=7. Using this value gives a scheme in Fig 3.4a that predicts NdI_2, SmI_2, EuI_2, DyI_2, TmI_2 and YbI_2 to be semiconducting materials, and this agrees with what has been observed experimentally [18, 28]. PrI_2 is known to exist in five different crystal modifications. In four of these, PrI_2 appears to be semiconducting, while in one modification it appears

metallic [29, 30]. The close proximity of the $4f^3$ ground state to the 5d-CB which is predicted for PrI_2 by our scheme corresponds well with such behaviour. Apparently in most modifications the 5d-CB is just above the 4f ground state whereas in one modification it is below. It is likely that the semiconducting phases of PrI_2 will show metal-insulator switching behaviour under pressure.

NdI_2 and DyI_2 are also predicted to be switchable materials because their 4f(2+) ground state energies are located just below the 5d-CB. Indeed NdI_2 is known to switch continuously from a semiconductor to a metal under pressure between 10 and 20 kbar [31]. HoI_2 and ErI_2 are predicted to exist as semiconductors but no information could be found on the existence of these compounds. Metallic LaI_2, CeI_2 and GdI_2 have also been reported [29, 32, 33] and the level schemes indeed predict these compounds to be metallic with the 4f ground state lying inside the 5d-CB. TbI_2, which we also predict to be metallic, has not been synthesized yet as far as we know.
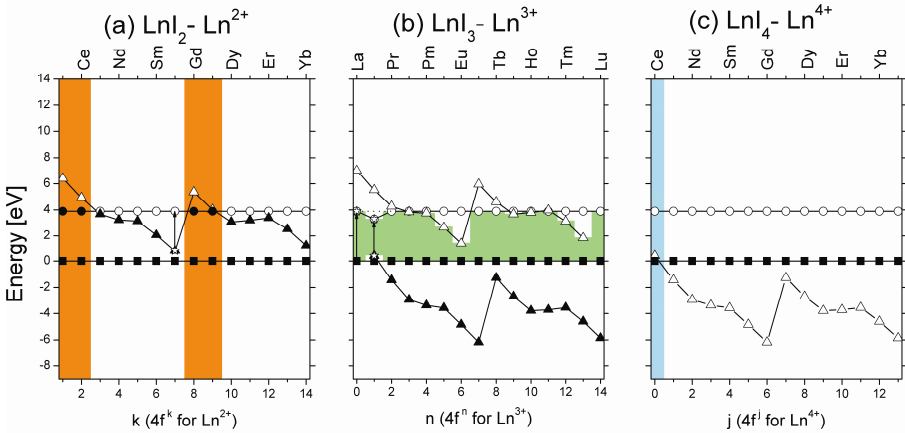

Figure 3.4. Predicted electronic structures of the binary Ln iodides (Ln=La to Lu): a) Ln diiodides (LnI_2): orange shading = metallic compounds; b) Ln triiodides (LnI_3): light green shading = optical bandgap; c) Ln tetraiodides (LnI_4): Light blue vertical bands = stable compounds. In all figures squares = 5p-VB, circles = 5d-CB, and triangles = 4f ground state. Filled symbols indicate an occupied band. Stars and arrows indicate the experimental data used.

The energy level scheme of the lanthanide triiodides (LnI_3) is shown in figure 3.4b. The results are similar to those of the lanthanide trichlorides and tribromides, albeit with a further shift of the 4f(2+) and the 4f(3+) ground state curves and the 5d-CB to lower energies relative to the mp-VB. The energy level scheme for the lanthanide tetraiodides shown in figure 3.4c has been predicted using the same assumption as was made for the $LnCl_4$ and $LnBr_4$ compounds. The unoccupied 4f(3+) ground state of CeI_4 is 0.4eV above the 5p-VB which will make the compound extremely unstable. We are not surprised that no reports on CeI_4 were found in the archived literature.

3.3. Lanthanide chalcogenides

The lanthanide chalcogenides range from wide bandgap semiconductors such as La_2O_3 to metallic compounds like CeS. From our literature survey we found that the trivalent lanthanide oxides are the materials that have undergone the most diverse optical investigations. These oxides along with the tetravalent LnO_2 and divalent LnO and LnS compounds were the subject of a previous investigation [34] and were revisited using the updated 4f(2+) and 4f(3+) ground state curves as was explained in chapter 2. The data used to compile the schemes for the lanthanide oxides may also be found there, while the data used for the other chalcogenides may be found in table 3.2

3.3.1. Lanthanide oxides.

The energy level schemes of the three lanthanide oxides (LnO, Ln_2O_3 and LnO_2) were introduced in chapter 2 in figures 2.2a through 2.2c. Figure 2.2a shows the energy level scheme for the divalent lanthanide monoxides LnO. Optical data for EuO (see table 1 and references therein) was used to position the 4f ground state with respect to the 5d-CB and the 2p-VB. The resulting scheme suggests that apart from EuO, only YbO can exist as a semiconducting compound, and this prediction agrees with what has been observed elsewhere [52, 53]. All other lanthanide monoxides are predicted to be metallic which is also what is found in practice [54-56]. Even in the case of SmO, where the

4f(2+) ground state level is only 0.05eV from the bottom of the 5d-CB, the scheme correctly predicts the metallic phase [57].

Table 3.2. Sources of the photoelectron (XPS, UPS) and optical (transmission, reflection, luminescence) experimental data for the 2+, 3+ and 4+ binary sulfides, selenides and tellurides used in this work to construct the energy level diagrams presented in figures 3.5 to 3.7. "?" means that no information on that transition was available, est. means that the transition was estimate, while "n/a" means not applicable, meaning that the transition is not meaningful in that scheme.

	Ln^{x+} (x=)	mp to 2+ 4f	mp to 3+ 4f	mp to 5d	4f-5d
LnS	2	2.95eV SmS [35, 36]	n/a	?	0.25eV SmS [37]
LnSe	2	2.4eV SmSe, 1.1eV EuSe [38-40]	n/a	?	1.62eV EuSe [41]
LnTe	2	1.9eV SmTe [39]	n/a	?	0.82eV SmTe [37]
Ln_2S_3	3	2.15eV Sm_2S_3[42]	-6eV Gd_2S_3[43, 44]	2.7eV La_2S_3, Dy_2S_3, Ho_2S_3 [45-47]	1.9eV Ce_2S_3 [48]
Ln_2Se_3	3	1.76eV Sm_2Se_3 [49]	?	2.3eV La_2Se_3 [50]	1.85eV Ce_2Se_3 [50]
Ln_2Te_3	3	0.4eV Eu_2Te_3 est.	0.3eV Ce_2Te_3 est.	2.2eV La_2Te_3 [51]	?
LnS_2	4	n/a	0.6eV CeS_2 est.	2.7eV est.	n/a
$LnSe_2$	4	n/a	0.45eV $CeSe_2$ est.	2.3eV est.	n/a
$LnTe_2$	4	n/a	0.3eV $CeTe_2$ est.	2.2eV est.	n/a

The trivalent lanthanide sesquioxides presented in figure 2.2b are the most studied of all the binary lanthanide compounds. The optical bandgap values predicted by our level scheme are all within 0.3eV of the values derived from diffuse reflectance spectra in the papers by Borchardt and White [58, 59]. Their experimental data is indicated in figure 2.2b by blue and red horizontal bars.

The scheme for the tetravalent lanthanide dioxides is shown in figure 2.2c. The only experimental data available is the energy of the VB to 4f transition of CeO_2. In an earlier paper it was predicted that both NdO_2 and DyO_2 should exist although no reports confirming their existence had been found [34]. However when we apply the refined curves from Fig 2.1, the unoccupied 4f(3+)

ground states of these compounds are predicted at or below the top of the valence band suggesting that rather than being too unstable to synthesize, these compounds are actually non-existent.
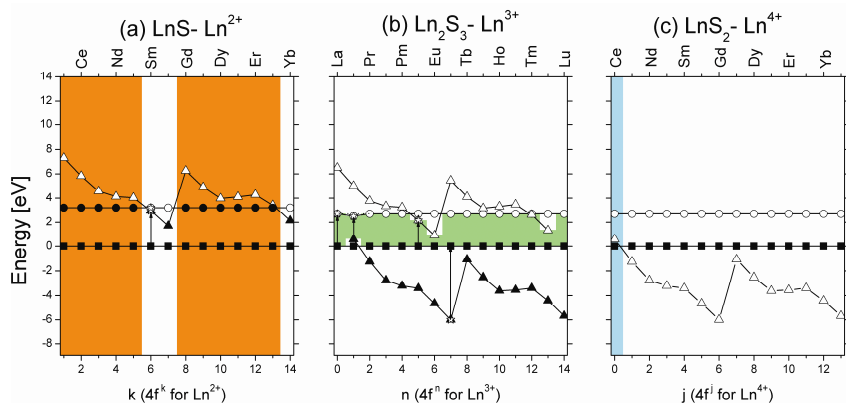
Figure 3.5. Predicted electronic structures of the binary Ln sulfides (Ln=La to Lu): a) Ln monosulfides (LnS): orange shading = metallic compounds; b) Ln sesquisulfides (Ln$_2$S$_3$): light green shading = optical bandgap; c) Ln disulfides (LnS$_2$): Light blue vertical bands = stable compounds. In all figures squares = 3p-VB, circles = 5d-CB, and triangles = 4f ground state. Filled symbols indicate an occupied band. Stars and arrows indicate the experimental data used.

3.3.2. Lanthanide sulfides.

The energy level scheme for the divalent lanthanide monosulfides (LnS) is shown in figure 3.5a. When experimental data on SmS (see table 3.2 and references therein) is used to construct the scheme, the model correctly predicts semiconducting or metallic behaviour as function of the number of electrons in 4f. Like the monoxides EuO and YbO, EuS and YbS are semiconducting [52, 53]. SmS is well known for its semiconductor to metal phase transition at relatively low pressures. In our scheme its 4f(2+) ground state energy is 0.25eV below the 5d conduction band making it indeed semiconducting at ambient conditions. TmS is the heavy lanthanide analogue to SmS and has its 4f(2+) ground state level lying 0.2eV above the 5d-CB, which leads us to predict metallic behaviour. Both observations agree with what have been observed experimentally [37, 60].

The energy level scheme for the trivalent lanthanide sesquisulfides (Ln_2S_3) is shown in figure 3.5b. The sesquisulfides have all been synthesized with the exception of Pm_2S_3 and Eu_2S_3 .[61] The schemes suggest that Eu_2S_3 should exist but the location of the unoccupied 4f(2+) ground state level only 0.9eV above the valence band is most likely the reason why it is difficult or even impossible to prepare.
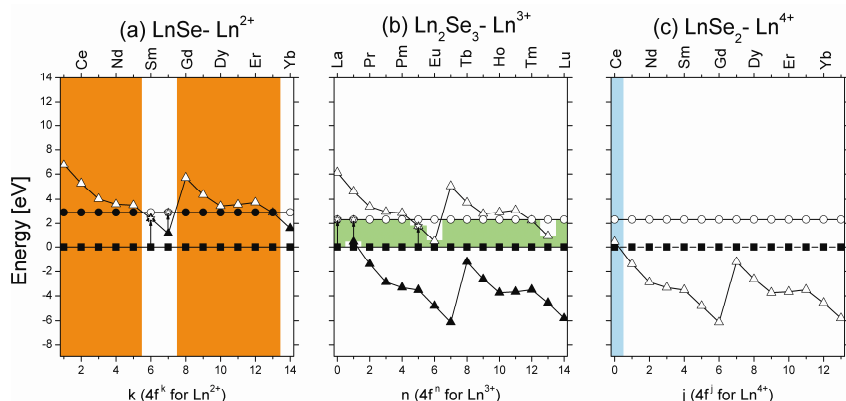

Figure 3.6. Predicted electronic structures of the binary Ln selenides (Ln=La to Lu): a) Ln monoselenides (LnSe): orange shading = metallic compounds; b) Ln sesquiselenides (Ln_2Se_3): light green shading = optical bandgap; c) Ln diselenides (LnSe$_2$): Light blue vertical bands = stable compounds. In all figures squares = 4p-VB, circles = 5d-CB, and triangles = 4f ground state. Filled symbols indicate an occupied band. Stars and arrows indicate the experimental data used.

No reports on the synthesis of tetravalent lanthanide disulfides were found. If we assume that the unoccupied 4f(3+) ground state levels of the lanthanide disulfides are at approximately the same energy as the occupied 4f(3+) ground state energies in the Ln_2S_3 scheme, then only CeS_2 might exist as is shown in figure 3.5c. However, an energy difference of only 0.6eV between the unoccupied 4f(3+) ground state energy and the 3p-VB would reduce the 4+ valence of Ce very easily to the 3+ valency and our scheme then suggests that CeS_2 cannot be prepared. Interestingly, the existence of layered compounds with the formula LnS_2 (Ln=La…Nd, Gd) has been reported [62-65]. The

crystal structure of these compounds consists of layers of $Ln^{3+}S^{2-}$ alternating with layers of covalently bonded S_2^{2-} sulfur complexes. Similar types of compounds were reported for the diselenides and ditellurides [63, 64]. This suggests that tetravalent CeS_2 will be difficult to prepare because of the more stable CeS_2 layered compound alternative containing trivalent Ce.

3.3.3. Lanthanide selenides.

The energy level scheme for the divalent lanthanide monoselenides (LnSe) is shown in figure 3.6a. The constructed energy level scheme presents a consistent picture in which only SmSe, EuSe and YbSe are predicted to be semiconducting, which is confirmed by the experimental data found for these compounds [37, 52, 66]. Indeed while the 1.64eV 4f(2+) to 5d-CB transition of EuSe is used to position the 5d-CB with respect to the 4f(2+) ground state, the model correctly predicts the 4f to 5d bandgaps of SmSe and YbSe to within 0.3eV [37, 67, 68]. All the other lanthanide monoselenides are metallic. Even the intermediate valence behaviour of TmSe [39, 60, 69] where the Tm ion fluctuates between a 2+ and a 3+ charge state due to the close proximity of the 4f(2+) ground state energy to the 5d-CB, is predicted correctly by our model. The energy level scheme for trivalent lanthanide sesquiselenides is shown in figure 3.6b. As the energy level locations are practically identical to those of the sesquisulfides they are not further discussed.

If it is assumed that the position of the unoccupied 4f(3+) ground state levels of $LnSe_2$ are at approximately the same energy as the occupied 4f(3+) ground state in Ln_2Se_3 with respect to the top of the VB, then it follows that only $CeSe_2$ may exist as is shown in figure 3.6c. As is the case with the sulfides, the 0.45eV energy difference between the unoccupied Cerium 4f(3+) ground state and the top of the valence band suggests that this compound is very unstable. Similarly to the lanthanide disulfides, layered polyselenides with the formula $LnSe_2$ (Ln=La...Nd) consisting of layers of LnSe alternating with layers of Se_2^{2-} molecular complexes have been synthesized [63, 64, 70]. Therefore it can

be suggested that tetravalent $CeSe_2$ will be difficult to prepare because of the more stable layered $CeSe_2$ compound which contains Ce^{3+} rather than Ce^{4+} ions.

3.3.4. Lanthanide tellurides.

The energy level scheme for the divalent lanthanide monotellurides is shown in figure 3.7a.The overall pattern is similar to that of the monoselenides and SmTe, EuTe and YbTe are predicted to be semiconducting [52, 71]. There are slight differences due to a somewhat lower energy of the 4f(2+) ground state energies with respect to the 5d-CB energy. As a result TmTe is a semiconducting compound that can be switched to its metallic phase by application of pressure [60]. The other LnTe compounds are predicted to be metallic.
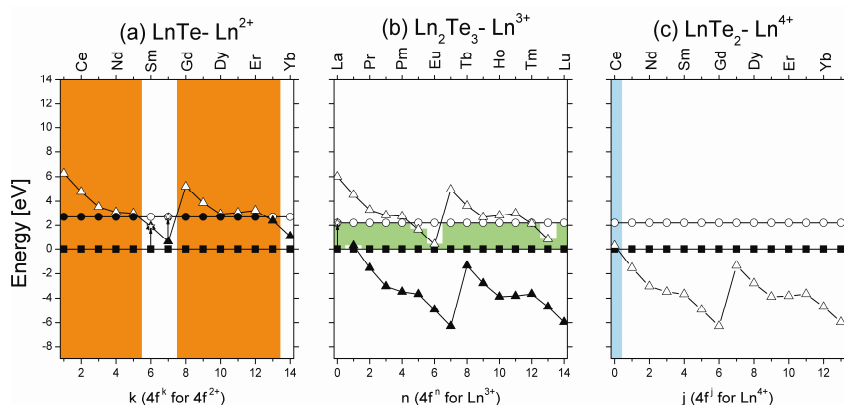
Figure 3.7. Predicted electronic structures of the binary Ln tellurides (Ln=La to Lu): a) Ln monotellurides (LnTe): orange shading = metallic compounds; b) Ln sesquitellurides (Ln_2Te_3): light green shading = optical bandgap; c) Ln ditellurides ($LnTe_2$): Light blue vertical bands = stable compounds. In all figures squares = 5p-VB, circles = 5d-CB, and triangles = 4f ground state. Filled symbols indicate an occupied band. Stars and arrows indicate the experimental data used.

The energy level scheme for the lanthanide sesquitellurides is shown in figure 3.7b. Unfortunately there was no data found that could be used to position the 4f(2+) and 4f(3+) ground state energy curves. Instead we estimate the relative positions of these curves using trends in the position of the curves for the other

sesquichalcogenides and for the lanthanide monochalcogenides. The scheme for the lanthanide sesquioxides shown in figure 2.2b in chapter 2 and those for the sesqui-sulfides and selenides shown in figures 3.5b and 3.6b show that the 4f(2+) and 4f(3+) curves of the lanthanide sesquichalcogenides move closer to or deeper inside the VB when the anion changes from O, to S, to Se. The same trend is observed for the 4f(2+) curve of the lanthanide monochalcogenides, see Fig. 2.2a, 3.5a, 3.6a and 3.7a. By combining these two trends we estimated the location of the 4f(2+) and 4f(3+) curves in Fig. 3.7b for Ln_2Te_3. The scheme and therefore also the properties predicted for the sesquitellurides is very similar to those of the sesquiselenides.

Figure 3.7c shows our predicted scheme for the lanthanide ditellurides. It is more or less a copy of the Ln_2Te_3 scheme where the occupied 4f(3+) levels have been changed into unoccupied ones. The scheme suggests that only $CeTe_2$ could energetically be stable although it would be even less stable than $CeSe_2$ because the empty 4f(3+) state of Ce^{3+} is predicted to be 0.15 eV closer to the top of the valence band. As with the disulfides and diselenides, the tetravalent ditellurides have never been synthesized, instead layered $LnTe_2$ (Ln=La…Pr, Sm, Gd) compounds are formed [64, 72-75] involving Te_2^{2-} complexes. Of these, $LaTe_2$ and $CeTe_2$ are the most widely investigated as they are charge density wave compounds [76].

3.4. Lanthanide pnictides

Of all the binary lanthanide compounds, the least experimental data was found for the pnictides as can be seen in table 3.3. Only examples of the trivalent monopnictides (LnN, LnP, LnAs and LnSb) and divalent Ln_3P_2 and Ln_3As_2 are known to exist. The divalent europium pnictides Eu_3P_2 and Eu_3As_2 are semiconductors while the properties of the trivalent pnictides range from narrow band semiconductors such as LaN to semimetals like the lanthanide antimonides.

3.4.1. Lanthanide nitrides.

Figure 3.8 shows the energy level scheme for the lanthanide nitrides. Of all the possible binary lanthanide nitrides only data on compounds of the form LnN have been published. The corresponding energy level scheme, shown in figure 3.8b, was constructed using XPS data that defines the energy of the Ce 4f(3+) ground state relative to the N 2p-VB. The 2p-VB to 5d-CB energy of DyN, HoN and ErN were used to place the 5d-CB relative to the valence band. While the 4f(2+) curve was positioned using data on YbN. The energy of the Ce 4f(3+) ground state, which lies less than 0.1eV below the bottom of the 5d-CB in the scheme, explains why CeN is a metallic intermediate valence compound as demonstrated by Baer and Zurcher [80].

Table 3.3. Sources of the photoelectron (XPS, UPS) and optical (transmission, reflection, luminescence) experimental data for the 2+, 3+ and 4+ binary pnictides used in this work to construct the energy level diagrams presented in figures 3.8 to 3.11. "?" means that no information on that transition was available, est. means that the transition was estimate, while "n/a" means not applicable, meaning that the transition is not meaningful in that scheme.

	Ln^{x+} (x=)	mp to 2+ 4f	mp to 3+ 4f	mp to 5d	4f-5d
Ln_3N_2	2	2eV Eu_3N_2 est.	n/a	3eV Eu_3N_2 est.	1eV Eu_3N_2 est.
Ln_3P_2	2	?	n/a	2.2eV Eu_3P_2 [77]	1.2eV Eu_3P_2 [77]
Ln_3As_2	2	?	n/a	2eV Eu_3As_2 [78]	1.2eV Eu_3As_2 [78]
Ln_3Sb_2	2	0.7eV Eu_3Sb_2 est.	n/a	1.9eV Eu_3Sb_2 est.	1.2eV Eu_3Sb_2 est.
LnN	3	1.7eV YbN [79]	1.4eV CeN [80]	1.5eV DyN, HoN, ErN [81]	?
LnP	3	1.1eV YbP [82]	0.7eV CeP [83]	1.1eV NdP, SmP, HoP [82, 84]	?
LnAs	3	1.05eV YbAs [85]	0.4eV CeAs [83]	1.05 average [85, 86]	?
LnSb	3	0.1eV EuSb est.	0eV CeSb [80]	0.55eV PrSb, SmSb [85]	?
Ln_3N_4	4	n/a	1.4eV Ce_3N_4 est.	1.5eV Ce_3N_4 est.	n/a
Ln_3P_4	4	n/a	0.7eV Ce_3P_4 est.	1.1eV Ce_3P_4 est.	n/a
Ln_3As_4	4	n/a	0.4eV Ce_3As_4 est.	1.05eV Ce_3As_4 est.	n/a
Ln_3Sb_4	4	n/a	0eV Ce_3Sb_4 est.	0.55eV Ce_3Sb_4 est.	n/a
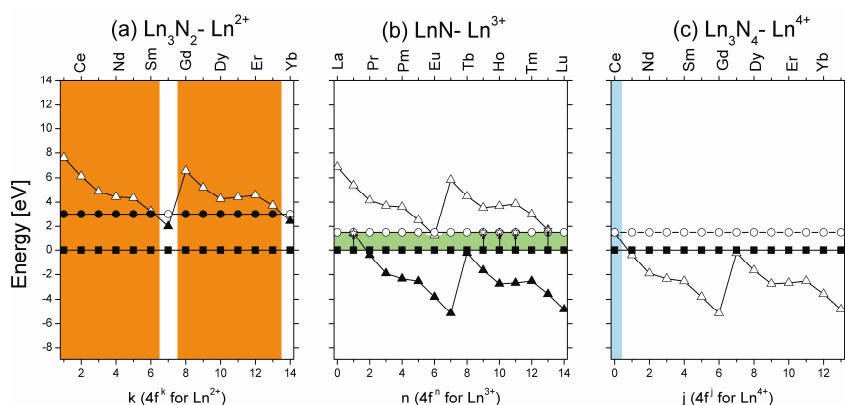
Figure 3.8. Predicted electronic structures of the binary Ln nitrides (Ln=La to Lu): a) Ln_3N_2: orange shading = metallic compounds; b) Ln mononitrides (LnN): light green shading = optical bandgap; c) Ln_3N_4: Light blue vertical bands = stable compounds. In all figures squares = 2p-VB, circles = 5d-CB, and triangles = 4f ground state. Filled symbols indicate an occupied band. Stars and arrows indicate the experimental data used.

Figure 3.8a gives an educated guess at the electronic structures of Ln_3N_2 compounds that have not yet been synthesized. The energy level scheme was predicted as follows. First the schemes for the trivalent Ln monopnictides LnN, LnP and LnAs in Fig. 3.8b, 3.9b and 3.10b, and the schemes for the divalent Ln_3P_2 and Ln_3As_2 compounds in Fig. 3.9a and 3.10a were constructed based on available experimental data. The trends found in the energy difference between the 4f(2+) curves and the mp-VB for these compounds were then used to estimate the 4f(2+) curve location in the Ln_3N_2 compounds. A similar method was used to estimate the mp-VB to 5d-CB energy difference of 3eV.

No tetravalent lanthanide nitrides of the form Ln_3N_4 have been reported. Therefore a level scheme was again estimated by assuming that the energy level position of the unoccupied 4f(3+) ground state is at approximately the same energy as the occupied 4f(3+) ground state of the LnN compounds. Basically we copied the scheme for the LnN compounds and changed the occupied 4f(3+) levels into unoccupied ones. This is shown in figure 3.8c. Apart from the energy of the 5d-CB, the scheme resembles that of $LnCl_4$. Like

$CeCl_4$, Ce_3N_4 is the only compound in this series that is predicted to be stable. However neither compound has been synthesized yet.

3.4.2. Lanthanide phosphides.

Figure 3.9a shows the energy level scheme for Ln_3P_2 compounds, constructed using the 3p-VB to 5d-CB and the 4f(2+) ground state to 5d-CB transition energies of Eu_3P_2. The scheme predicts that like Eu_3P_2, Yb_3P_2 should also be semiconducting. However, no data on Yb_3P_2 was found, nor was there any published data on metallic Ln_3P_2 compounds.
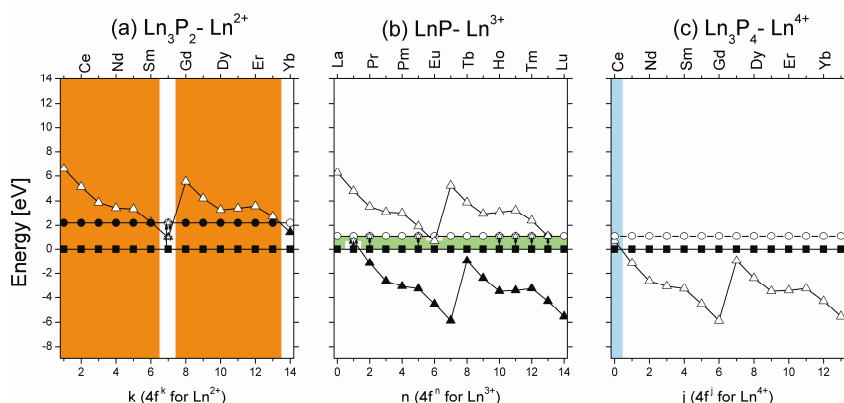
Figure 3.9. Predicted electronic structures of the binary Ln phosphides (Ln=La to Lu): a) Ln_3P_2: orange shading = metallic compounds; b) Ln monophosphides (LnP): light green shading = optical bandgap; c) Ln_3P_4: Light blue vertical bands = stable compounds. In all figures squares = 3p-VB, circles = 5d-CB, and triangles = 4f ground state. Filled symbols indicate an occupied band. Stars and arrows indicate the experimental data used.

Figure 3.9b shows the energy level scheme proposed for the lanthanide monophosphides (LnP). Of all the pnictides most experimental data is available for the monophosphides as can be seen from the arrows in Fig. 3.9b.

Figure 3.9c shows the predicted energy level scheme for Ln_3P_4. We copied the scheme for the LnP compounds and changed the occupied 4f(3+) levels into unoccupied ones. Only Ce_3P_4 is predicted to exist but since the unoccupied 4f(3+) ground state level is only 0.7eV above the 3p-VB it is likely that Ce^{4+} is

unstable against reduction to Ce^{3+} and the compound therefore cannot be synthesized.

3.4.3. Lanthanide arsenides.

The energy level scheme for lanthanide arsenides of the form Ln_3As_2 is shown in figure 3.10a. The scheme is very similar to that of the Ln_3P_2 compounds. Like Eu_3P_2 only Eu_3As_2 is known to exist [78]. The 4f(2+) ground state of Eu is 1.2 eV below the 5d-CB and the compound is semiconducting.
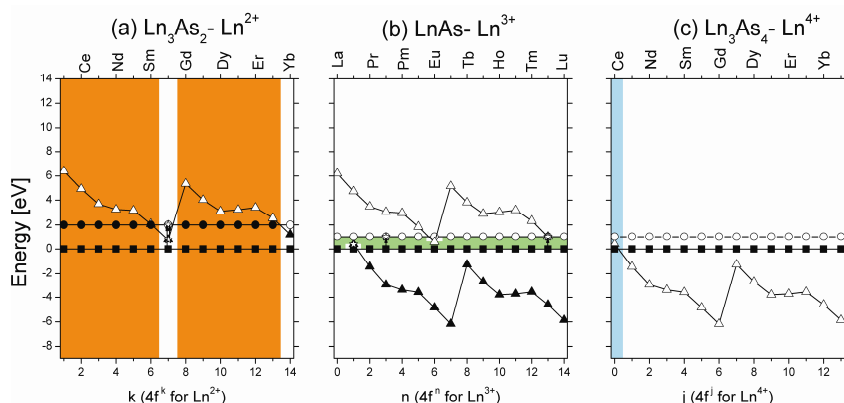
Figure 3.10. Predicted electronic structures of the binary Ln arsenides (Ln=La to Lu): a) Ln_3As_2: orange shading = metallic compounds; b) Ln monoarsenides (LnAs): light green shading = optical bandgap; c) Ln_3As_4: Light blue vertical bands = stable compounds. In all figures squares = 4p-VB, circles = 5d-CB, and triangles = 4f ground state. Filled symbols indicate an occupied band. Stars and arrows indicate the experimental data used.

The energy level scheme for the lanthanide monoarsenides LnAs is shown in figure 3.10b. The scheme predicts that EuAs should exist as a semiconducting Ln^{3+} compound as is the case for EuN and EuP, and EuAs indeed does exist, but the Eu appears to be present as a 2+ ion rather than a 3+ ion. In addition EuAs has a Na_2O_2 (hexagonal) structure rather than the face centred cubic (FCC) NaCl rock salt structure generally observed for the Ln monopnictides. Iandelli and Franceschi suggested that in EuAs two As ions form As_2^{4-}

complexes [87]. Therefore in this case Eu is divalent and it is better to write the compound as $Eu_2(As_2)$.

Figure 3.10c shows the predicted energy scheme for Ln_3As_4 obtained by copying the scheme for the LnAs compounds and changing the occupied 4f(3+) levels into unoccupied ones. Only Ce_3As_4 is predicted to exist but since the unoccupied 4f(3+) ground state is only 0.4 eV above the valence band Ce^{4+} will be very prone to reduction and the material will therefore be extremely unstable.

3.4.4. Lanthanide antimonides.

No published data on any Ln_3Sb_2 compound was found. Therefore the scheme in figure 3.11a is an educated guess based on trends observed for the pnictides and the chalcogenide compounds. Our energy level scheme suggests that Eu_3Sb_2 and Yb_3Sb_2 are both small bandgap semiconductors.

Figure 3.11. Predicted electronic structures of the binary Ln antimonides (Ln=La to Lu): a) Ln_3Sb_2: orange shading = metallic compounds; b) Ln monoantimonides (LnSb): light green shading = optical bandgap; c) Ln_3Sb_4: Light blue vertical bands = stable compounds. In all figures squares = 5p-VB, circles = 5d-CB, and triangles = 4f ground state. Filled symbols indicate an occupied band. Stars and arrows indicate the experimental data used.
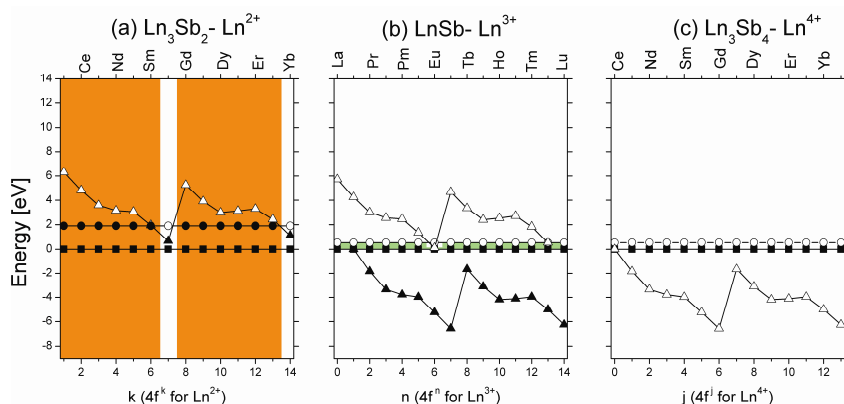
The energy level scheme for the mono-antimonides (LnSb) is shown in figure 3.11b. The unoccupied 4f(2+) ground state energy of Eu^{3+} is calculated to be about 0.1 eV above the top of the valence band by using the 0.55eV 5p-VB to

4f(2+) transition of YbN to place the 4f(2+) curve. Such a small energy difference makes Eu very susceptible to reduction to the divalent state. Like EuAs, EuSb does not contain Eu^{3+} but Eu^{2+} and like the As in EuAS, the Sb in EuSb forms Sb_2^{4-} units that form a bond with divalent Europium [87].

Figure 3.11c shows the predicted energy scheme for Ln_3Sb_4. We simply copied the scheme for the LnSb compounds and changed the occupied 4f(3+) levels into unoccupied ones. Since all these unoccupied states are below the filled valence band none of the Ln_3Sb_4 compounds, including Ce_3Sb_4, can be energetically stable and are therefore non-existent.

3.5. Summary

In this chapter it has been possible to construct schemes that can be used to investigate a wide range of binary lanthanide compounds, from wide band-gap insulators to metals, including the schemes for the oxides shown in chapter 2, this amounts to 512 possible compounds of which 366 are predicted to exist. Of these compounds, 249 actually exist, consisting of 42 metallic or interconfigurational valence materials, 53 semimetals and 154 insulating, semiconducting or switchable materials.

By using these schemes we can, in some cases for the first time, predict the electronic structure and optical bandgap of all of these materials quickly and easily. In chapter 4, the trends uncovered from these schemes will be discussed in more detail.

References

[1]   Freiser M J, Methfessel S and Holtzberg F 1968 *Journal of Applied Physics* **39** 900-2

[2]   Kobayashi T, Mroczkowski S and Owen J F 1980 *Journal of Luminescence* **21** 247-57

[3]   Wood A B, Young J P, Peterson J R and Haschke J M 1981 Absorption spectrophotometric characterization of Sm(II), Sm(III), and Sm(II/III)

bromides and Sm(III) oxybromide in the solid state. In: *15th Rare Earth Research Conference,* (Rolla, MO, USA

[4]   Gahane G H, Kokode N S, Muthal P L, Dhopte S M and Moharil S V 2009 *Optical Materials* **32** 18-21

[5]   Feofilov S P, Zhou Y, Jeong J Y and Keszler D A 2007 *Journal of Luminescence* **122-123** 503-5

[6]   Sato S 1976 *Journal of the physical society of Japan* **41** 913-20

[7]   Klier K, Novák P, Miller A C, Spirko J A and Hatalis M K 2009 *Journal of Physics and Chemistry of Solids* **70** 1302-11

[8]   Popma T J A, van der Weg W F and Thimm K 1981 *Journal of Luminescence* **24-25** 289-92

[9]   Olson C G, Piacentini M and Lynch D W 1978 *Physical Review B* **18** 5740-9

[10]   Dujardin C, Pedrini C, Garnier N, Belsky A N, Lebbou K, Ko J M and Fukuda T 2001 *Optical Materials* **16** 69-76

[11]   Gruen D M, Conway J G and McLaughlin R D 1956 *Journal of chemical physics* **25** 1102-11

[12]   van Loef E V D, Dorenbos P, van Eijk C W E, Krämer K W and Güdel H U 2003 *Physical Review B* **68** 045108

[13]   Birowosuto M D, Dorenbos P, van Eijk C W E, Krämer K W and Güdel H U 2007 *Journal of Physics: Condensed Matter* **19** 256209

[14]   Jungmann A, Claessen R, Zimmerman R, Meng G, Steiner P, Hüfner S, Tratzky S, Stöwe K and Beck H P 1995 *Zeitschrift for Physik B* **97** 25-34

[15]   Bessiere A., Dorenbos P, van Eijk C W E, Krämer K W, Güdel H U, de Mello Donega C and Meijerink A 2005 *Nuclear Instruments and Methods in Physics Research A* **537** 22-6

[16]   Marabelli F, Wachter P and Kaindl G 1992 *Physical Review B* **46** 10012-6

[17]   Stezowski J J and Eick H A 1970 *Inorganic Chemistry* **9** 1102-5

[18]   Haschke J M 1979 *Handbook on the Physics and Chemistry of the Rare Earths: Volume 4 - Non-Metallic Compounds - II,* ed K A Gschneidner and L R Eyring (Amsterdam: North-Holland Publishing Company)

[19]   Beck G and Nowacki W 1938 *Die Naturwissenshaften* **30** 495-6

[20]   Meyer G and Schleid T 1986 *Journal of the less common metals* **116** 187-97

[21]   Lanza G and Fragalá I L 1998 *Journal of Physical Chemistry A* **102** 7990-5

[22]   Hohnstedt C and Meyer G 1993 *Zeitschrift für anorganische und allgemeine Chemie* **619** 1379-83

[23]   Hohnstedt C and Meyer G 1993 *Zeitschrift für anorganische und allgemeine Chemie* **619** 1374

[24]   Sanchez J P, Friedt J M, Bärnighausen H and van Duyneveldt A J 1984 *Inorganic Chemistry* **24** 408-15

[25]   Meyer G 1988 *Chemical Reviews* **88** 93-107

[26]   Beck H G and Bärnighausen H 1971 *Zeitschrift für anorganische und allgemeine Chemie* **386** 221-8

[27]   Kramer K, Schleid T, Mathias S, Urland W and Meyer G 1989 *Zeitschrift für anorganische und allgemeine Chemie* **575** 61-70

[28]   Burrow J H, Maule C H, Strange P, Tothill J N and Wilson J A 1987 *Journal of Physics C: Solid State Physics* **20** 4115-33

[29]   Meyer G and Meyer H-J 1992 *Chemistry of Materials* **4** 1157-68

[30]   Gerlitzki N, Meyer G, Mudring A-V and Corbett J D 2004 *Journal of Alloys and Compounds* **380** 211-8

[31]   Beck H P and Schuster M 1992 *Journal of Solid State Chemistry* **100** 301-6

[32]   Krämer K W, Güdel H U, Fischer P and Keller L 2002 *Applied Physics A.* **74** S595-S7

[33]   Ahn K, Felser C, Seshadri R, Kremer R K and Simon A 2000 *Journal of Alloys and Compounds* **303-304** 252-6

[34]   van der Kolk E and Dorenbos P 2006 *Chemistry of Materials* **18** 3458-62

[35]   Gudat W, Alvarado S F and Campagna M 1978 *Solid State Communications* **28** 943-6

[36]   Chainani A, Kumigashira H, Ito T, Sato T, Takahashi T, Yokoya T, Higuchi T, Takeuchi T, Shin S and Sato N K 2002 *Physical Review B* **65** 155201

[37]   Batlogg B, Kaldis E, Schlegel A. and Wachter P 1976 *Physical Review B* **14** 5503-14

[38]   Suga S, Taniguchi M, Seki M, Sakamoto H, Kanzaki H, Yamamoto M, Kurita A, Kaneko Y and Koda T 1984 *Solid State Communications* **49** 1005-8

[39]   Campagna M, Bucher E, Wertheim G K and Longinotti L D 1974 *Physical Review Letters* **33** 165-8

[40]   Busch G, Cotti P and Munz P 1969 *Solid State Communications* **7** 795-8

[41]   Verreault R 1969 *Solid State Communications* **7** 1653-6

[42]   Glurdzhidze L N, Kekhaiov T D, Bzhalava T L, Dzhabua Z U and Sanadze V V 1979 *Soviet Physics of the Solid State* **21** 2021-3

[43]   Kimura S, Arai F, Tezuka Y, Shin S, Kunii S, Suzuki T and Ikezawa M 1993 *Physica B* **186-188** 89-91

[44]   Kaciulis S, Latisenka A and Plesanovas A 1991 *Surface Science* **251-252** 330-5

[45]   Mauricot R, Dexpert-Ghys J and Evain M 1996 *Journal of Luminescence* **69** 41-8

[46]   Henderson J R, Muramoto M and Lok E 1967 *The Journal of Chemical Physics* **47** 3347-56

[47]   Forster C M and White W B 2005 *Materials Research Bulletin* **41** 448-54

[48]   Mauricot R, Bullot J, Wery J and Evain M 1996 *Materials Research Bulletin* **31** 263-9

[49]   Ivanchenko L A, Pribyl'skaya N Y, Finkel'shtein L D and Efremova N N
        1988 *Poroshkovaya Metallurgiya* **12** 58-61

[50]   Prokofiev A V, Shelykh A I, Golubkov A V and Smirnov I A 1995
        Journal of Alloys and Compounds **219** 172-5

[51]   Bagde G D, Sartale S D and Lokhande C D 2005 *Materials Chemistry
        and Physics* **89** 402-5

[52]   Wachter P 1972 *Critical Reviews in Solid State and Materials Sciences*
        3 189

[53]   Syassen K, Winzen H, Zimmer H G, Tups H and Leger J M 1985
        Physical Review B **32** 8246 -52

[54]   Leger J M, Yacoubi N and Loriers J 1981 *Journal of solid state
        chemistry* **36** 261-70

[55]   Adachi G-y and Nobuhito I 1998 *Chemical Reviews* **98** 1479-514

[56]   Semiletov S A, Imamov R M, Ragimli N A and Man L I 1976 *Thin
        Solid Films* **32** 325-8

[57]   Leger J M, Aimonino P, Loriers J, Dordor P and Coqblin B 1980
        Physics Letters A **80** 325-7

[58]   White W B 1967 *Applied Spectroscopy* **21** 167-71

[59]   Borchardt H J 1963 *The Journal of Chemical Physics* **39** 504-11

[60]   Batlogg B, Kaldis E, Schlegel A and Wachter P 1976 *Physics Letters A*
        56 122-4

[61]   Yuan H, Zhang J, Yu R and Su Q 2009 *Journal of Rare Earths* **27** 308-
        11

[62]   Shleid T, Lauxmann P, Graf C, Bartsch C and Doert T 2009 *Zeitschrift
        fur Naturforschung B* **64** 189-96

[63]   Guittard M and Flahaut J 1991 *Synthesis of Lanthanide and Actinide
        Compounds,* ed G Meyer and L R Morss (Dordrecht: Kluwer Academic
        Publishers) pp 321-52

[64]   Flahaut J 1979 *Handbook on the Physics and Chemistry of the Rare
        Earths,* ed K A Gschneidner and L R Eyring (Amsterdam: North-
        Holland Publishing Company) pp 1-88

[65]   Müller C J, Schwarz U, Schmidt P, Schnelle W and Doert T 2010
         Zeitschrift für anorganische und allgemeine Chemie **636** 947-53

[66]   Suryanarayanan R and Paparoditis C 1970 *Solid State Communications*
         8 1853-5

[67]   Bucher E, Narayanamurti V and Jayaraman A 1971 *Journal of Applied
         Physics* **42** 1741-5

[68]   Wong C C and Wood C 1971 *Physics Letters A* **34** 125-6

[69]   Antonov V N, Harmon B N and Yaresko A N 2002 *Physica B* **312-313**
         373-5

[70]   Doert T and Graf C 2005 *Zeitschrift für anorganische und allgemeine
         Chemie* **631** 1101-6

[71]   Reid F J, Matson L K, Miller J F and Himes R C 1964 *Journal of
         Physics and Chemistry of Solids* **25** 969-76

[72]   Ramsey T H, Steinfink H and Weiss E J 1963 *Journal of Applied
         Physics* **34** 2917-8

[73]   Kang J S, Olson C G, Kwon Y S, Shim J H and Min B I 2006 *Physical
         Review B* **74** 085115

[74]   Stöwe K 2000 *Zeitschrift für anorganische und allgemeine Chemie* **626**
         803-11

[75]   Kwon Y S and Min B I 2000 *Physica B* **281-282** 120-1

[76]   Lavagnini M, Sacchetti A, Degiorgi L, Shin K Y and Fisher I R 2007
         Physical Review B **75** 205133

[77]   Busch G, Hulliger F, Streit P, Wachter P and Wullschleger J 1971
         Journal de Physique Colloque **32** 734-5

[78]   Wachter P and Wullschleger J 1972 *Journal of Physics and Chemistry
         of Solids* **33** 939-43

[79]   Degiorgi L, Basca W and Wachter P 1990 *Physical Review B* **42** 530-9

[80]   Baer Y, Hauger R and Zuercher C 1979 *Journal of Electron
         Spectroscopy and Related Phenomena* **15** 27-32

[81]   Sclar N 1964 *Journal of Applied Physics* **35** 1534-8

[82]   Meng J and Ren Y 1991 *Solid State Communications* **80** 485-8

[83]   Franciosi A, Weaver J H, Martensson N and Croft M 1981 *Physical Review B* **24** 3651-4

[84]   Meng J and Ren Y 1992 *Materials Chemistry and Physics* **30** 235-8

[85]   Hiscocks S E R and Mullin J B 1969 *Journal of Materials Science* **4** 962-73

[86]   Hulliger F 1979 *Handbook on the Physics and Chemistry of the Rare Earths: Volume 4 - Non-Metallic Compounds - II,* ed K A Gschneidner and L R Eyring (Amsterdam: North-Holland Publishing Company) p 163

[87]   Iandelli A and Franceschi E 1973 *Journal of the less common metals* **30** 211-6

Chapter 4: Using an empirical model for the electronic properties of the binary Lanthanide halide, chalcogenide and pnictide compounds to understand material properties

This chapter has been published as part of E. Rogers, P. Dorenbos, E. van der Kolk, Systematics in the optical and electronic properties of the binary lanthanide halide, chalcogenide and pnictide compounds – an overview, New Journal of Physics, 13, 093038, 2011

Abstract.

The basic optical, electrical and chemical properties of the binary divalent, trivalent and tetravalent lanthanide (Ln= La…Lu) halides (F, Cl, Br, I), chalcogenides (O, S, Se, Te) and pnictides (N, P, As, Sb) were studied using an empirical model that utilizes the systematic behaviour in the energy difference between the localized $4f^n$-states, the 5d-derived conduction band and the mp-derived valence band (m=2…5) over the Lanthanide series. As the wide variety in the electrical and optical properties of Ln-materials is to a large extent controlled by the energy of these states relative to each other it is possible to simultaneously predict insulating, semiconducting or metallic behaviour, the nature and magnitude of band-gap energies and the chemical stability of Ln-materials as well as valence and valence changes of Ln-ions. It can thus be used to predict the basic electronic structure of materials for which no experimental data can be found and may be a guideline for theoretical modelling.

4.1. Introduction

In chapter 2 an empirical model was introduced that, given optical or photoelectron data on one compound in a series of lanthanide compounds, for

instance EuO, the electronic structure/ optical bandgap of all compounds in that series, i.e. LnO (Ln = La…Yb) can be predicted to within 0.3eV.

In chapter 3 it was also shown that where no suitable experimental data is available, it is possible to use trends in the position of the energy levels of similar Ln based compounds to predict a scheme.

In this chapter these trends will be examined in more detail, looking at patterns that can be seen in the change in the energy of the Ln 4f ground state and 5d CB as a function of anion. We will also see that the empirical model can be used to explain why some Eu^{3+} compounds do not exist. Finally the model will be compared to that used for lanthanide doped compounds, and future uses of the model will be discussed.

4.2. Observed trends in the level schemes

The universal behaviour of the ground state energies as a function of the number of electrons in the 4f orbital, i.e. the 4f(2+) and 4f(3+) curves from Fig. 2.1 in chapter 2, forms the basis with which to construct the level schemes shown in chapter 3. In addition to these clear trends as a function of the type of lanthanide ion, we occasionally mentioned trends with changing type of anion or with changing lanthanide valency when discussing the schemes in chapter 3. Several of those trends were used to predict schemes in cases where no experimental data was available. We will analyze these trends further below.

Figure 4.1 shows trends in the behaviour of the divalent lanthanide compounds that have an occupied Ln 4f(2+) ground state, such as $LnCl_2$, LnS and Ln_3P_2. Because the energy of the 4f(2+) ground state of Eu^{2+} is usually located between the mp-VB and the 5d-CB, the binary divalent europium compounds (i.e. EuF_2) have been selected to quantify the trends. Figure 4.1a shows the energy of the 5d-CB with respect to the top of the mp-VB. The halides are represented by black squares, the chalcogenides by red circles and the pnictides by green triangles. Data on the halides and on Eu_3N_2 and Eu_3Sb_2 are estimated values. The bandgap decreases in a regular fashion with the increase of the

period (m) of the periodic table that the anion belongs to. It also decreases in going from halides to chalcogenides to pnictides.

Figure 4.1b shows the energy of the 4f(2+) ground state of the Eu^{2+} ion above the top of the mp-VB for the halides, chalcogenides and pnictides and as function of the period (m). We observe similar trends to those seen in Figure 4.1a. Figure 4.1c shows the 4f(2+) to 5d-CB energy difference of the Eu compound predicted for the halides, chalcogenides and pnictides. Note that these results can be derived from Figures 4.1a and 4.1b.

Figure 4.2 shows trends derived from the energy level schemes in figures 2.2b (chapter 2) and 3.1b to 3.11b (chapter 3) for compounds that have an occupied Ln 4f(3+) ground state. Because the optical properties of Ce compounds are most frequently studied and tend to have 4f levels lying above the mp-VB, data on Ce compounds are used to illustrate these trends. Figure 4.2a shows the position of the La (filled symbols) and Ce (half-filled symbols) 5d-CB levels above the top of the mp-VB as predicted by the model for the halides (black squares), chalcogenides (red circles) and pnictides (green triangles). The La and Ce values are shown in this figure due to the differences between the mp-VB to 5d-CB energies measured directly for La compounds and calculated from the sum of the mp-VB to 4f(3+) energy difference and the 4f(3+) to 5d-CB energy observed for Ce compounds. Similar trends to those found in Figure 4.1a are observed.

Figure 4.2b shows the position of the Ce 4f(3+) ground state level above the top of the mp-VB for the lanthanide halides, chalcogenides and pnictides. Figure 4.2c shows the 4f(3+) ground state to 5d-CB transition energy of the binary cerium compounds.
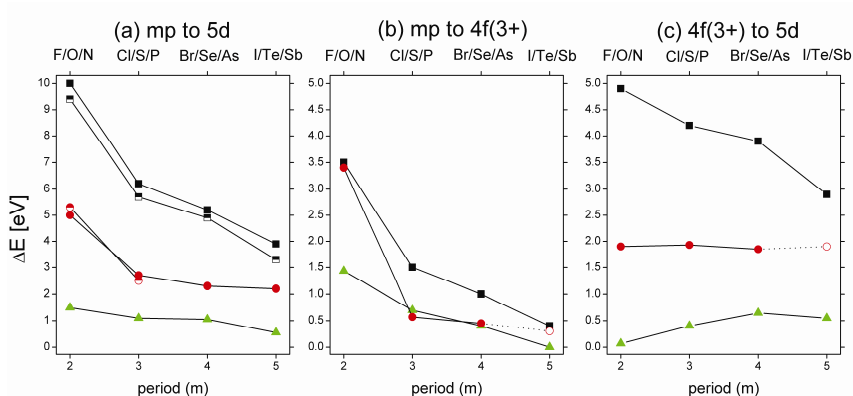
Figure 4.1. Trends found in the schemes for the divalent compounds: a) *m*p-VB→5d-CB energy difference, b) *m*p-VB→4f(2+) energy difference, c) 4f(2+) ground state→5d-CB energy difference, black squares = halides, red circles = chalcogenides and green triangles = pnictides. Unfilled symbols indicate estimated values.
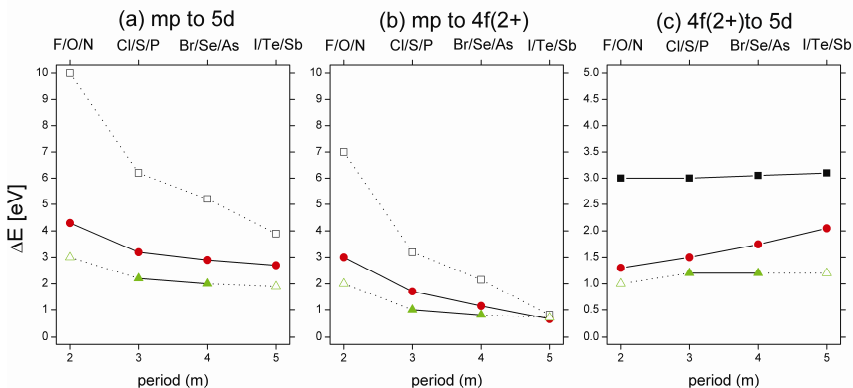
Figure 4.2. Trends found in the schemes for the trivalent compounds: a) *m*p-VB→5d-CB energy difference, b) *m*p-VB→4f(3+) energy difference, c) 4f(3+) ground state→5d-CB energy difference, black squares = halides, red circles = chalcogenides and green triangles = pnictides. Unfilled symbols indicate estimated values and half filled symbols indicate the *m*p→5d energy difference of compounds where the 4f(3+) ground state lies above the *m*p band.

For both the divalent and trivalent Ln ions, the 5d-CB, 4f(2+) and 4f(3+) energies decrease with respect to the top of the *m*p-VB when we go horizontally in the periodic table from halides to chalcogenides to pnictides, but

also when we go vertically i.e. from F to Cl to Br to I. This is related to the electronegativity of the anions which decreases in the same sequence. Paulings electronegativity is 3.98, 3.44, and 3.04 for F, O, and N, respectively, and it is 3.98, 3.16, 2.96, and 2.66 for F, Cl, Br, and I, respectively [1]. The 4f and 5d energy differences in Fig. 4.1c and 4.2c are determined by the crystal field interaction and the covalence of the compound. These aspects have been studied in detail for lanthanide activated compounds [2-6] and will not be further addressed in this work.

This work reveals that the binary lanthanide compounds display simple systematic behaviour in electronic structure over the Ln-series (La, Ce, Pr,…,Lu). The simplicity originates from two important aspects of Ln-compounds. The first is the double zigzag curves of the variation in 4f ground state energy with type of lanthanide as presented in figure 2.1. They are universal in the sense that they do not change with the type of Ln-material. The second is the invariance of the 5d energy with changing lanthanide ion. This causes the mp-VB to 5d-CB to be constant as a function of the type of Ln-ion.

There also appears to be much similarity between the divalent, trivalent, and tetravalent level schemes within a compound series like LnO-Ln_2O_3-LnO_2 or LnI_2-LnI_3-LnI_4. On one hand the energies of the mp-VB, the 5d-CB and the 4f ground state with respect to each other are different for each series of lanthanide compounds and have to be established using experimental data. On the other, these energies appear surprisingly similar within a series of compounds. For example the schemes in Figure 2.2 in chapter 2 for LnO, Ln_2O_3, and LnO_2 all appear similar, the only difference between them is whether lanthanide states are occupied or not. For LnO_2 the 4f(3+) states are empty. The scheme for Ln_2O_3 is practically the same as that of LnO_2 but with occupied 4f(3+) states. Going to the scheme of LnO, an extra electron is added to the lanthanides and either the 4f(2+) state or the 5d-CB is being occupied, but again the energies of the 2p-VB, the 5d-CB and the 4f(2+) and/or 4f(3+) ground state with respect to each other appear similar to the other Ln oxides. In

predicting level schemes, particularly for the pnictides where very little or no experimental data was available for some compounds, we frequently made use of these similarities.

4.3. The stability of some binary lanthanide materials

Many possible binary Ln compounds do not as yet exist. The schemes in chapter 3 predict that trivalent Eu and Yb compounds such as EuI_3, Eu_2S_3, Eu_2Se_3, Eu_2Te_3, Yb_2Te_3, EuAs and EuSb can exist based on energy level considerations but no reports were found on their existence. One reason for this could be the presence of more favourable alternatives. Europium sulfides, selenides and tellurides (chapter 3 figs. 3.5b, 3.6b, 3.7b) form divalent EuX or mixed valence Eu_3X_4 compounds rather than trivalent Eu_2X_3 (X=S, Se, Te), while EuAs and EuSb form divalent compounds of the form $Eu_2^{2+}X_2^{2-}$ (X= As, Sb) where there is a covalent bond between two As or Sb ions (chapter 3, figs. 3.10 and 3.11) rather than the trivalent rock salt structures found for the other Ln monopnictides.

However there appears to be a trend in the existence/nonexistence of trivalent Ln compounds. Looking at the non-existing compounds EuI_3, Eu_2S_3, Eu_2Se_3, Eu_2Te_3, Yb_2Te_3, EuAs and EuSb, we note that with the exception of EuAs, the energies of the unoccupied 4f(2+) states are located at less than 40% of the mp-VB to 5d-CB bandgap above the mp-VB in our schemes which in absolute terms means that they are all located less than 1.4eV above the valence band. Apparently under such conditions the 3+ valence state is not stable against reduction to 2+ during synthesis of the compound and the 3+ lanthanide compound is not formed.

Almost all tetravalent lanthanide compounds are predicted by our model not to exist. Exceptions are several compounds within the lanthanide tetrafluoride (LnF_4) and dioxide (LnO_2) families as can be derived from figures 3.1c and 2.2c, respectively. All of the lanthanide dioxides that we predict to be stable indeed do exist. The use of the refined 4f(2+) and 4f(3+) curves, see chapter 2

fig. 2.1, in the level schemes of this work clears up an issue from our previous work, where, in addition to CeO_2, PrO_2 and TbO_2, the model predicted that the non-existent NdO_2 and DyO_2 would be stable [7].

The divalent lanthanide monochalcogenides are the most complete of all the series studied regarding their stability. With the exception of the Pm monochalcogenides, all of the monosulfides, monoselenides and monotellurides have been prepared (chapter 3 figs. 5a, 6a and 7a) and most of the lanthanide monoxides (chapter 2 fig. 2.2a) have also been prepared. These compounds include semiconductors such as EuO, mixed valence compounds such as TmSe and metallic compounds like GdS, and the nature of these compounds, whether they are semiconducting, mixed valence or metallic, has been correctly modelled by our schemes. TbO, HoO and TmO have not been reported in literature but there is no reason to believe that with the proper synthesis conditions they would not exist as FCC metals like the other isostructural metallic monoxides.

The situation for the lanthanide dihalide materials is more complex than that observed for the monochalcogenides. Figures 3.1a, 3.2a, 3.3a and 3.4a in chapter 3 predict that compounds like NdF_2, $LaCl_2$, $PrBr_2$ and HoI_2 should exist as semiconductors if we only take the positions of their energy levels into consideration. However reports that they have been prepared were not found. This suggests that aspects other than energy level location also determine whether a compound can be synthesized or not. One such aspect might be the crystal structure which should be energetically stable. The lanthanide monochalcogenides all exhibit the same face centred cubic NaCl type structure, but the lanthanide dihalides show a great deal of variety of crystal structure. Several of the dihalide compounds are polymorphic and PrI_2 has five different crystal structures, one of which corresponds to a metallic phase [8, 9]. With the exception of the difluorides, which are all isostructural, the semiconducting dihalides can be divided into light and heavy lanthanide compounds. The light

lanthanide compounds from NdX_2 to EuX_2 have crystal structures with a larger anion co-ordination number around the lanthanide ion than that seen for the heavier DyX_2 to YbX_2 compounds. In addition, while both the monochalcogenide and dihalide series contain materials that undergo semiconductor to metal phase transitions under pressure, switchable monochalcogenides undergo an isostructural transition to a metallic phase, while switchable NdI_2 undergoes a structural change during its semiconductor to metal transition [10]. All this suggests that the crystal structure and therefore the co-ordination number of the cations complicate the chemical behaviour of the dihalide series compared to that of the lanthanide monochalcogenides.

It is interesting to note that the metallic di- bromides, chlorides and fluorides, do not exist while most metallic monochalcogenides do. This is probably due to the highly oxidizing behaviour of the anion, leading to the far higher stability of the trivalent LnX_3 compound compared to its LnX_2 counterpart. Clearly this is not considered by our model which is primarily designed to predict the electronic structure.

Of the lanthanide dihalides the diiodides (chapter 3 fig. 3.4a) are probably the most interesting to consider when regarding the existence or non-existence of nominally divalent compounds. Although there is little spectroscopic data available for the diiodides, there is a wealth of crystallographic and electrical data available on both semiconducting and metallic compounds and this data matches well with what is expected on the basis of the energy level scheme shown in figure 3.4a. However no experimental data could be found on TbI_2, HoI_2 or ErI_2 and no explanation for their non-existence can be found from our model. We predict TbI_2 to be metallic while HoI_2 and ErI_2 are suggested to be semiconductors. Our model shows several lighter lanthanide compounds with similar electronic properties: CeI_2, PrI_2 and NdI_2 respectively, and these have been prepared. Sadly then, the mystery behind the current non-existence of these materials is beyond the scope of this model.

Finally we look at the divalent lanthanide pnictides. Here only two ionically bonded compounds are known to exist, Eu_3P_2 and Eu_3As_2. However mixed valence Sm, Eu and Yb compounds, which are not covered in this paper, are found in the Ln-LnX (X= As, Sb) series and the review by Hulliger gives a good overview of these [11]. Because there is little data available, we cannot say for certain whether or not the other ionically bonded divalent pnictides are possible. As the trivalent LnX phase is so stable, only the semiconducting Eu and Yb versions such as Eu_3N_2 are likely to be possible.

4.4. The relationship between lanthanide activated and binary lanthanide compounds

The method used in this work to construct level schemes such as those in chapter 3 is derived from the method developed for lanthanide doped inorganic compounds and many of the features and trends observed are similar too. Figure 4.1b shows the location of the Eu^{2+} 4f(2+) ground state energy above the top of the mp-VB. In Eu^{3+} doped compounds this location is obtained from the so-called charge transfer band in the excitation spectrum of Eu^{3+} emission. Here an electron is excited from the top of the anion mp-VB to the Eu^{3+} ion, so that the final state of the Eu ion is Eu^{2+} and there is a hole in the valence band. A compilation on charge transfer energies in Ref. [12] comprises almost 200 different halide, chalcogenide, and nitride compounds. The trend in the mp-VB$\rightarrow Eu^{3+}$ CT energy with the type of anion in the compounds reported there is basically the same as that which we observe in Fig. 4.1b.

The energy differences between the 4f and 5d-CB states of Eu^{2+} or Ce^{3+} binary lanthanide compounds summarized in Fig. 4.1c and Fig. 4.2c show the same trends and patterns as those observed for Eu^{2+} doped [13] and Ce^{3+} doped [5, 6] inorganic compounds. The 4f to 5d-CB energy difference is determined by the splitting of the 5d states due to the crystal field interaction plus the shift of the average energy of the 5d configuration relative to that of the free (gaseous) lanthanide ions. The splitting and shift in turn depend on the size and shape of

the anion coordination polyhedron around the lanthanide and on the amount of covalency between the lanthanide and its neighbouring anion ligands, respectively. The details are very compound specific. For example, the increase in $4f(2+)\rightarrow5d$-CB energy of Eu^{2+} with the period (m) for EuO, EuS, EuSe, and EuTe in Figure 4.1c is also observed for Eu^{2+} doped in CaO, CaS, CaSe and in SrO, SrS, and SrSe [13]. It was attributed to the increasingly larger size of the anion in going from O, to, S, to Se, to Te. This leads to a decrease in the crystal field splitting of the 5d states and consequently a larger $4f(2+)\rightarrow5d$ energy.

Inspecting the schemes in chapter 3 one may notice that the energy difference between the $4f^n$ ground state of Ln^{3+} with that of the $4f^{n+1}$ ground state of Ln^{2+} is about 8 eV for the fluoride compounds but appears significantly smaller for the chalcogenide and pnictide compounds. This is further illustrated in Figure 4.3 for all of the binary Eu compounds. The Europium halides are represented by black squares, the chalcogenides by red circles and the pnictides by green triangles. Values that were estimated are represented by unfilled symbols.

The energy difference is known as the Coulomb correlation or Coulomb interaction energy U_{ff} between two 4f electrons [14, 15]. It is determined by the Coulomb repulsion between the two electrons in the same orbital at the same cation site. For free (or gaseous) Eu ions, $U_{ff}(Eu)$ is the same as the difference between the third and fourth ionization potential of Eu and it amounts to about 18 eV [16, 17]. In Eu metal U_{ff} reduces to a value of about 5.4 eV. This large reduction has been attributed to electronic screening and ionic relaxation in the metal phase [14, 15]. From the work on lanthanide doped inorganic compounds it was found that $U_{ff}(Eu)$ depends on the type of compound. For our most thoroughly studied compound YPO_4, $U_{ff}(Eu)$ appears to be 7.0 eV [18]. For the poorly polarizable fluoride compounds there are strong indications that $U_{ff}(Eu)$ is larger at around 7.5-8 eV whereas it decreases to values around 6eV in strongly polarizable compounds like $LaBr_3$ and $CaGa_2S_4$. Figure 4.3 illustrates that the same trend appears to apply for the binary lanthanide compounds shown in the schemes in Figures 2.2 and 3.1 to 3.11.
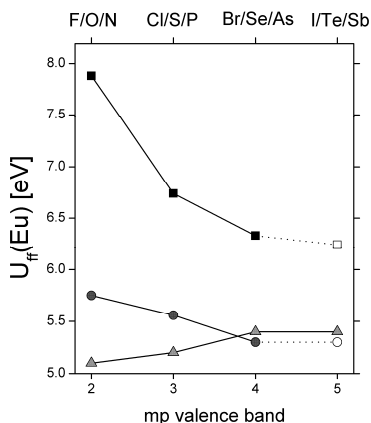
Figure 4.3. The Coulomb correlation energy $U_{ff}(Eu)$ of the binary europium compounds. Squares = halides (EuX_3), circles = chalcogenides (Eu_2X_3), triangles = pnictides (EuX). Empty symbols are estimated values.

Figure 4.3 shows that $U_{ff}(Eu)$ for the halides and chalcogenides decreases with the period (*m*). Clearly the larger polarizability of the anion with increase of *m* leads to larger screening effects and the reduction of the correlation energy $U_{ff}(Eu)$. The same applies when going from the halides to the chalcogenides, i.e., an O^{2-} anion is more strongly polarizable and provides stronger screening than an F^- anion. For the pnictides we observe a somewhat reversed behaviour, i.e., $U_{ff}(Eu)$ tends to increase from N to P to As to Sb. However, the errors involved in the schemes especially for this family of compounds may well be of the order of 0.5 eV and therefore the observed trend is not significant. Interestingly, $U_{ff}(Eu)$ for the most polarizable (m=4 and 5) chalcogenides and pnictides in Figure 17 approaches the same value of around 5.5 eV of Eu metal. It suggests that the effects of screening in those compounds on U_{ff} are similar. We regard the observed trends in $U_{ff}(Eu)$ and the quantitative correspondence with U_{ff} in Eu metal and Eu doped inorganic compounds as strong support for the schemes presented in chapter 3.

4.5. Comparison with ab initio methods

Finally we should consider how this method compares with others used to calculate the electronic structures of Ln compounds. In a recent publication by Petit *et al.* the electronic structures of Ln monochalcogenides and monopnictides, LnX (X=O, S, Se, Te, Po, N, P, As, Sb, Bi), were calculated using *ab initio* methods [19]. It is interesting to compare their results with those presented here as the two methods are so different. While Petit *et al.* use an *ab initio* method: the self-interaction corrected local spin density (SIC-LSD) energy functional, our method relies on experimental data. Both models can successfully predict the valencies of binary Ln compounds but there are differences regarding the predicted bandgaps and the semiconducting/metallic nature of some compounds. However the model presented here has been shown to be able to accurately predict the bandgap of binary Ln compounds. It can also be easily applied to compounds with different crystal environments within minutes, so long as appropriate experimental data is available. Therefore, while ab-initio methods are more elegant than our empirical method, our method is able to give quite accurate results very quickly and at this stage is more applicable for use in the search for new Ln based materials.

4.6. Conclusion and outlook

This work involves the implementation of an empirical model or technique, based on previously collected experimental data, which is able to organize in a consistent way a huge body of scattered experimental data. These compounds vary from wide bandgap insulators, through semiconductors, to metallic compounds, showing that the model can be successfully applied to predict and explain a wide range of materials.

The application of the model explicitly reveals that the wide variety of properties seen for the binary lanthanide compounds can be reproduced with great accuracy by applying two simple empirical rules: (i) the mp-VB to 5d-CB energy is constant over the lanthanide series and (ii) the lanthanide 4f-GS

energy follows a material independent double-seated shaped curve over the lanthanide series as shown in figure 1. These empirical rules result in the observed systematic and universal behaviour of the optical, electrical and chemical properties of binary lanthanide materials as a function of the Ln ion.

The relative energies of the mp-VB, 5d-CB and 4f-GS observed as a function of the type of ligand follow a clear trend that was noted before for smaller subgroups of materials like the Ce pnictides but are now presented for all binary lanthanides. These trends can be explained in a first approximation by the Pauling electronegativity of the ligands and the crystal field splitting of the 5d-CB. These trends have successfully been used to predict the electronic structure of those binary Ln materials for which no experimental data was available.

The presented data on the binary Ln materials convincingly reveal that methods for Ln-ion doped materials, recently developed by one of us in the field of luminescence, can be used to understand and predict electrical and optical properties of fully concentrated lanthanide materials. It is also possible to work in the other direction, using knowledge on concentrated lanthanide materials to predict the luminescence properties of Ln-ions as dopants in materials.

Our energy level schemes also reveal that the relative energies of the mp-VB, 5d-CB and 4f-GS do not change significantly when the stoichiometry of a certain material (i.e. LnO, Ln_2O_3, LnO_2) changes. The difference between stoichiometries is in the filling of either the 4f or 5d-CB of the 2+,3+ or 4+ Ln energy levels. This allows one to predict properties of for example a tetravalent Ln-material like CeO_2 from the optical gap of a trivalent material like Pr_2O_3.

We have strong indications that the approach presented here for the binary Ln-materials is also applicable to ternary materials with the general formula $Ln_xM_yL_z$ (Ln=lanthanide, M=closed shell cation and L=pnictides, chalcogenide or halide ligands) as long as the cations are optically inactive which is the case for monovalent Li, Na, K,.., divalent Mg, Ca, Sr,…, or trivalent Sc or Y. This is also the case for trivalent ions like B, Al, Ga,…, tetravalent ions like C, Si and Ge, pentavalent ions like P, As, Sb or hexavalent ions like S.

The model may serve as a reliable tool for material scientists to accelerate the design of Ln-materials with deliberately chosen properties. Unlike *ab initio* based models, this empirical model can be applied immediately, without any further specialist knowledge, by other material scientists to explain and predict the properties of their favourite Ln-materials.

References

[1] Allred A L 1961 *Journal of Inorganic and Nuclear Chemistry* **17** 215-21

[2] Jörgensen C K 1971 *Modern Apsects of Ligand field Theory* (Amsterdam: North Holland)

[3] Morrison C A 1980 *Journal of Chemical Physics* **72** 1001-2

[4] Görller-Walrand C and Binnemans K 1996 *Handbook on the Physics and Chemistry of Rare Earths,* ed K A Gschneidner Jr. and L Eyring (Amsterdam: Elsevier Science B.V.)

[5] Dorenbos P 2000 *Physical Review B* **62** 15640-9

[6] Dorenbos P 2000 *Physical Review B* **62** 15650-9

[7] van der Kolk E and Dorenbos P 2006 *Chemistry of Materials* **18** 3458-62

[8] Meyer G and Meyer H-J 1992 *Chemistry of Materials* **4** 1157-68

[9] Gerlitzki N, Meyer G, Mudring A-V and Corbett J D 2004 *Journal of Alloys and Compounds* **380** 211-8

[10] Beck H P and Schuster M 1992 *Journal of Solid State Chemistry* **100** 301-6

[11] Hulliger F 1979 *Handbook on the Physics and Chemistry of the Rare Earths: Volume 4 - Non-Metallic Compounds - II,* ed K A Gschneidner and L R Eyring (Amsterdam: North-Holland Publishing Company) p 163

[12] Dorenbos P 2005 *Journal of Luminescence* **111** 89-104

[13] Dorenbos P 2003 *Journal of Luminescence* **104** 239-60

[14] Hüfner S and Wertheim G K 1973 *Physical Review B* **7** 5086-90

[15]   Herbst J F, Lowy D N and Watson R E 1972 *Physical Review B* **6** 1913-24

[16]   Dorenbos P 2009 *Journal of Alloys and Compounds* **488** 568-73

[17]   Thiel C W, Sun Y and Cone R L 2002 *Journal of Modern Optics* **49** 2399-411

[18]   Bos A J J, Dorenbos P, Bessière A and Viana B 2008 *Radiation Measurements* **43** 222-6

[19]   Petit L, Tyer R, Szotek Z, Temmerman W M and Svane A 2010 *New Journal of Physics* **12** 113041

Chapter 5: Experimental study of the $4f^n \rightarrow 4f^n$ and $4f^n \rightarrow 4f^{n-1}5d^1$ transitions of the Lanthanide Diiodides LnI_2 (Ln = Nd, Sm, Eu, Dy, Tm, Yb)

Abstract

The diffuse reflectance and photoluminescence (PL) spectra of NdI_2, SmI_2, EuI_2, DyI_2, TmI_2 and YbI_2 were measured between 640 and 12500nm and 240 to 1400nm respectively in order to determine their $4f^n \rightarrow 4f^{n-1}5d^1$ optical bandgaps. The results were compared with those obtained using an empirical model of the electronic structure of LnI_2. The results can be used to explain the lanthanide valency and crystalline structure changes of other lanthanide diiodides such as PrI_2.

5.1. Introduction

The lanthanide diiodides, LnI_2, where Ln is La, Ce… Tm, Yb, are quite well known binary lanthanide compounds that have been the subject of numerous investigations into their structure, electrical properties etc. They can be divided into two groups, those with a divalent lanthanide ion: NdI_2 (at low pressure), SmI_2, EuI_2, DyI_2, TmI_2 and YbI_2, and those with a trivalent Ln ion: LaI_2, CeI_2 and GdI_2 [1-3]. PrI_2 has five polymorphs, some of which contain Pr^{2+} while others contain Pr^{3+} [4]. The first group can be written as $Ln^{2+}(I^-)_2$ and are semiconducting or insulating compounds while the second group can be written as $Ln^{3+}(I^-)_2 + e^-$ with the extra electron in the Ln 5d conduction band providing metallic properties [1].

The divalent Ln diiodides show a range of interesting properties. SrI_2: Eu, which resembles EuI_2, is an outstanding scintillator due to its excellent energy resolution and high light yield [5-7]. Beck and Schuster showed that NdI_2 exhibits a simultaneous structural and semiconductor to metal phase transition between 1 and 2 GPa of hydrostatic pressure, while Friedt *et al.* showed that an impure sample of DyI_2, while semiconducting below 0°C, switches to a metallic phase at increasing temperatures [8, 9]. These suggest that NdI_2 and DyI_2 are possible switchable materials.

It is of interest to know and understand the optical properties of these compounds as they aid in understanding their electronic structure and thus their unusual properties. The lanthanide diiodides with Ln^{2+} ions have partially filled 4f bands lying between the occupied I 5p valence band and the empty Ln 5d conduction band [4, 10]. The first lower energy optical transitions that are seen therefore are either the interconfigurational $4f^n \rightarrow 4f^{n-1}5d^1$ or the intraconfigurational Ln $4f^n \rightarrow 4f^n$ transitions.

Previously an empirical model, originally used to determine the electronic structures and optical properties of Ln doped compounds, [11, 12] was used to investigate the binary lanthanide halides, chalcogenides and pnictides with 2+, 3+ and 4+ valencies [10]. The model uses an experimentally derived 4f-electron binding energy curve. It has a double zigzag shape as function of the number of electrons in the 4f-shell and enables the positioning of the 4f levels of a series of compounds relative to their mp-valence (m=2…5) and 5d conduction bands. Optical data like luminescence excitation, transmission or diffuse reflectance are needed to determine the optical bandgap of one compound in the series, which can then be used to predict the optical bandgaps of all other compounds in that series. In our previous investigation it was found that while there were plenty of data available for many of the series of compounds studied, the optical properties of the diiodides were largely unknown. Therefore the optical bandgaps were estimated on the basis of optical data on SrI_2:Eu.

In this chapter the diffuse reflectance of NdI_2, SmI_2, EuI_2, DyI_2, TmI_2 and YbI_2 and the photoluminescence (PL) spectra of SmI_2, EuI_2, TmI_2 and YbI_2 are presented. From these data we determine the optical bandgaps of the compounds and use these in concert with an empirical model in order to present a more complete picture of the optical properties and electronic structure of all of the lanthanide diiodides from La to Yb.

5.2. Experiment

NdI_2, SmI_2, EuI_2, DyI_2, TmI_2 and YbI_2 powders (99.9% purity) from Sigma Aldrich were used. As the powders are both air and water sensitive, they were stored in a N_2 filled glove box when not in use. The phase purity of the samples was checked using X-ray diffraction by a PANalytical X'Pert Pro MPD X-ray diffractometer. A significant amount of LnI_3 was observed for most of the samples. No lanthanide sesquioxide (Ln_2O_3) phase was found. The specially designed sealed sample holder used for all measurements in this investigation is shown in figure 5.1. It is similar in design to one by Dai *et al.* [13], and consists of a container for the powder designed to fit in a Pike EasyDiff diffuse reflectance accessory. A window is placed on top of the sample and held in place by a cover that is screwed into place by hand. The windows used were either quartz or ZnSe (for diffuse reflectance only) of 1mm thickness and 12mm diameter. An o-ring was used in order to provide an airtight seal.

Diffuse reflectance was measured using the sample holder and beam blocker in a Bruker Vertex 80V Fourier Transform (FT) spectrometer. By using different combinations of light sources (W lamp and Globar), beamsplitters (CaF_2 and KBr), and detectors (GaP, Si, InGaAs, and MCT), it was possible to measure between 0.1 and 2eV (12500 and 620nm). In order to reduce specular reflectance from the windows, a beam blocker was placed further down the optical path on the outside of the accessory as shown in figure 5.1. It was

possible in this way to reduce any artifacts due to specular reflectance from the windows from the measured diffuse reflectance spectra.

Laser excited emission spectra were investigated using the Bruker Vertex 80V FTIR by exciting the sealed powder samples with second and third harmonic of a tuneable Ti:sapphire laser at wavelengths ranging from between 240 and 960nm. Si and InGaAs detectors were used along with a CaF_2 beamsplitter. Photoluminescence emission and excitation spectra were measured using a VUV/UV/VIS home build dedicated emission set-up detailed in reference 14 [14]. In order to correct for the wavelength dependent intensity of the xenon light source used, Sodium Salicylate was used as a reference below 350nm, while a Si photodiode was used to record the lamp spectrum above this region.
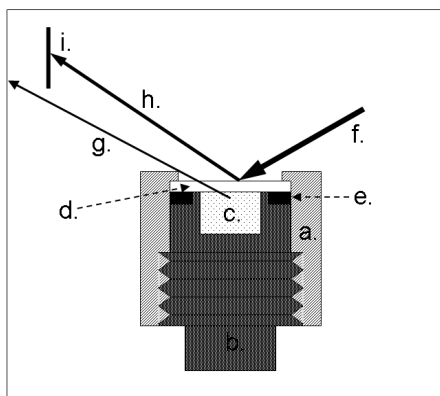
Figure 5.1. Sample holder (not to scale): a) outer cover, b) sample holder, c) sample, d) window, e) o-ring, f) incoming beam, g) diffusely reflected light, h) specularly reflected light, i) beam blocker

5.3. Results

5.3.1. Diffuse Reflectance

Figure 5.2A shows the diffuse reflectance spectrum measured for NdI_2. It shows an absorption edge starting around 0.49 ± 0.02eV (2530nm) that we attribute to the $4f^4 \rightarrow 4f^3 5d^1$ transition of NdI_2. Also present are a series of

absorption lines marked by red circles that can be attributed to the Nd^{2+} $4f^n \rightarrow 4f^n$ transitions [15] which are also displayed diagrammatically in figure 5.5, and a series of weaker transitions marked by blue squares that represent the Nd^{3+} $4f^n \rightarrow 4f^n$ transitions, suggesting the presence of Nd^{3+} impurities in the sample, or a NdI_3 second phase.

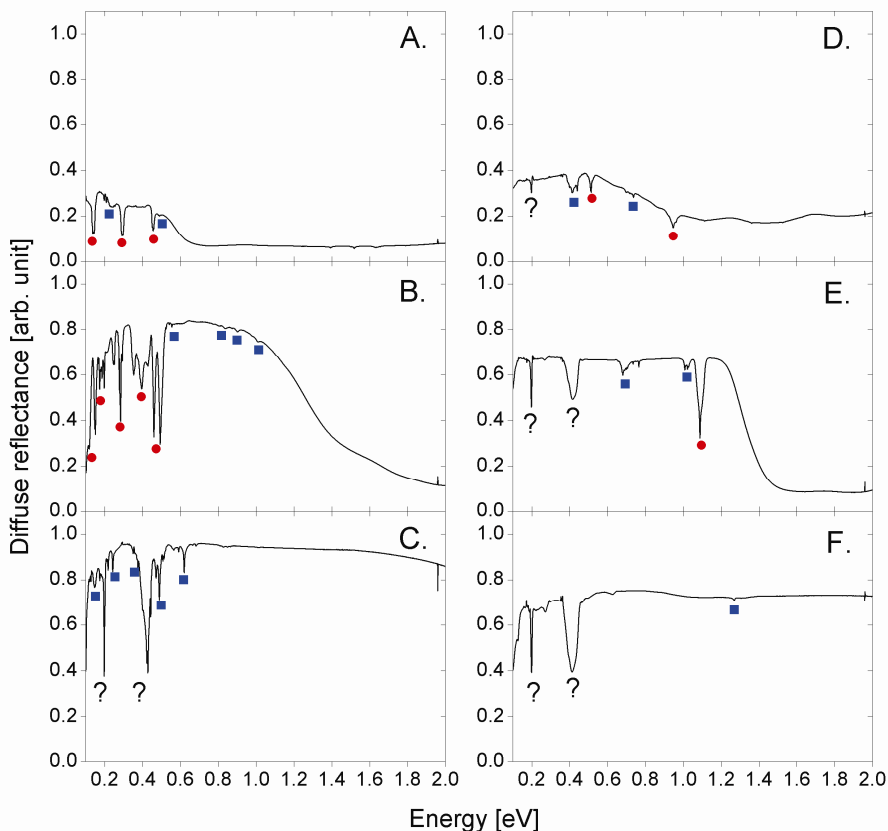Figure 5.2B shows the diffuse reflectance spectrum measured for SmI_2. An absorption edge is found at $1.01 \pm 0.05 eV$ (1230nm). The absorption edge is not as steep as that observed for TmI_2 and NdI_2 and there is evidence of another absorption band above $1.6 eV$ (775nm). Strong dips in the spectrum indicated by red circles can be attributed to Sm^{2+} $4f^n \rightarrow 4f^n$ transitions [15, 16], while the presence of some weak lines, identified as Sm^{3+} $4f^n \rightarrow 4f^n$ transitions are marked with blue squares and suggest the presence of a small amount of Sm^{3+} in the sample, or a SmI_3 second phase.

Figure 5.2C shows the diffuse reflectance spectrum measured for EuI_2. The spectrum exhibits dips that we attribute to the presence of Eu^{3+} which are marked with blue squares as well as others that are not due to any lanthanide $4f^n \rightarrow 4f^n$ transition which are indicated by "?" symbols.

Figure 5.2D shows the diffuse reflectance spectrum measured for DyI_2. There is an absorption edge around $0.51 \pm 0.05 eV$ (2430nm) that can be attributed to the $4f^{10} \rightarrow 4f^9 5d^1$ transition of DyI_2. The sharp dips in the spectrum marked by red circles have been attributed to the $^5I_8$ to $^5I_6$ and $^5I_8$ to $^5I_7$ $4f^n \rightarrow 4f^n$ transitions of Dy^{2+} [15, 17], while the dips labelled with blue squares in the figure can be attributed to $Dy^{3+} 4f^n \rightarrow 4f^n$ transitions due to impurities such as DyI_3.

Figure 5.2E shows the diffuse reflectance spectrum measured for TmI_2. An absorption edge is seen at around $1.23 \pm 0.02 eV$ (1008nm) that can be attributed to the $4f^{13} \rightarrow 4f^{12} 5d^1$ transition of TmI_2. The strong dip around $1.09 eV$ can be attributed to the $^2F_{7/2} \rightarrow ^2F_{5/2}$ transition of Tm^{2+} [15, 18], while weaker dips correspond with Tm^{3+} $4f^n \rightarrow 4f^n$ transitions, suggesting that Tm^{3+} impurities, most probably from TmI_3, are present in the sample. The dips marked "?" cannot be attributed to either Tm^{2+} or Tm^{3+}.

Figure 5.2. Diffuse reflectance spectra of A) NdI$_2$, B) SmI$_2$, C) EuI$_2$, D) DyI$_2$, E) TmI$_2$ and F) YbI$_2$. Red circles indicate Ln^{2+} 4f^n→4f^n transitions, blue squares indicate Ln^{3+} 4f^n→4f^n transitions and "?" indicates that a transition is of unknown origin. Magenta lines and arrows indicate how and where the absorption edge was assigned.

Figure 5.2F shows the diffuse reflectance spectrum measured for YbI$_2$. The dip labelled with a blue square can be attributed to the Yb^{3+} ^{2}F$_{7/2}$→^{2}F$_{5/2}$ transition, suggesting that Yb^{3+} impurities are present in the sample while the dips marked "?" cannot be identified as lanthanide 4f^n→4f^n transitions. The presence of Ln^{3+} intraconfigurational transitions in all of the samples studied is a very strong indication that they are not phase pure. In addition there were several other features, labelled "?" in figure 5.2. These appear in many of the samples and at the same energies and may be an indication that water is present.
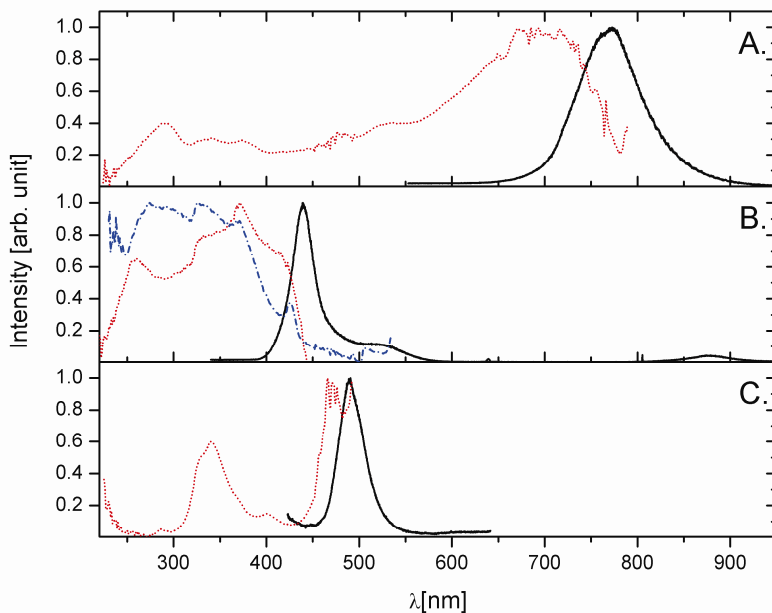
5.3.2. Emission and excitation

Figure 5.3 shows emission and excitation spectra for SmI_2, EuI_2, and YbI_2. As TmI_2 exhibits emission outside the sensitivity range of the available detector, the emission of TmI_2 excited using a Ti:sapphire laser at 450nm was measured using a Bruker Vertex 80V FT spectrometer and is shown in figure 5.4.

In figure 5.3A the photoluminescence emission and excitation spectra of SmI_2 are shown. The emission spectrum consists of one broad peak centred at around 770nm that we attribute to $4f^5 5d^1 \rightarrow 4f^6$ emission. The excitation spectrum monitoring the emission at 800nm shows a broad absorption band at 695 nm that we can attribute to the $4f^6 \rightarrow 4f^5 5d^1$ bands.

In figure 5.3B the PL emission and excitation spectra of EuI_2 are shown. The emission consists of a strong peak centred at 440nm and a smaller peak at around 515nm. The excitation spectra corresponding to these peaks are significantly different suggesting that the two emission peaks have different origins. The peak at 440nm is attributed to $4f^6 5d^1 \rightarrow 4f^7$ emission from the regular Eu^{2+} crystallographic site. The excitation spectrum relating to this peak consists of two peaks attributed to $4f^7 \rightarrow 4f^6 5d^1$ transitions, superimposed on a broad background. The drop in the excitation spectrum below 250nm is possibly due to the $4p \rightarrow 5d$ transition of EuI_2. The peak around 515nm may be from Eu^{2+} ions at a defect site caused by the presence of Eu^{3+} in the sample and the related charge compensation.

Finally the optically stimulated emission and excitation spectra of YbI_2 are shown in figure 5.3C. The emission spectrum shows a strong peak at 490nm, which can be attributed, in the same way as the other spectra measured, to the $4f^{13} 5d^1 \rightarrow 4f^{14}$ transition of YbI_2. However the excitation spectrum is quite different to the other two compounds studied. The spectrum consists of two well separated peaks, either due to the crystal field splitting of the $4f^{14} \rightarrow 4f^{13} 5d^1$ transition of YbI_2 which has a different crystal structure than SmI_2 and EuI_2, or to excitation to the higher energy Yb $4f^{13}(^2F_{5/2})5d^1$ state rather than the expected $4f^{13}(^2F_{7/2})5d^1$ state.

Figure 5.3. Optical excitation and emission spectra of: A. SmI_2: red dots = excitation (λ_{em}=800nm), black = emission (λ_{ex}=483nm); B. EuI_2: red dots = excitation (λ_{em}=451nm), blue dash-dots = excitation (λ_{em}=549nm), black = emission (λ_{ex}=320nm); C. YbI_2: red dots = excitation (λ_{em}=510nm), black = emission (λ_{ex}=345nm).

In figure 5.4 the emission spectrum of TmI_2 after excitation at 450nm is shown. Unlike the spectra measured for SmI_2, EuI_2 and YbI_2, the emission spectrum measured for TmI_2 consists of a sharp spike at 1140nm. This suggests that the emission measured is $4f^{13} \rightarrow 4f^{13}$ emission rather than $4f^{13} \rightarrow 4f^{12}5d^1$ emission. In the diffuse reflectance measurements it was seen that the Tm^{2+} $^2F_{7/2} \rightarrow {}^2F_{5/2}$ transition lay just below the $4f^n \rightarrow 4f^{n-1}5d^1$ optical gap. It is then likely that after excitation into the Tm^{2+} 5d state, the electron relaxes to the Tm^{2+} $^2F_{5/2}$ level before returning to the ground state radiatively.
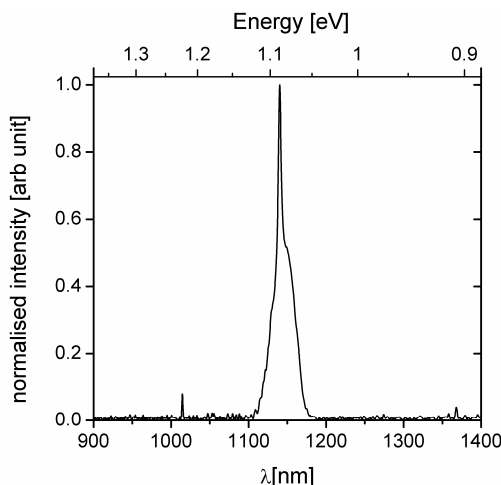
Figure 5.4. Emission spectrum of TmI_2 powder after excitation by a Ti:sapphire laser at 450nm

5.4. Discussion

The $4f^n \rightarrow 4f^{n-1}5d^1$ transitions established optically in this work have been analyzed using an empirical model that was developed for Ln doped compounds by Dorenbos [11, 12]. The model was later shown to be applicable to the binary Ln oxides and the Ln monosulfides in a study by van der Kolk and Dorenbos [19]. In chapters 2 to 4 it was shown that the model can be extended to cover all of the binary Ln halides, chalcogenides and pnictides containing Ln ions with 2+, 3+ and 4+ valencies [10]. It was shown that the model is applicable to a wide range of compounds from insulators and semiconductors to mixed valence, semi-metallic and metallic compounds [10].

The model can be described by the following three statements. Firstly, the electron binding energy at the top of the anion mp band, where m is 2 for F, O and N, 3 for Cl, S and P, 4 for Br, Se and As, 5 for I, Te and Sb is defined as 0, and used as an anchoring point for the binding energy scheme.

Secondly, as the 5d band is delocalized, its energy, relative to the mp band is independent of the Ln ion studied, i.e. from Ce to Pr to Nd to Tm and Yb.

Finally, it can be shown that the change in energy of the 4f ground state follows a distinctive zigzag pattern as a function of cation, which remains invariant (i.e. from Sm to Eu to Gd) no matter what type of compound.
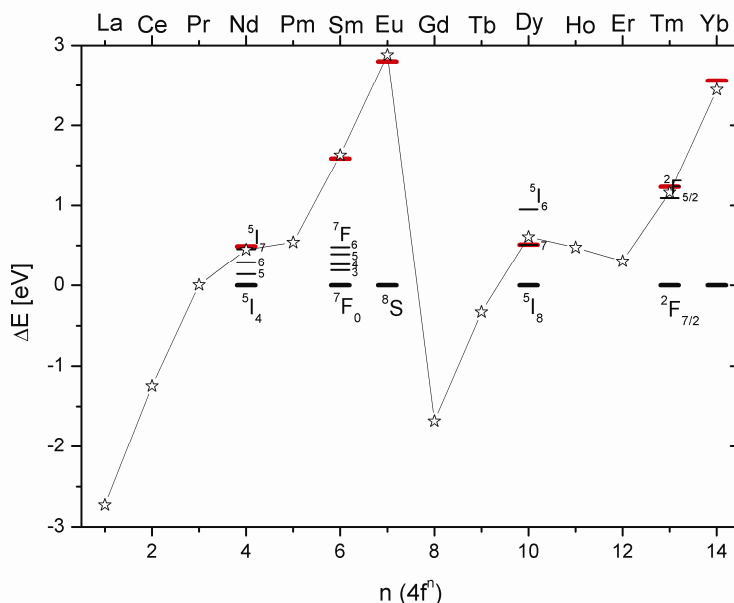
Figure 5.5. Scheme showing the measured $4f^n \rightarrow 4f^{n-1}5d^1$ gap (red bars), measured $4f^n \rightarrow 4f^n$ transitions (thin black lines) and the predicted $4f^n \rightarrow 4f^{n-1}5d^1$ optical gap of LnI_2 relative to the 4f ground state (stars)

The model is empirical and relies on experimental data in order to place the energy transitions relative to each other. This is primarily done using either optical data such as transmission, luminescence excitation or diffuse reflectance spectra, or photoelectron spectroscopy (UPS, XPS or BIS). As long as sufficient data are available for one compound in a series such as EuO for the LnO series, or data for several compounds, such as La_2S_3, Ce_2S_3 and Sm_2S_3 for Ln_2S_3, a scheme may be easily constructed. When such data are unavailable or are incomplete, then the substitution of data on a similar Ln doped compound, i.e. SrI_2:Eu for EuI_2, may be used instead. Using this model it is also possible to plot the energy of the $4f^n \rightarrow 4f^{n-1}5d$ transition and define the 4f ground state to be at 0 energy for each of the compounds studied, so that the

$4f^n \rightarrow 4f^{n-1}5d^1$ bandgap energy varies as the series progresses from La to Ce to Yb as dictated by the zigzag pattern. This is done in figure 5.5 for LnI_2, where the measured $4f^n \rightarrow 4f^{n-1}5d^1$ bandgaps of NdI_2, SmI_2, EuI_2, DyI_2, TmI_2 and YbI_2 have been graphed alongside the predicted $4f^n \rightarrow 4f^{n-1}5d^1$ bandgaps.

The thick black horizontal bars indicate the 4f ground state of the Ln^{2+} ions of the measured Ln diiodides while the red lines indicate the transition to the lowest energy 5d state which is defined using the absorption edge. For NdI_2, DyI_2 and TmI_2, diffuse reflectance spectra were used to determine the optical bandgap, while for SmI_2, EuI_2 and YbI_2, the excitation spectra were used. For SmI_2, where the optical bandgap was visible in both the diffuse reflectance and the excitation spectra, the excitation spectrum was used. This was because the absorption edge observed for SmI_2 measured using diffuse reflectance was particularly difficult to determine and the 0.8eV bandgap energy measured using this seemed too low when considered in relation to the other compounds studied, in particular TmI_2 which should have a smaller $4f^n \rightarrow 4f^{n-1}5d^1$ optical bandgap than SmI_2 [20]. Also in figure 5.5 we show the Ln^{2+} intraconfigurational $4f^n \rightarrow 4f^n$ transition energies identified in the diffuse reflectance spectra shown in figure 5.2. It can be seen that the $4f^n \rightarrow 4f^{n-1}5d^1$ optical bandgaps measured by diffuse reflectance and luminescence excitation spectra correspond well with the data predicted using the empirical model, which was fitted using all the measured data. The predicted values for the $4f^n \rightarrow 4f^{n-1}5d^1$ optical bandgaps are all within 0.11eV of the measured data. The double zigzag curve is 0.2eV lower than the one predicted in our earlier paper, which was predicted using data on SrI_2:Eu^{2+} only [10]. The slight change in the position of the curve makes very little difference to the predictions of metallic or semiconducting behaviour outlined in our previous paper. The known metallic LaI_2, CeI_2 and GdI_2 have negative $4f^n \rightarrow 4f^{n-1}5d^1$ bandgaps, as does the unknown compound TbI_2, showing that the 4f band is situated above the 5d conduction band, leading to a trivalent Ln ion and free electrons in the 5d conduction band, leading to metallic behaviour. With the exception of PrI_2, the

other compounds, including the unknown PmI_2, HoI_2 and ErI_2 are shown to be semiconducting.

PrI_2 is predicted to have a $4f^n \rightarrow 4f^{n-1}5d^1$ optical bandgap of almost 0. This suggests that PrI_2 could display interconfigurational valence behaviour, something that was also suggested by Gerlitzki *et al*. [4]. This very small gap could also explain the different properties of the various PrI_2 polymorphs, as the small changes in the crystalline environment may be enough to alter the crystal field splitting of the Pr 5d band just enough for the compound to exhibit either semiconducting or metallic properties.

5.5. Conclusions

The divalent lanthanide iodides, NdI_2, SmI_2, EuI_2, DyI_2, TmI_2 and YbI_2 show systematic variation in their optical bandgaps as has been predicted using an empirical model. Diffuse reflectance and photoluminescence spectra show both intraconfigurational $4f^n \rightarrow 4f^{n-1}5d^1$ and interconfigurational $4f^n \rightarrow 4f^n$ transitions. The data collected allowed us to study the electronic structure of the LnI_2 system in more detail and could explain some of the physical properties of other compounds in the series. It may in future be of interest to investigate some of these materials further, as their luminescent properties could be utilized, although the hygroscopic nature of the samples may be problematic.

References

[1]   Meyer G, Gerlitzki N and Hammerich S 2004 *Journal of Alloys and Compounds* **380** 71-8

[2]   Burrow J H, Maule C H, Strange P, Tothill J N and Wilson J A 1987 *Journal of Physics C: Solid State Physics* **20** 4115-33

[3]   Stöwe K, Tratzky S, Beck H P, Jungmann A, Claessen R, Zimmermann R, Meng G, Steiner P and Hüfner S 1997 *Journal of Alloys and Compounds* **246** 101-10

[4]   Gerlitzki N, Meyer G, Mudring A-V and Corbett J D 2004 *Journal of Alloys and Compounds* **380** 211-8

[5]   Cherepy N J, Payne S A, Stephen J. Asztalos, Hull G, Kuntz J D, Niedermayr T, Pimputkar S, Roberts J J, Sanner R D, Tillotson T M, van Loef E, Wilson C M, Shah K S, Roy U N, Hawrami R, Burger A, Boatner L A, Choong W-S and Moses W W 2009 *IEEE Transactions on Nuclear Science* **56** 873-80

[6]   Cherepy N J, Hull G, Drobshoff A D, Payne S A, van Loef E, Wilson C M, Shah K S, Roy U N, Burger A, Boatner L A, Choong W-S and Moses W W 2008 *Applied Physics Letters* **92** 083508

[7]   Alekhin M S, de Haas J T M, Krämer K W and Dorenbos P 2011 *IEEE Transactions on Nuclear Science* **58** 2519-27

[8]   Beck H P and Schuster M 1992 *Journal of Solid State Chemistry* **100** 301-6

[9]   Friedt J M, MacCordick J, Sanchez J P and Rebizant J 1980 *Solid State Communications* **35** 1021-4

[10]   Rogers E, Dorenbos P and van der Kolk E 2011 *New Journal of Physics* **13** 093038

[11]   Dorenbos P 2004 *Journal of Luminescence* **108** 301-5

[12]   Dorenbos P, Krumpel A H, van der Kolk E, Boutinard P, Bettinelli M and Cavalli E 2010 *Optical Materials* **32** 1681-5

[13]   Dai S, Young J P and Mamantov G 1991 *Applied Spectroscopy* **45** 1056-8

[14]   Bos A J J, van Duijvenvoorde R M, van der Kolk E, Drozdowski W and Dorenbos P 2011 *Journal of Luminescence* **131** 1465-71

[15]   Dorenbos P, Bos A J J and Poolton N R J 2010 *Physical Review B* **82** 195127

[16]   Wood D L and Kaiser W 1962 *Physical Review* **126** 2079-88

[17]   Kiss Z J 1965 *Physical Review* **137** 1749-61

[18]   Kiss Z J 1962 *Physical Review* **127** 718-24

[19]   van der Kolk E and Dorenbos P 2006 *Chemistry of Materials* **18** 3458-62

[20]   Dorenbos P 2003 *Journal of Physics: Condensed Matter* **15** 575-94

Chapter 6: The effect of increasing nitrogen content on the 4f-5d bandgap energy of $EuO_{1-x}N_x$

Abstract

$EuO_{1-x}N_x$ powders (x=0, 0.1, 0.2, 0.3, 0.4 and 1) were prepared by the solid state reaction of EuO and EuN powders at 1200°C in an Ar atmosphere. The powders show a decrease in both lattice parameter and bandgap with the increase in N content due to an increase in the crystal field splitting and centroid shift of the 5d conduction band levels.

6.1. Introduction

Lanthanide based switchable materials which undergo a reversible semiconductor to metal phase transition under pressure have been of interest for a long time. Of these compounds, Samarium monosulfide, SmS, is undoubtedly the most famous as it exhibits a discontinuous isostructural phase transition at only 0.65 GPa [1]. Other related compounds such as TmTe, SmSe, SmTe and EuO require increasingly high pressures in order to switch and switch continuously [1-3].

The properties of lanthanide based switchable materials strongly depends on the relative position of the localized 4f levels to the 5d conduction band, with materials where the 4f levels lie very close to the conduction band, such as SmS, switching at lower pressures than those with larger 4f to 5d gaps such as EuO.

As the crystal field splitting of the 5d conduction band levels is sensitive to changes in the lattice cell dimensions of the material, it is possible to increase the crystal field splitting, and thus reduce the energy difference between the bottom of the 5d band and the top of the 4f levels by alloying with a related compound. This has been widely investigated for the samarium

monochalcogenides, particularly SmS, where doping with other lanthanides such as La or Gd, or alloying with the samarium monopnictides SmX_p (X_p= P, As, Sb) leads to solid solutions with improved switching and even metallic behaviour [4]. Chevalier *et al.* studied EuO alloyed with NdN, GdN and EuN and observed a change in the structural, electrical and magnetic properties as a function of the substitution concentration and type [5]. Pressure dependent measurements on two samples, $EuO_{0.75}N_{0.25}$ and $Eu_{0.82}Nd_{0.18}O_{0.82}N_{0.18}$ showed switching behaviour at a far lower pressure than that seen for undoped EuO [6]. Recently there has been renewed interest in the magnetic properties of EuO and other rare earth based materials for spintronics applications [7]. EuO is a ferromagnetic semiconductor with a Curie temperature (T_C) of 69K. Upon substitution with Gd, La or Lu the Curie temperature can be increased significantly, in some cases reaching almost 200K [8-11]. Chevalier *et al.* showed that the Curie temperature can also be increased by alloying EuO with EuN, with the Curie temperature reaching 77K when x=0.3 [5]. However, more recently Wicks *et al.* suggested that there was little change in T_C as x increased for $EuO_{1-x}N_x$ thin films deposited by NO-assisted molecular beam epitaxy [12].

By alloying EuO with EuN we should see a shift in bandgap and lattice parameter as the N content increases. The latter has been recorded by Chevalier et al. for $EuO_{1-x}N_x$ where x<0.3 and x>0.92 [5]. Between 0.3 and 0.92 there was a miscibility gap which Gibb et al. attributed to the presence of Eu^{3+} [13] while for x>0.92 a metallic compound containing Eu^{3+} ions was observed.

As EuO has a larger $4f^n \rightarrow 4f^{n-1}5d^1$ energy difference than SmS, it is an interesting material to study optically in order to see how alloying with a similar compound affects the optical bandgap of a lanthanide based compound. Lanthanide based compounds often show interesting optical behaviours and are used as scintillators and phosphors for light emitting diodes (LEDs) among other things. Knowledge on how the $4f^n \rightarrow 4f^{n-1}5d^1$ energy changes with substitution will allow us to make more informed decisions on new functional lanthanide based materials.

EuO is a semiconductor with a face centred cubic NaCl type structure. It contains divalent Eu ions and has a lattice parameter of 5.142Å [14-18]. EuN exhibits the same structure, but contains Eu^{3+} ions. EuN has a considerably smaller lattice parameter of 5.014Å [19] as, although N^{3-} is larger than O^{2-}, this is more than compensated for by the far smaller ionic radius of Eu^{3+} compared to Eu^{2+}. The presence of Eu^{2+} or Eu^{3+} strongly affects the optical properties of the materials. The $4f^7$ ground state is approximately 1eV below the 5d derived conduction band bottom of EuO which means that the optical bandgap of this compound is determined by a 4f to 5d transition. EuN is predicted to exhibit a charge transfer (CT) transition from the top of the N 2p valence band to the 4f shell of Eu^{3+} around 1.3eV [20]. It may also be possible to observe a 2p VB to 5d CT transition for these materials. However as the O 2p to Eu 5d energy difference in EuO is known in literature to be about 5eV, well out of the range measurable by our equipment it is not of concern in this article. EuN is predicted to have an N 2p to Eu 5d energy difference of only 1.5eV on the basis of the bandgaps of the similar compounds DyN, HoN and ErN [21]. It should therefore be possible to observe an additional transition around this energy in our spectra of the mixed anion compounds although the Eu^{2+} 4f-5d and Eu^{3+} N 2p→4f charge transfer transitions may obscure it.

In this article we describe the synthesis of $EuO_{1-x}N_x$ powders and their characterization using X-ray diffraction (XRD). Next we will show the diffuse reflectance spectra of the compounds, before finally discussing their optical properties and electronic structure.

6.2. Experimental Methods

EuO was fabricated by the reaction of Eu_2O_3 powder (99.99%, Rhône Poulenc) and Eu metal pieces (99.9%, Csre) for 8 hours at 800°C in an Ar/H_2 atmosphere while EuN was made by heating Eu metal pieces for 8 hours at 800°C in an N_2 atmosphere. $EuO_{1-x}N_x$ powders were synthesized by the solid

state reaction of EuO and EuN powders in an Ar atmosphere at 1200°C for 8 hours. The resulting compounds were crushed and phase purity was checked by XRD. If necessary, the heating process was repeated in order to obtain better phase purity. Four $EuO_{1-x}N_x$ solid solutions were successfully made with nominal values of x = 0.1, 0.2, 0.3 and 0.4.

Initially thermograviometric analysis (TGA) was used to try to calculate x more accurately. It was proposed that when a $EuO_{1-x}N_x$ sample was heated, two reactions would occur. Firstly, EuO would fully oxidize to Eu_2O_3 and secondly EuN would also oxidize to form Eu_2O_3. The change in mass when this occurred would allow us to calculate x. However samples containing nitrogen, EuN and $EuO_{0.7}N_{0.3}$, displayed strong nitrogen retention which led to a too large mass increase. While the changes in mass for all our measurements were within 1 or 2% of what was expected for these compounds, this difference is of the same order as the difference in the predicted change in mass across all values of x. This meant that we were unable to use TGA as an accurate method for determining x.

XRD measurements were taken for powdered samples using a Bruker D4 X-ray diffractometer between 20 and 120° using Cu kα radiation. As the samples were hygroscopic, Kapton foil was used to protect the samples during measurement. The pattern measured for $EuO_{0.9}N_{0.1}$ was measured some time after the other patterns. In order to allow for peak shifts due to changes in the calibration of the system, the pattern has been corrected using the shift in the corundum patterns used to check the calibration of the system in order to allow for optimal comparisons of the patterns.

Diffuse reflectance was measured between 0.1 and 2.4eV using a modified Pike EasiDiff accessory inside a Bruker Vertex 80V spectrometer. Spectra were measured using a tungsten lamp and a Globar mid infrared lamp as light sources and CaF_2 and KBr beamsplitters. Four detectors were used: GaP, Si,

InGaAs and liquid nitrogen cooled MCT. The reference used for the diffuse reflectance measurements was KBr powder which was assumed to have a constant reflectance across the range of wavelengths studied.

As the samples were oxygen and water sensitive it was necessary to protect the powders from air. To do this, the samples were placed in a sample holder covered with a ZnSe or SiO_2 window, previously described in [22]. The sample was loaded into the holder, an O-ring and a window was placed on top and then sealed by screwing down a cap. This was done in a nitrogen filled glovebox. Using this sample holder led to there being a large specular component to the reflectance which turned out to be unfeasible to correct for post-measurement. Dai et al. used a beamstop placed on the window of their sample holder in order to physically block the specular reflectance [23]. In our case it was decided that rather than place the beamstop on the window, it was easier to place the beam stop further along the optical path, on the outside of the Pike Easidiff accessory. This gave us a way to easily block the specular component of the reflectance.

6.3. Results

6.3.1. XRD

The XRD patterns measured for EuO, EuN and $EuO_{1-x}N_x$ are shown in figure 6.1. The measurements show that the diffraction patterns of $EuO_{1-x}N_x$ are similar to that of EuO, with the diffraction peaks shifted towards higher angles as x increases. EuN has peaks shifted considerably to higher angles than EuO and $EuO_{1-x}N_x$ due to its smaller lattice parameter, as although N^{3-} is larger than O^{2-}, the net effect is a decrease in ionic radius, due to Eu^{3+} being smaller than Eu^{2+}. The EuO and $EuO_{1-x}N_x$ patterns show that the compounds are not phase pure. The EuO pattern shows the presence of Eu_2O_3, while the $EuO_{1-x}N_x$ patterns show a EuN phase which increases in strength with x. The $EuO_{1-x}N_x$ powders probably also contain traces of Eu_2O_3 as it is present in the EuO precursor. Chevalier noted that there was a miscibility gap when x became

greater than 0.3. It is probably this that leads to the increasing amount of second phase EuN in the samples
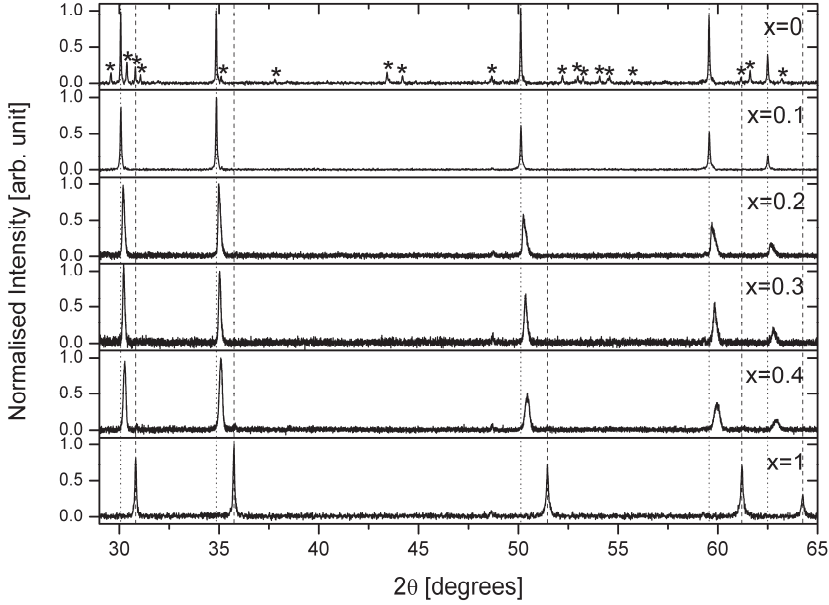
Figure 6.1. X-ray diffraction patterns of $EuO_{1-x}N_x$ for x = 0 (EuO), 0.1, 0.2, 0.3, 0.4 and 1 (EuN). Values of x are nominal and relate to the ratio of EuO to EuN in the initial composition of the samples before firing. The dotted and dashed lines act as a guide to the eye regarding the position of the EuO and EuN peaks respectively, and *s indicate peaks due to Eu_2O_3.

XRD peaks were fitted using the built-in peak fitting functions in Origin pro 8 using a Voigt function and the fitted values for the peak maxima were used to calculate the lattice parameter shown in figure 6.2. The value used was the median value and error bars reflect the range of lattice parameters calculated for each sample. The lattice parameter is given as a function of nominal EuN content. In addition to calculating the lattice parameter, XRD was used to estimate how much of the EuN second phase was present as thermograviometric analysis turned out to be inconclusive for the samples studied. EuN was found in the samples with nominal compositions $EuO_{0.8}N_{0.2}$, and $EuO_{0.6}N_{0.4}$. These data were used to correct the value of x. Causes of errors

in the values of x shown were determined to be largely due to the presence of Eu_2O_3 in the sample and errors in transferring the precursor powders from the weighing paper to the crucible. As relatively low concentrations of Eu_2O_3 were seen in the XRD patterns of $EuO_{1-x}N_x$, it is possible that some of the excess O displaces N. To allow for this, an error is included that indicates x if all the excess O in the sample displaces N. The loss of material due to adhesion to the weighing paper was found to produce an error that increased x. This error is also included in figure 6.2. The lattice parameters for $EuO_{1-x}N_x$ as measured by Chevalier *et al.* are also shown in figure 6.2 as are the lattice parameters for $EuO_{1-x}N_x$ as expected using Vegard's Law using our measurements for the lattice parameters of EuO and EuN of 5.142 and 5.0165Å respectively.
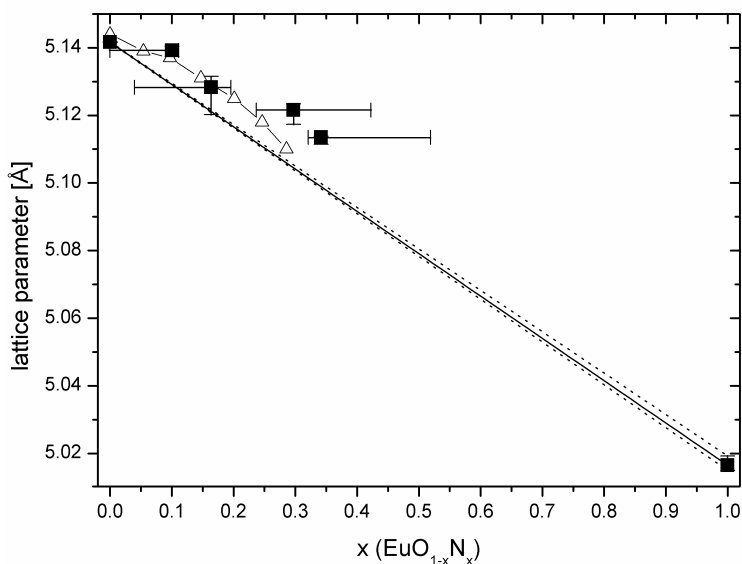
**Figure 6.2.** Lattice parameters for $EuO_{1-x}N_x$: squares = lattice parameter versus nominal EuN content x, triangles = data measured by Chevalier et al. [5]. The solid line shows the change in lattice parameter predicted by Vegard's Law, and the dotted lines indicate the range in the predicted lattice parameter when errors in the values of the lattice parameters of EuO and EuN are considered.

6.3.2. Diffuse reflectance

Figure 6.3 shows the diffuse reflectance spectra of EuO, $EuO_{0.8}N_{0.2}$, $EuO_{0.7}N_{0.3}$, $EuO_{0.6}N_{0.4}$ and EuN measured between 0.2 and 2.4eV.EuO shows a strong reflectance edge around 0.84±0.1eV, which we attribute to a $4f^7 \rightarrow 4f^6 5d^1$ transition, similar to those observed elsewhere [3, 24, 25]. Below 0.75eV a series of sharp dips can be seen. The dips labelled with blue arrows are attributed to Eu^{3+} $4f^7 \rightarrow 4f^7$ transitions, while those marked with red arrows may be an indication that water is present in the sample.
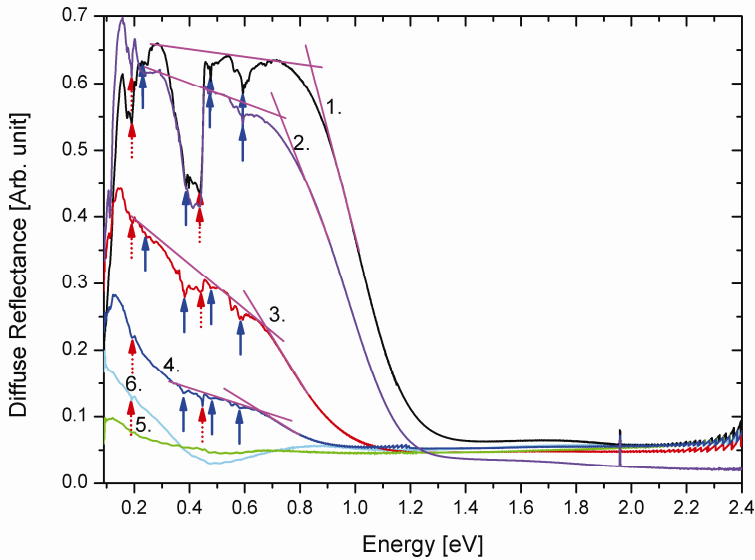
Figure 6.3. The diffuse reflectance of $EuO_{1-x}N_x$ powders: 1. EuO, 2. $EuO_{0.9}N_{0.1}$, 3. $EuO_{0.8}N_{0.2}$, 4. $EuO_{0.7}N_{0.3}$, 5. $EuO_{0.6}N_{0.4}$, 6. EuN, solid blue arrows indicate Eu^{3+} $4f^7 \rightarrow 4f^7$ transitions while dotted red arrows indicate possible water lines. Magenta lines act as a guide to the eye regarding the definition of the reflectance edge.

EuN displays a very different diffuse reflectance spectrum to EuO. EuN is expected to display a charge transfer transition from the N 2p valence band to the Eu3+ 4f shell around 1.27eV. However, the diffuse reflectance spectrum does not show an absorption edge, and the shape of the spectrum suggests that EuN is semimetallic.

$EuO_{0.9}N_{0.1}$ shows a reflectance edge around $0.73\pm0.1eV$ that we attribute to an Eu^{2+} $4f^7{\rightarrow}4f^65d^1$ transition albeit shifted to lower energies than that seen for EuO. The spectrum also exhibits dips attributable to Eu^{3+} $4f^7{\rightarrow}4f^7$ transitions and there may also be some water present.

$EuO_{0.8}N_{0.2}$ shows a reflectance edge around $0.67\pm0.1eV$ that we attribute to an Eu^{2+} $4f^7{\rightarrow}4f^65d^1$ transition, shifted to lower energies. The spectrum also exhibits dips attributable to Eu^{3+} $4f^7{\rightarrow}4f^7$ transitions and there may also be some water present. Below 0.6eV the diffuse reflectance spectrum of $EuO_{0.8}N_{0.2}$ deviates in shape from that observed for EuO. The decrease in intensity between 0.15 and 0.6 eV is most likely due to the presence of EuN in the sample, either in a solid solution with EuO in the form of $EuO_{0.8}N_{0.2}$, or as unabsorbed EuN present in the sample.

$EuO_{0.7}N_{0.3}$ shows a reflectance edge around $0.65\pm0.1eV$ that is attributed to an EuO $4f^7{\rightarrow}4f^65d^1$ transition shifted to lower energy. Eu^{3+} $4f^7{\rightarrow}4f^7$ transitions are also visible, although they appear lower in intensity than those observed for EuO and $EuO_{0.8}N_{0.2}$. This is due to the lower overall intensity of the spectrum. The deviation in behaviour from that of EuO observed for $EuO_{0.8}N_{0.2}$ is stronger for $EuO_{0.7}N_{0.3}$. As this sample contains more EuN, this strongly suggests that this behaviour is due to the presence of EuN.

$EuO_{0.6}N_{0.4}$ appears to be different to both $EuO_{0.8}N_{0.2}$ and $EuO_{0.7}N_{0.3}$. Here the strong absorbance of EuN present in solution and as an impurity phase in the sample dominates the spectrum making it impossible to determine where the $4f^7{\rightarrow}4f^65d^1$ transition has been shifted. Likewise, due to the low overall intensity of the measured spectrum, it is no longer possible to observe Eu^{3+} $4f^7{\rightarrow}4f^7$ transitions and any possible dips due to the presence of water.

6.4. Discussion

6.4.1. Phase formation and lattice parameters

In figure 6.1, the XRD patterns for EuO, EuN and $EuO_{1-x}N_x$ (x=0.2, 0.3 and 0.4) are shown. The samples are not completely phase pure, in the case of EuO there are peaks attributable to Eu_2O_3, while the $EuO_{1-x}N_x$ samples contain unreacted EuN.

The lattice parameters for EuO and EuN calculated from the measured patterns are 5.142 Å and 5.017 Å respectively, which corresponds well with the values from literature. The lattice parameters calculated for measurements on the $EuO_{1-x}N_x$ samples however, deviate from what is expected from Vegard's law and from that which was previous measured by Chevalier *et al*. (figure 6.2). The second phases lead to the nominal value of x being an overestimate, but even taking this into account there is still a strong deviation from what is expected. This may be an indication that the solid solution is not ideal and the distribution of O^{2-} and N^{3-} is not random due to $Eu^{2+}O^{2-}$ and $Eu^{3+}N^{3-}$ forming local pairs due to charge compensation effects.

6.4.2. Diffuse Reflectance

In figure 6.3 the diffuse reflectance spectra of EuO, EuN and $EuO_{1-x}N_x$ (x=0.1, 0.2, 0.3 and 0.4) are shown. EuO is semiconducting, but EuN shows very different optical behaviour, suggesting that it is semimetallic. $EuO_{0.9}N_{0.1}$, $EuO_{0.8}N_{0.2}$ and $EuO_{0.7}N_{0.3}$ also appear to be semiconducting, but the presence of increasing amounts of EuN, which is strongly absorbing, particularly between 0.3 and 0.7eV, strongly influences the shape of the spectrum in the transmitting region. In the case of $EuO_{0.6}N_{0.4}$, this influence is so strong that it is impossible to determine the bandgap of the compound.
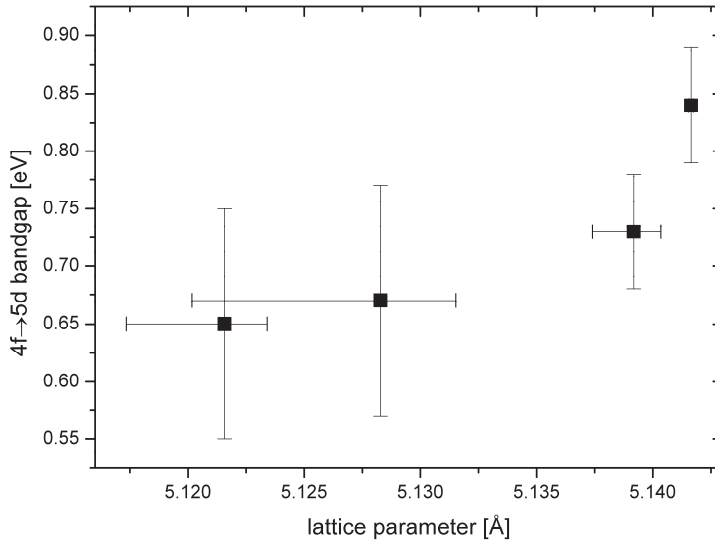
Figure 6.4. Lattice parameter versus bandgap for $EuO_{1-x}N_x$: black squares=measured data

In figure 6.4 we show bandgap energy versus lattice parameter for EuO, $EuO_{0.9}N_{0.1}$, $EuO_{0.8}N_{0.2}$ and $EuO_{0.7}N_{0.3}$. The bandgap is here defined as the energy difference between the Eu^{2+} 4f band and the bottom of the Eu 5d conduction band. There is a decrease in bandgap with decreasing lattice parameter. Extrapolating to smaller lattice parameters gives a suggested bandgap for $EuO_{0.6}N_{0.4}$ of around 0.57eV which is in the region where the EuN absorption is strongest, confirming that this is the reason that no band edge is clearly visible.

The relationship between lattice parameter and bandgap suggests that the changing bandgap effect is structural in nature and that contributions due to excess electrons in the conduction band are insignificant.

The decrease in bandgap measured for $EuO_{0.9}N_{0.1}$, $EuO_{0.8}N_{0.2}$ and $EuO_{0.7}N_{0.3}$ is attributed to a lowering of the Eu 5d conduction band relative to the Eu^{2+} 4f ground state compared to that of EuO. We envisage two causes for the shift in

the 5d band of $EuO_{1-x}N_x$ as x increases. The first is the increased crystal field splitting of the 5d levels, due to the presence of an increasing amount of dopants in the form of smaller Eu^{3+} and larger N^{3-} ions compared to Eu^{2+} and O^{2-} respectively, which lead to shorter Eu to O/N distances and a decreased lattice parameter. Of these, the smaller Eu^{3+} ion has the largest influence, as can be seen by the much smaller lattice parameter of EuN compared to EuO. The second is an increase in the centroid shift, defined as the decrease in average energy of the different 5d levels for lanthanides in compounds relative to that of the free lanthanide ion. Such decrease is due to increased covalency between 5d-orbitals and anion orbitals, and the covalency in the Eu-N bond is larger compared to that in the Eu-O bond. Figure 6.5, where the zero of energy is defined as the binding energy of an electron in the $4f^7$ ground state of Eu^{2+}, shows how the electronic structure of $EuO_{1-x}N_x$ changes with x. The figure uses solid red and blue bars to represent the O-2p (α) and N-2p (β) bands. The $Eu^{2+}4f^7$ ground state is represented by the orange horizontal lines (γ) while the Eu 5d band of EuO is represented by the unfilled pink bars labelled ε. The $Eu^{3+/2+}$ acceptor state of EuN for each compound represented in the figure is labelled δ, while the corresponding EuN Eu 5d band is represented by the unfilled grey bars labelled ζ. The 4f to 5d energy differences for EuO and $EuO_{1-x}N_x$ indicated by arrows b, c, d and e in the figure, are taken from the diffuse reflectance spectra in figure 6.3. The O2p to 4f(2+) energy gap in EuO, indicated by arrow a, was taken from photoemission data from literature [26-28]. The same gap is assumed for the samples with x=0.1, 0.2, and 0.3 in Figure 6.5 as was observed by Wicks et al. in [12]. Data for EuN for the N-2p→5d and N-2p→4f transitions, labelled f and g respectively, are taken from our earlier predictions in [20]. As EuN appears to be semimetallic, this suggests that our previous prediction in chapter 3 and used in figure 6.5 overestimates the EuN bandgap. We would also expect, from looking at figure 6.5, to see transitions from the occupied 4f band to the Eu^{3+} 5d band, something that is not observed in our spectra. While we show lowering of the bottom of the EuO Eu-5d band as x increases, we do not do the same for the EuN 5d-band. By the

same argument used to attribute part of the change in the energy of the 4f→5d transition of EuO to increased crystal field splitting, we would expect for there to be some effect on the energy of the bottom of the Eu-5d band of EuN. However, as we have no quantifiable information on how it would change with x, it is not included in the diagram.
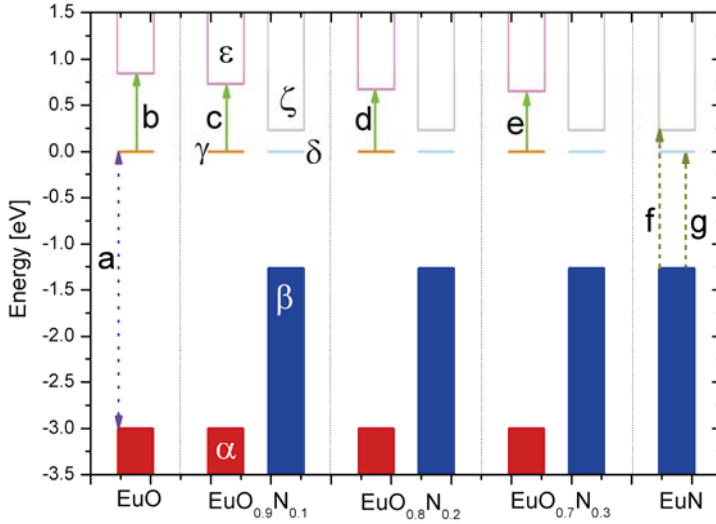
Figure 6.5. Energy level scheme for $EuO_{1-x}N_x$, EuO and EuN (predicted): solid red bar (α) = 02p band, solid blue bar (β) = N 2p band, orange line (γ) = Eu^{2+} 4f ground state, cyan line (δ) = $Eu^{3+/2+}$ acceptor state of EuN, open pink bar (ϵ) = Eu^{2+} 5d conduction band, open grey bar (ζ) = Eu^{3+} 5d conduction band. Green arrows indicate measured transitions, purple arrows indicate literature values and dark yellow arrows indicate transitions estimated in [20]. Arrow a = EuO O-2p→Eu-$4f^7$, arrows b to e = Eu^{2+} $4f^7$→$4f^6 5d^1$, arrow f = EuN N-2p→Eu-5d and arrow g= N-2p to $Eu^{3+/2+}$ acceptor state.

Considering the very different behaviour in the change in lattice parameter of $EuO_{1-x}N_x$ with x compared to that observed for $SmCh_{1-x}Pn_x$, where Ch= S, Se and Pn= P, As, Sb, it is not possible to infer from the results presented in this investigation how the electronic structure of the Sm compounds change with x. Why the change in lattice parameter of $EuO_{1-x}N_x$ compounds deviates from the behaviour seen for the Sm compounds, is unclear. While the discontinuous

phase transition of SmS compounds complicate the comparison between SmS and EuO based compounds, SmSe exhibits a continuous phase transition like EuO, although at lower pressures. However, SmSe shows similar behaviour to SmS in that the decrease in lattice parameter when it is alloyed with a pnictide such as As, is far faster than that predicted by Vegard's law. The increased change in lattice parameter of $SmCh_{1-x}Pn_x$ has been suggested to be due to the switching of Sm^{2+} ions to Sm^{3+} ions.

One major difference between the electronic structures of $SmCh_{1-x}Pn_x$ and $EuO_{1-x}N_x$ is that SmP, SmAs and SmSb have Sm^{3+} $4f^{3+/2+}$ acceptor states above the bottom of the 5d band, whereas in figure 5 we show the $4f^{3+/2+}$ acceptor states of Eu^{3+} for EuN lying below it. Etourneau et al. reported lattice parameters measured for $Eu_{1-x}Nd_xO_{1-x}N_x$ and $Eu_{1-x}Gd_xO_{1-x}N_x$ as well as $EuO_{1-x}N_x$ [29]. Unlike $EuO_{1-x}N_x$ the lattice parameters for $Eu_{1-x}Gd_xO_{1-x}N_x$ and $Eu_{1-x}Nd_xO_{1-x}N_x$ (below x=0.26) appeared to follow Vegard's Law [29]. Above x=0.26 $Eu_{1-x}Nd_xO_{1-x}N_x$ appears to behave more like $SmSe_{1-x}As_x$ [30], which appears to us to suggest that some of the Eu^{2+} ions lost an electron and switched to Eu^{3+}. The main difference in the electronic structure between $EuO_{1-x}N_x$ and $Eu_{1-x}Nd_xO_{1-x}N_x$ and $Eu_{1-x}Gd_xO_{1-x}N_x$ and the $SmCh_{1-x}Pn_x$ compounds is the presence of the $Ln^{3/2+}$ acceptor state below the 5d band and it seems likely that this a major cause in the deviation in the change in lattice parameter for $EuO_{1-x}N_x$ compared to the other related compounds.

6.5. Conclusions

$EuO_{1-x}N_x$ (x<0.4) were prepared by the direct reaction of EuO and EuN at 1200°C. The samples show a decrease in both bandgap and lattice parameter as EuN content increases. The presence of increasing quantities of EuN strongly affects the diffuse reflectance spectra of these samples. We attributed the decrease in the optical $4f^7 \rightarrow 4f^65d^1$ bandgap to an increase in the crystal field splitting of the 5d band levels. This is caused by an increase in lattice pressure. The lattice pressure is increased by the substitution of EuN for EuO, as EuN

has a smaller ionic radius. A further shift in the $4f^7 \rightarrow 4f^6 5d^1$ bandgap is caused by a centroid shift due to the more highly covalent Eu-N bond compared to Eu-O.

References

[1] Jayaraman A, Narayanamurti V, Bucher E and Maines R G 1970 *Physical Review Letters* **25** 1430-3

[2] Jayaraman A 1972 Influence of Pressure on Phase Transitions. pp 121-42

[3] Zimmer H G, Takemura K, Syassen K and Fischer K 1984 *Physical Review B* **29** 2350-2

[4] Jayaraman A. and Maines R G 1979 *Physical Review B* **19** 4154-61

[5] Chevalier B, Etourneau J, Tanguy B, Portier J and Hagenmuller P 1973 *C. R. Acad. Sc. Paris C* **277** 1029-31

[6] Chevalier B, Demazeau G, Etourneau J and Hagenmuller P 1979 *Physica Status Solidi B.* **93** K63-K6

[7] Schmehl A, Vaithyanathan V, Herrnberger A, Thiel S, Richter C, Liberati M, Heeg T, Röckerath M, Kourkoutis L F, Mühlbauer S, Böni P, Muller D A, Barash Y, Schubert J, Idzerda Y, Mannhart J and Schlom D G 2007 *Nature Materials* **6** 882-7

[8] Mayazaki H, Im H J, Terashima K, Yagi S, Kato M, Soda K, Ito T and Kimura S 2010 *Applied Physics Letters* **96** 232503

[9] Melville A, Mairoser T, Schmehl A, Shai D E, Monkman E J, Harter J W, Heeg T, Hollander B, Schubert J, Shen K M, Mannhart J and Schlom D G 2012 *Applied Physics Letters* **100** 4

[10] Ott H, Heise S J, Sutarto R, Hu Z, Chang C F, Hsieh H H, Lin H J, Chen C T and Tjeng L H 2006 *Physical Review B* **73** 094407

[11] Mairoser T, Schmehl A, Melville A, Heeg T, Canella L, Böni P, Zander W, Schubert J, Shai D E, Monkman E J, Shen K M, Schlom D G and Mannhart J 2010 *Physical Review Letters* **105** 257206

[12]   Wicks R, Altendorf S G, Caspers C, Kierspel H, Sutarto R, Tjeng L H and Damascelli A 2012 *Applied Physics Letters* **100** 4

[13]   Gibb T C, Greenwood N N, Viegas F, Chevalier B and Etourneau J 1977 *Journal of Solid State Chemistry* **22** 239-41

[14]   Rau R C 1964 In: *Proceedings of the Rare Earth Research Conference,* p 117

[15]   Taylor D 1984 *Transactions and Journal of the British Ceramic Society* **83** 5-9

[16]   McWhan D B, Souers P C and Jura G 1966 *Physical Review* **143** 385-9

[17]   Eick H A, Baenziger N C and Eyring L 1956 *Journal of the American Chemical Society* **78** 5147-9

[18]   Cunningham G W 1963 *Reactor Materials* **6** 63-6

[19]   Klemm W and Winkelmann G 1956 *Zeitschrift fuer Anorganische und Allgemeine Chemie* **288** 87-90

[20]   Rogers E, Dorenbos P and van der Kolk E 2011 *New Journal of Physics* **13** 093038

[21]   Sclar N 1964 *Journal of Applied Physics* **35** 1534-8

[22]   Rogers E, Dorenbos P, de Haas J T M and van der Kolk E 2012 *Journal of Physics: Condensed Matter* **24** 275502

[23]   Dai S, Young J P and Mamantov G 1991 *Applied Spectroscopy* **45** 1056-8

[24]   Busch G, Junod P and Wachter P 1964 *Physics Letters* **12** 11-2

[25]   Wachter P 1972 *Critical Reviews in Solid State and Materials Sciences* **3** 189

[26]   Beukers J N, Kleibeuker J E, Koster G, Blank D H A, Rijnders G, Hilgenkamp H and Brinkman A 2010 *Thin Solid Films* **518** 5173-6

[27]   Eastman D E, Holtzberg F and Methfessel S 1969 *Physical Review Letters* **23** 226-9

[28]   Steeneken P G 2002 New light on EuO thin films. In: *PhD Thesis*: Rijksuniversiteit Groningen)

[29] Etourneau J, Chevalier B, Hagenmuller P and Georges R 1980 *Journal de Physique, Colloque* **41** C5-193-C5-204

[30] Cater E D, Heslinga D D, Schweitzer J W and Beeken R B 1981 *Journal of Applied Physics* **52** 2143-5

Chapter 7: Thermally induced metal-semiconducting phase transition of Samarium Monosulphide (SmS) thin films

Abstract

High quality phase pure Samarium Monosulphide (SmS) thin films were prepared by electron beam evaporation using a samarium metal source in a H_2S atmosphere. The optical properties (reflection, transmission, absorption) of the films in the semiconducting and metallic phase were analysed from the UV to the mid-IR and explained in terms of the electronic structure of SmS. In this paper it will be shown that metallic SmS thin films exhibit an apparently continuous thermally induced metallic to semiconducting phase transition when studied optically. Temperature dependent XRD measurements however indicate that the metallic to semiconductor phase transition is in fact first order at a single grain level. The apparently continuous optical behaviour is therefore due to the polycrystalline nature of the films.

7.1. Introduction

The reversible semiconductor to metallic phase transition of Samarium Monosulphide (SmS) has been observed many times [1-9]. The discontinuous pressure induced transition from a semiconducting to a metallic phase occurs under a relatively low 6.5kbar of hydrostatic pressure. This transition is then reversible upon the reduction of pressure to below 1 to 1.5kbar [1,2]. Under ambient conditions SmS is a black (green in some thin films) semiconductor

with a NaCl (rock salt) structure [10] with divalent Sm ions. In the semiconducting phase SmS has a 3p valence band and a 5d conduction band which is divided by the crystal field interaction into lower energy t_{2g} and higher energy e_g states. The $4f^6$ ground state levels of Sm^{2+} lie just below the conduction band [4, 11, 12]. Van der Kolk and Dorenbos have shown [12] that the energy difference between the 3p valence band and 5d conduction band is constant throughout the lanthanide series (LaS, CeS, PrS, ..SmS,.., LuS) but that the $4f^n$ energy levels of the lanthanide ions with respect to the conduction band change dramatically as a function of the type of lanthanide ion. From LaS to PmS and GdS to ErS the 4f ground state lies above the conduction band, leading to metallic behaviour, while in the case of EuS and YbS the 4f ground state lies well below the conduction band, resulting in semiconductor like behaviour. In the exceptional case where the $4f^n$ levels lie in very close proximity to the 5d conduction band, as is seen for SmS, the material becomes resonant and can switch between the metallic and semiconducting phase after a critical perturbation [12].

Switching occurs when applied pressure increases the crystal field splitting between the t_{2g} and e_g levels until the bottom of the 5d band overlaps with the ground state 4f levels so that each Sm^{2+} ion donates one electron to the conduction band and becomes Sm^{3+} [11, 13]. The result is that the material undergoes a discontinuous isostructural transition to a golden, metallic phase with trivalent Sm. When the pressure is released from a sample under hydrostatic pressure, a hysteretic discontinuous return to the semiconducting phase is observed [1, 2]. Pressure induced switching from a semiconducting to a metallic state has also been observed in SmS thin films. In this case the switching mechanism has been ascribed to stresses induced by polishing equivalent to the effect of applying hydrostatic pressure [14]. In this case there is no return to the semiconducting phase upon the cessation of polishing.

Besides the pressure induced reverse metal to semiconductor phase transition, it has been shown in several studies that a metal to semiconductor phase transition, suggested to be due to the relaxation of stresses, can be induced by heating either a crystal with a metallic surface layer or a metallic thin film [4, 6-8]. The metallic layer could be induced by polishing or during film synthesis. The thermally induced transition was first observed by Kaldis and Wachter in 1972 for a metallic layer on a SmS crystal [4]. This result was confirmed by Pohl *et al.* in 1974 for a bulk crystal heated on a hotplate in air [6] while Bzhalava *et al.* observed the thermally induced transition for a metallic phase thin film [7, 8]. However, due to the lack of quantitative experimental data, no conclusions on the time and temperature dependence of the phase transition, or on a possible mechanism behind it, could be made.

In this paper the thermally induced metallic to semiconducting phase transition has been studied both optically and by using temperature dependent x-ray diffraction (XRD) in order to understand how the optical properties, electronic structure, lattice constant and crystal structure change during the transition.

Many different methods of preparing SmS thin films have been investigated [9, 15, 16], however in this investigation polycrystalline SmS thin films were synthesized using electron beam evaporation as is described in the experimental section. In the results section the transmission/absorption and reflectance and the XRD characterization of these films in the semiconducting and metallic phases is initially presented. The thermally induced metallic to semiconducting phase transition measured using temperature dependent Fourier Transform absorption and reflection spectroscopy and XRD is then given. It will be shown that although the optical spectra suggest a continuous transition, the XRD results indicate a discontinuous transition on a grain by grain basis.

7.2. Experimental

Polycrystalline semiconducting phase SmS thin films of thickness varying between 50 and 800nm were prepared using electron beam evaporation. Prior to thin film deposition, the vacuum chamber (Leybold Univex 450) was pumped down to a pressure below 10^{-4} Pa. Samarium metal ions were evaporated from a Sm metal source (Sm 99.9% Alfa Aesar) using an electron beam. These reacted with the Hydrogen Sulphide (H_2S) atmosphere of the chamber and the resulting SmS condensed on substrates heated between 250 and 275°C. The best results were obtained with a H_2S pressure of 1 x 10^{-3} Pa for a deposition rate of 1.2nm/s, as measured using a quartz microbalance.

Our XRD measurements showed that the films are of high quality, with no evidence of impurity phases such as SmO or other samarium sulphide phases such as Sm_2S_3. The films appeared highly stable with measurements taken three or four months after film synthesis still showing identical absorbance and XRD results with no sign of impurities despite the films being stored in air. SEM analysis using a Phillips/FEI X130-SFEG microscope showed polycrystalline films with crystallites of around 30nm. The metallic phase was obtained by polishing the films with 0.3µm alumina powder until a golden layer appeared on the upper surface of the film.

The films were initially characterized with x-ray diffraction (Bruker D8, Cu Kα radiation). Samples were then further characterized by Fourier Transform UV to MIR spectroscopy (Bruker Vertex 80V spectrometer) in order to measure the absorbance, transmittance and reflectance of the films. By varying the combinations of sources (deuterium lamp, tungsten lamp and globar), detectors (GaP, Si and Deuterated Triglycine Sulphate) and beam splitters (CaF_2 and KBr) used, it was possible to measure the transmission and reflectance between 400 and 40000cm^{-1} (0.12 to 5eV), while the absorbance (A) was calculated from the transmittance (T) using the Lambert Beer equation $A = -\log_{10}(T)$.

Temperature dependent optical measurements were conducted with a Janis VPF-800 cryostat controlled by a Lakeshore Model 331 Temperature Controller integrated into the Bruker Vertex 80V spectrometer. Temperature dependent X-ray diffraction measurements were carried out in a PANalytical X'Pert Pro MPD X-ray diffractometer with an Anton Paar TTK 450 chamber.

7.3. Results

7.3.1. XRD and Optical Film Characterisation

Figure 7.1 curve a shows the XRD spectrum of an as deposited 400nm thick SmS film on glass (Corning 1737F). The XRD peaks matched well with those in literature, with peaks corresponding to the (111), (200), (220), (311), and (222) lattice planes [5, 17, 18]. Curve b shows the same film after being polished into the metallic phase. It can clearly be seen that some semiconducting phase SmS still remains. XRD measurements on polished films of different thicknesses suggests that only a surface layer of the film is switched, as the ratio of metallic to semiconducting SmS decreases with thickness independently of the level of polishing. The metallic state is isostructural with the semiconducting one, with peaks corresponding to the same set of reflection planes. The metallic phase peaks appear at slightly higher angles to those of the semiconducting phase due to the lattice contraction related to the switch to trivalent Sm ions that have a smaller ionic radius than divalent Sm. Our measured value of 593pm for the lattice constant of the semiconducting phase at 300K is somewhat smaller than the 597pm measured elsewhere [8, 16, 19]. However the lattice constant of 570pm calculated for the metallic phase is consistent with that measured by other investigations [8, 20]. The SEM image of a semiconducting phase film inset into figure 1 shows that the film is polycrystalline with grain sizes of about 30nm.
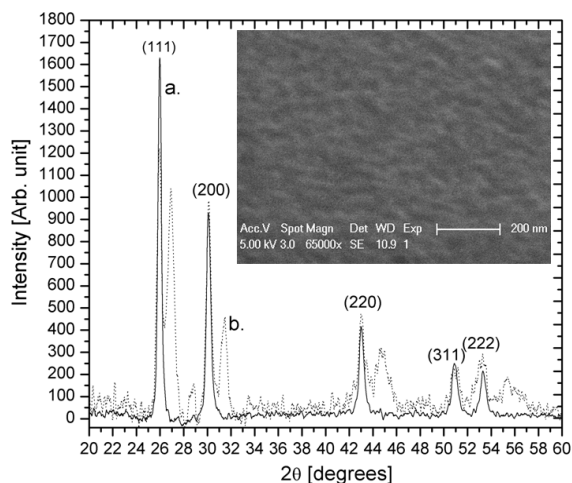
Figure 7.1. XRD measurements of a SmS thin film deposited on glass: a) Semiconducting phase, b) with a thin metallic phase surface layer, inset: SEM image of the surface of a semiconducting phase SmS thin film.

Next the films were characterized using FT spectroscopy. Figure 7.2 shows the normalized transmittance (figure 7.2A), absorbance (figure 7.2B) and reflectance (figure 7.2C) of the semiconducting phase (curves 1) of a 400nm thick SmS thin film deposited on quartz and the same sample after a surface layer has been polished into the metallic phase (curves 2).

There is a considerable difference between the transmittance, absorbance and reflectance of the semiconducting and metallic phase. The transmittance and absorbance spectra of the semiconducting phase show 4f-5d transitions as will be explained in the following section, however, the same features in the corresponding reflectance spectrum are masked by thin film interference fringes between 12000 and 32000 cm^{-1}. The features in the transmittance and absorbance spectra are independent of thickness and are therefore due to 4f-5d transitions rather than interference effects. The major feature in the metallic phase is the transition between 20000 and 25000cm^{-1} which appears very strongly for reflectance measurements, where it gives the metallic phase film its characteristic gold colouring, and is also present in the transmission and

absorption spectra. The gold colour of SmS is attributed by Kirk *et al.* to the 3p-5d transition. This bound electron transition also appears in the reflectivity spectra of noble metals and is responsible for the typical colour of gold [2].
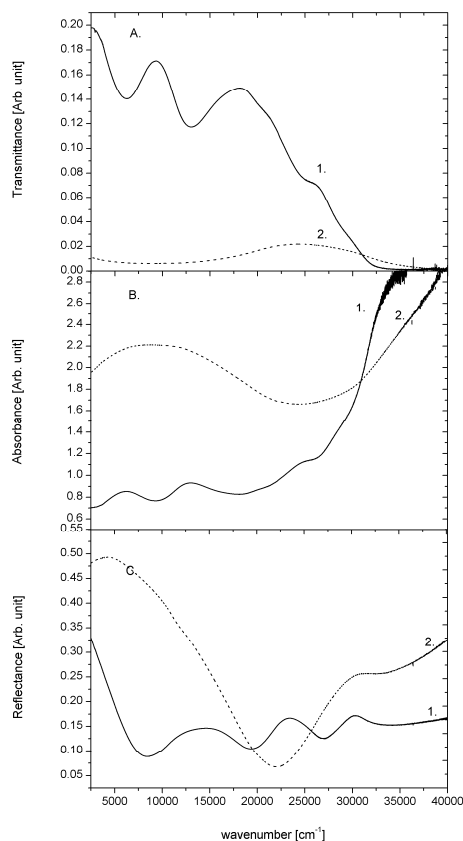

Figure 7.2. The normalized transmittance (A), absorbance (B) and reflectance (C) of a 400nm thick SmS thin film on quartz: 1) in the semiconducting phase, 2) after being polished into the metallic phase.

7.3.2. Temperature dependent absorption of Semiconducting SmS thin films

Figure 7.3 shows the normalized absorption spectrum of semiconducting SmS as a function of temperature for 475nm thick thin films on a Corning 1737F glass substrate. According to the data of Holtzberg *et al.*, Batlogg *et al.* and Suryanarayanan *et al.* the position of the absorption peaks due to 4f-5d transitions have been assigned so that the E_1 peak at 6650cm^{-1} (0.8eV) is due to the $4f^6(^7F_0) - 4f^5(^6H)5d(t_{2g})$ transitions, the E_2 peak at 13215cm^{-1} (1.6eV) is

due to $4f^6(^7F_0)$ to $4f^5(^6F)5d(t_{2g})$ transitions and the E_3 peak at 25000cm^{-1} (3.1eV) has been attributed to the $4f^6(^7F_0)$ to $4f^5(^6H)5d(e_g)$ transitions [21, 11, 16]. It can be noted however that the resulting 2.3eV crystal field splitting thus obtained for t_{2g} and e_g is much larger than that observed for divalent lanthanide levels in compounds with an octahedral coordination [22]. The positions of the 4f-5d transitions have been published several times, although there have been considerable shifts in the recorded positions of the peaks [4, 10, 11, 16, 21, 23]. The lower edge of the 3p-5d transitions can also be identified and is assigned to the increase in the slope of the absorbance towards higher energy starting at approximately 18000cm^{-1} (2.2eV).
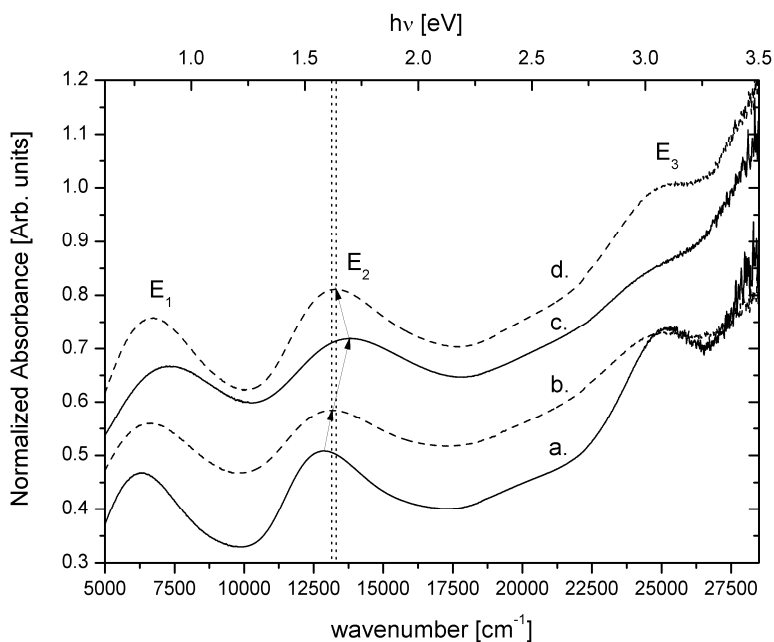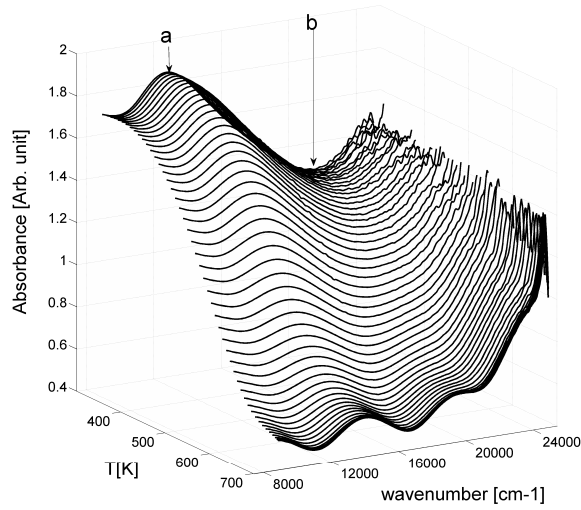

Figure 7.3. The temperature dependence of the absorption of semiconducting SmS: a) 77K, b) 300K, c) 700K, d) 300K (cooled from 700K). The E_1, E_2 and E_3 peaks are indicated. Arrows act as a guide to the peak shift while the dotted vertical lines act as a guide to the hysteresis.

The 4f-5d transitions of semiconducting SmS thin films show a considerable temperature dependence. At 77K (curve a) the absorption peaks are narrower and the E_1 and E_2 peaks are shifted to the lower energies of 6326 cm^{-1} and 12876 cm^{-1} while the E_3 peak is shifted to a higher energy (25250cm^{-1}) than the corresponding peak energy of the film at 300K (curve b). At 700K (curve c) the peaks are broader and the E_1 and E_2 peaks are shifted to higher energies, appearing at 7329 and 13794 cm^{-1} respectively. Assuming the previous peak assignations, this suggests a decrease in the crystal field splitting, caused by a thermally induced increase in lattice constant. The opposite effect accounts for the behaviour of the film cooled to 77K (curve a). However, while the peak positions of the cooled films return to the original values upon returning to 300K, the heated film shows a small hysteresis in the position of the peaks as is seen in curve d. Although the shift decreases as the film is cooled, the energies of the first two 4f-5d peaks do not return to their initial values but remain shifted by about 0.02eV. It is possible that stresses in the as deposited films that increase crystal field splitting are partially removed after annealing.

7.3.3. The Thermally Induced Phase Transition of SmS

Figure 7.4 shows the temperature resolved absorbance of a 400nm thick SmS thin film with a surface layer polished into the metallic phase, as it is heated from 300 to 700K. A temperature ramp of 20K/min was programmed (in addition at the end of the ramp the sample was held at the maximum temperature for 450 seconds). Figure 7.4 shows that the metallic layer on the semiconductor film gradually disappears. Initially the spectrum is identical to the absorbance of the metallic phase shown in figure 2B. At about 400K a decrease in the absorbance is clearly visible, the broad peak at 12750 cm^{-1} (arrow a) and the minimum at 21-22000 cm^{-1} (arrow b) shift and new features, attributable to the E_2 4f-5d (14100 cm^{-1}) and 3p-5d (~18000 cm^{-1}) transitions of the semiconducting phase appear before measurements stop at 700K.

Figure 7.4. Temperature dependent switching of polished SmS: absorption spectrum between 300 and 700K. Arrow a indicates the absorbance maximum and arrow b the minimum for the metallic phase.
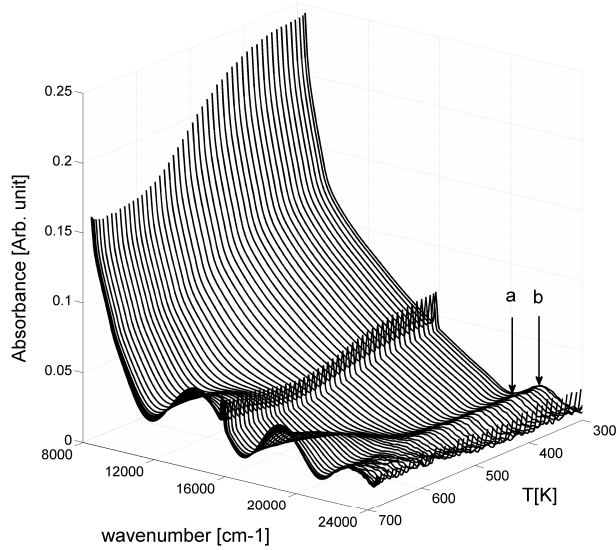
Figure 7.5. Temperature dependent switching of polished SmS: reflectance spectrum between 300 and 700K. Arrow a indicates the reflectance minimum of the metallic phase while arrow b shows the reflectance maximum due to remaining semiconducting phase SmS.

Figure 7.5 shows the temperature dependent reflectance of another 400nm thick SmS thin film measured using the same conditions as were used for the absorbance measurements. Initially the reflectance was of the metallic type with a minimum at 20000 cm^{-1} (indicated by arrow a) and a sharp increase of reflection with decreasing energy below this. A small maximum probably due to some remaining semiconducting phase was visible at 22000 cm^{-1} (indicated by arrow b). The reflectance remains constant up to around 400K after which the overall reflectance begins to decrease. No shift is seen in the position of the reflectance minimum at 20000 cm^{-1} until at 450K when the feature disappears and semiconducting features appear. Interference fringes typical of the semiconducting phase become clearly visible around 550K. These fringes then increase in magnitude until the film reaches 700K. The final spectrum shows the same structure as that seen for the semiconducting phase in figure 7.2C, although, as the interference fringes are thickness dependent, they appear in different positions to those seen in figure 7.2C.

Bzhalava *et al.* observe a time and temperature dependence for the thermally induced metal to semiconductor transition, i.e. films taking less time to switch at higher temperatures [7]. In order to investigate the switching speed of the thermally induced phase transition the ramp rate was varied from 5 to 20K/min. It was found that variations in the heating rate had no effect on the transition temperature range measured using reflectance spectroscopy. By measuring the temperature resolved reflectance of a film heated to only the middle of the measured transition range (550K) it was found that the reflectance followed the temperature, meaning that the phase transition stopped once a constant temperature was reached. This suggests that temperature rather than time is the dominant parameter with the films always switching in the same temperature range.
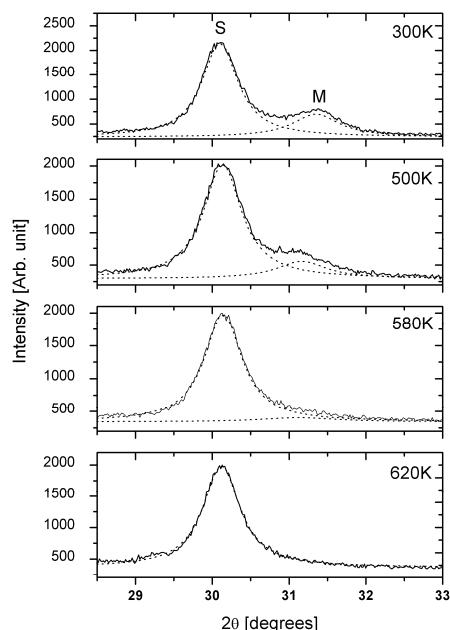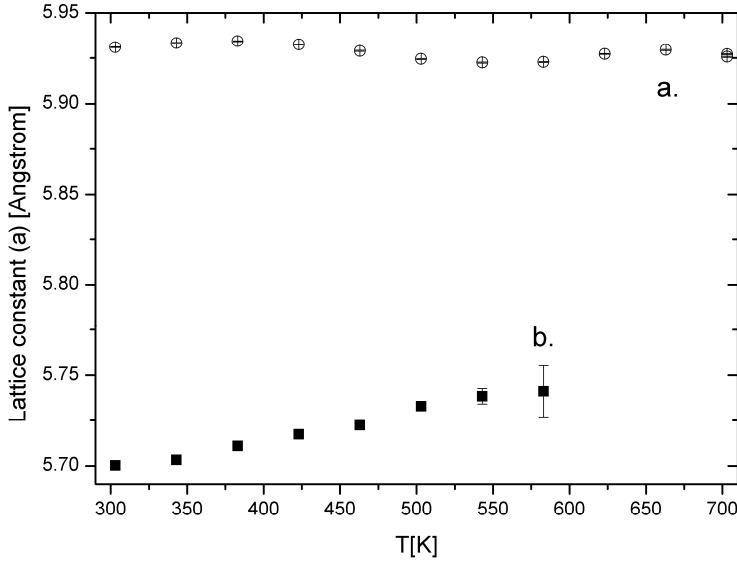
Figure 7.6. Temperature dependent metallic to semiconductor phase transition of an 800nm thick polished SmS thin film: Selected XRD results during the thermally induced M-S transition for the (200) semiconducting (S) and metallic (M) phase peaks. Dotted lines show the Lorentzian peak fitting used to calculate values in figures 7 and 8.

Temperature dependent X-ray diffraction measurements are shown in figures 7.6-7.8. Figure 7.6 shows the (200) diffraction peaks at different temperatures. At 300K both semiconducting and metallic phase diffraction peaks can be seen. By 500K the ratio between the metallic to semiconducting phase peak intensity has decreased and by 620K the metallic phase peak is absent.

The temperature dependent behaviour is summarized in figure 7.7 which shows how the lattice constant calculated from the position of the (200) peak changes throughout the experiment. The metallic phase shows a significant increase in lattice constant as the temperature increases, which suggests that it has a far larger thermal expansion than the semiconducting phase which shows

relatively little change with increasing temperature. The large difference in thermal expansion corresponds with the results of Iwasa *et al.* for the thermal expansion at low temperatures [24].

Figure 7.7. Temperature dependent metallic to semiconductor phase transition of an 800nm thick polished SmS thin film: Lattice constant calculated using the (200) diffraction peak: a) Semiconducting phase peak (open circles), b) metallic phase peak (filled squares).

Figure 7.8 shows the relative XRD peak intensity of the metallic phase of SmS in relation to the intensity of the semiconducting phase for the (200) XRD peak. Initially between 300 and 380K the diffraction intensity of the metallic phase is constant at around 32%. As the temperature increases to 540K the relative intensity drops linearly to around 8% and then vanishes entirely at 620K. The changes in the spectrum in figure 7.8 occur in the same temperature range as those observed in the optical measurements (figures 7.4 and 7.5).
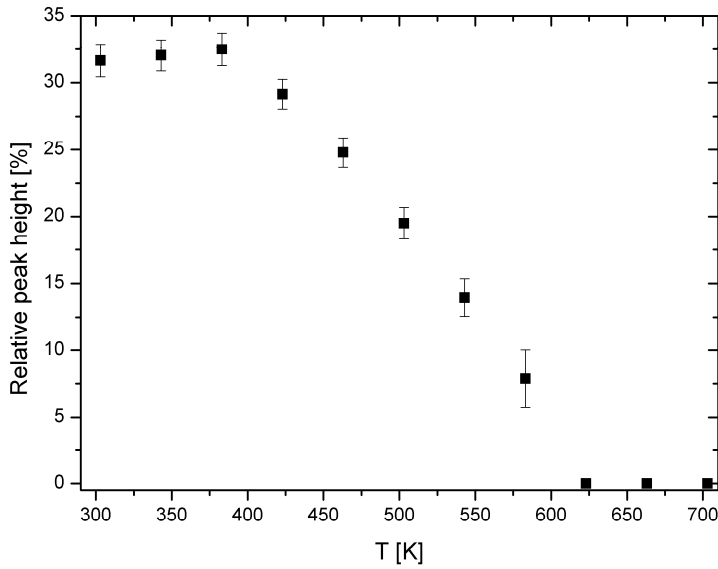
Figure 7.8. Temperature dependent metallic to semiconductor phase transition of an 800nm thick polished SmS thin film: Relative diffraction peak height (in percent) of the (200) metallic phase peak with regard to the (200) semiconducting phase peak.

7.4. Discussion

7.4.1. The Thermally Induced Phase Transition

The lattice parameter of the metallic phase of SmS calculated from the XRD peak position shows a significant shift to larger values due to the thermal expansion of the material (figure 7.7 curve b). No information on the thermal expansion of metallic phase SmS above 300K can be found but the thermal expansion measured by Iwasa *et al.* for a single crystal under pressure below 300K shows a far larger thermal expansion in the metallic phase than in the semiconducting phase [24] which corresponds quite well with what is seen for our measurements and which is generally seen when comparing metals and insulators. Finally the optical switching experiments, like those in figures 7.4 and 7.5, at different heating rates, indicate that switching is largely independent

of time and strictly follows temperature changes, suggesting that the metal to semiconductor phase transition and the thermal expansion of the metallic phase are related effects. Due to the heating of SmS there is a thermal lattice expansion (figure 7.7) with a corresponding reduction in crystal field splitting of the 5d-derived conduction band of SmS. This results in a shift to higher energy of the lower energy 5d state (bottom of the conduction band) towards the Sm^{2+} 4f ground state. We therefore conclude that the thermally induced phase transition in SmS thin films is mostly due to a reduction in crystal field splitting due to lattice expansion corresponding with the heating of the film.

An apparently continuous transition of the film was seen for both of the optical measurements (figures 7.4 and 7.5), with the metallic layer switching to the semiconducting phase between 350 and 700K. Although no earlier quantitative experiments exist on the continuous or discontinuous nature of the metal to semiconductor phase transition in thin films, all earlier work has reported a discontinuous phase transition in both directions for the change in resistivity [1] and reflectivity [2] of SmS single crystals under hydrostatic pressure.

We now discuss the expected changes in XRD peak intensity and position of the S and the M phases during a thermally induced continuous and discontinuous M to S phase transition for a polycrystalline thin film.

First we discuss a possible discontinuous thermally induced metallic to semiconducting phase transition of the metallic layer on a semiconducting film. The XRD spectrum will have two groups of peaks corresponding to the metallic and the semiconducting phases. During heating we should initially see both peaks shifting to lower values of 2θ but due to the higher thermal expansion of the metallic phase [25], we should see the metallic phase peak move towards that of the semiconducting phase.

At a critical temperature the lattice constant will reach a critical value and the grains will switch from the metallic to the semiconducting phase causing a discontinuous jump of the metallic phase peak intensities.

Because of the polycrystalline nature of the film however, grains will have a distribution of internal strains and thus a distribution of different lattice parameters and corresponding switching temperatures on a grain by grain basis, so that a gradual drop in metallic phase XRD peak intensities is expected until above a certain temperature all the metallic phase grains have phase changed and the metallic phase XRD peaks are gone.

Let us now assume a continuous thermally induced metallic to semiconductor phase transition in metallic grains forming the metallic layer on a further semiconducting film.

Again the XRD spectrum will have two groups of peaks corresponding to the metallic and the semiconducting phase. Besides the earlier discussed thermally induced lattice expansion, this time there will be additional metallic phase peak shifts. Since in a continuous phase transition more and more Sm^{3+} ions change into Sm^{2+} ions in the metallic layer (called mixed phase layer from here on) as the temperature rises, the lattice parameter of this mixed phase layer increases (Sm^{2+} is bigger than Sm^{3+}) and as a result the mixed-phase XRD peaks shift continuously towards the peaks of the pure S phase film until they eventually merge. Note that in the mixed phase film, Sm^{2+} and Sm^{3+} ions are randomly distributed with one corresponding lattice parameter so that the XRD spectrum has a discrete XRD spectrum corresponding to this mixed phase. The metallic phase peak intensity should not change significantly.

A shift in the peak position will be seen for both the continuous and discontinuous phase transitions due to thermal expansion as can be clearly seen in figure 7.7. It is possible to distinguish this effect from that of a continuous

phase transition, since in the case of a continuous phase transition the metallic phase XRD peaks will merge with the semiconducting phase peaks upon completion of the phase transition without losing intensity.

Studying the (200) metallic phase peak position and intensity (Figures 7.7 and 7.8) we can conclude that its temperature dependent behaviour resembles that of the discontinuous case most closely. A continuous shift is observed (figure 7.7) with a clear drop in intensity (figure 7.8) and the metallic phase peak is by no means merged with the semiconducting phase peak upon completion of the phase transition. All this suggests that the thermally induced metallic to semiconducting phase transition is discontinuous on a grain to grain basis, with grains switching between 380 and 620K. The measured optical spectra are the average of the corresponding metallic and semiconducting phase and therefore show a continuous behaviour.

7.5. Conclusion

Samarium Monosulphide thin films fabricated using electron beam evaporation of Samarium metal in a Hydrogen Sulphide atmosphere can be synthesised to a high quality. The resulting films show hysteretic temperature dependent behaviour due to the rearrangement of crystals and defects due to heating. The films can be switched to the metallic phase by polishing and a reverse transition can be induced thermally. The mechanism behind the thermally induced metal to semiconductor phase transition of SmS is most likely due to the thermal expansion of the metallic phase decreasing the crystal field splitting until the bottom of the 5d derived conduction band is shifted to higher energy than the 4f levels. It can be concluded on the basis of our temperature dependent optical and XRD data that although the metal to semiconducting thermally induced phase transition in SmS thin films appear continuous in optical spectra (reflection and transmission) it is in fact discontinuous on a grain-to-grain basis which is in accordance with previous studies on SmS single crystals.

Acknowledgements

References

[1] Jayaraman A, Narayanamurti V, Bucher E, Maines R G, 1970, Phys. Rev. Lett., **25** (20), 1430-3

[2] Kirk J L, Vedam K, Narayanamurti V, Jayaraman A, Bucher E,1972, Phys. Rev. B, **6** (8), 3023-6

[3] Kaminskii V V, Kazanin M M, Solov'ev S M, Sharenkova N V, Volodin N M, Semiconductors, 2006, **40** (6), 651-4

[4] Kaldis E, Wachter P, 1972, Solid State Comm., **11,** 907-12

[5] Kitagawa R, Takebe H, Moringa K, 2003, Appl. Phys. Lett., **82** (21), 3641-3

[6] Pohl D W, Badertscher R. Müller K A, Wachter P, 1974, Applied Optics, **13** (1), 95-7

[7] Bzhalava T L, Zhukova T B, Smirnov I A, Shul'man S G, Yakovleva N A, 1975, Sov. Phys. Solid State, **16** (12), 2428

[8] Bzhalava T L, Shulman S G, Dedegkayev T T, Zhukova T B, Smirnov I A, 1975, Phys. Lett. A, **55** (3), 161-2

[9] Jin P, Tazawa M, Huang J F, Tanemura S, 1998, Journal of Crystal Growth, **191**, 285-9

[10] Smirnov I A, Oskotskii V S, 1978, Sov. Phys. Usp., **21** (2), 117-40

[11] Batlogg B, Kaldis E, Schlegel A, Wachter P, 1976, Phys. Rev. B., **14** (12), 5503-14

[12] van der Kolk E, Dorenbos P, 2006, Chem. Mater., **18**, 3458-62

[13] Antonov V N, Harmon B N, Yaresko A N, 2002, Phys. Rev. B., **66**, 165208

[14] Volkonskaya T I, Shelykh A I, Bzhalava T L, Shul'man S G, Zhukova T B, Smirnov I A, 1975, Sov. Phys. Solid State, **17** (4), 751

[15] Domrachev G A, Zav'yalova L V, Svechnikov G S, Suvorova O N, Khanova A V, Schupak E A, Yarosh L A, 2003, Russian Journal of General Chemistry, **73**(4), 560-5

[16] Suryanarayanan R, Smirnov I A, Brun G, Shul'man S G, 1976, J. Phys. Colloques, **37**, C4- 271-4

[17] Sharenkova N V, Kaminskiĭ V V, Golubkov A V, Vasil'ev L N, Kamenskaya G A, 2005, Phys. Solid State, **47** (4), 622-6

[18] de Tomasi F, Perrone M R, Protopapa M L, Leo G, 2002, Thin Solid Films, **413**, 171-6

[19] Batlogg B, Schlegel A, Wachter P, 1977, Physica B, **86-88**, 229-30

[20] Tanemura S, Koide S, Senzaki Y, Miao L, Hirai H, Mori Y, Jin P, Kaneko K, Terai A, Nabatova-Gabain N, 2003, Applied Surface Science, **212-213**, 279-86

[21] Holtzberg F, Torrance J B, 1972, AIP Conf. Proc., **5**, 860-4

[22] Dorenbos P, 2003, J. Phys.:Condens. Matter, **15**, 4797-4807

[23] Pohl D W, Jaggi R, Gisler K, Weibel H, 1975, Solid State Comm., **17**, 705-8

[24] Iwasa K, Tokuyama T, Kohgi M, Sato N K, Mori N, 2005, Physica B, **359-361**, 148-50

[25] Freund L B, Suresh S, *Thin Film Materials: Stress, Defect Formation and Surface Evolution* (Cambridge, UK: Cambridge University Press)

Chapter 8: SmS thin films by RF magnetron sputtering

Abstract

Sm_xS thin films were fabricated by co-sputtering Sm metal and Sm_2S_3 targets by RF magnetron sputtering in an Ar atmosphere. Semiconducting phase SmS was fabricated when there were deposition rates of 0.35±0.05 nm/min for Sm and 1.1±0.05 nm/min for Sm_sS_3. By increasing the ratio of Sm to Sm_2S_3 it was possible to produce metal rich Sm_xS films. A rapid decrease in the lattice parameter was seen for Sm_xS films sputtered when $1.04<x\leq1.34$ as Sm^{2+} switched to Sm^{3+}, and films where $x \geq1.67$ closely resembled SmS switched to the metallic phase.

8.1. Introduction

Samarium monosulfide (SmS) is a semiconductor containing Sm^{2+} ions which undergoes a transformation to an isostructural metallic phase containing Sm^{3+} ions and free electrons under pressure [1]. The transition can also be induced by polishing the surface of a crystal or thin film to induce stresses, which leads to a metallic form of SmS which is stable at atmospheric pressure and room temperature [2, 3]. A similar phase has also been induced by doping SmS with metallic lanthanide monosulfides such as NdS or GdS or with SmP or SmAs [4-9]. It is also possible to make SmS thin films that are metallic under certain conditions without having to polish them [3, 10, 11]. A reverse metal to semiconductor transition can be made by releasing pressure on a sample, although a hysteresis is observed for the transition [1]. SmS switched to the metallic phase by polishing can be switched back to the semiconducting phase by heating the sample in a vacuum above 370K as described in chapter 7 [2]. A metal to semiconductor transition can also be laser induced, either through laser heating of the sample [12-14] or through a photoinduced transition [15].

8.1.1. Polishing and temperature induced phase transitions of SmS

Previously, in chapter 7, we studied the temperature induced metal to semiconductor phase transition of SmS thin films [2]. SmS thin films fabricated by electron beam evaporation of Sm metal in an H_2S atmosphere were polished into the metallic phase using alumina powder. The films could then be switched back to the semiconducting phase by heating in a vacuum. It was shown that the films switched discontinuously on a grain by grain basis between 380 and 620K.
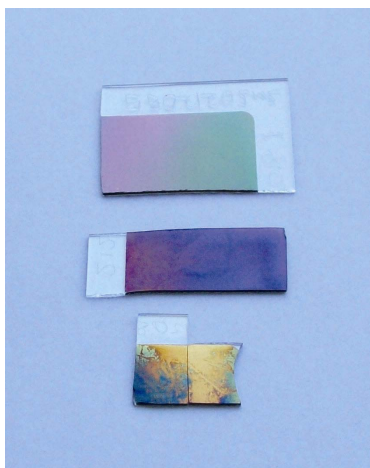

Figure 8.1. SmS thin film: Top: as deposited, middle: polished using alumina powder, bottom: coated with 100nm alumina before being polished using alumina powder.

*8.1.2. Al$_2$O$_3$ coated SmS thin films*

When the first series of SmS thin films were made, we coated a few of the early examples with a 100nm thick layer of Al_2O_3 as a protective coating. These films were poor in quality and initially switched from a grey-green semiconducting phase to a dark blue metallic phase by polishing. When parts of these films were then coated with alumina and then polished, golden patches, similar to those seen when good quality SmS thin films are polished, were clearly visible as is shown in figure 8.1. This suggested that the alumina coating might increase the stresses induced in the film by polishing and may be

beneficial in engineering the switching properties, such as the temperature induced transition, of SmS thin films.
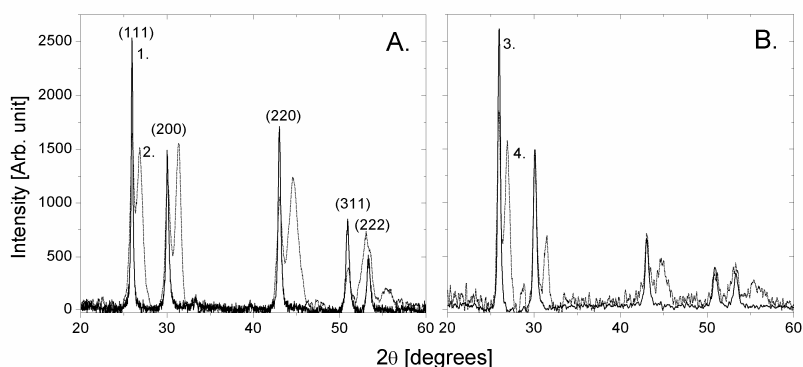
Figure 8.2. A: XRD of a 200nm thick SmS film on Vycor coated with 100nm of alumina (1) and a metallic layer (2). B: XRD of a 400nm thick partially confined SmS thin film on glass (3) and without (4) polished to induce a metallic layer (from [16])

Follow up work to fabricate better quality SmS thin films at the University of Gent, where the first films were made, showed that a SmS film deposited using the method outlined in chapter 7 and confined by a 100nm thick layer of alumina, switched to the same metallic phase as an uncoated (partially confined) SmS thin film as shown in figure 8.2 [16]. In figure 8.2A patterns for films coated with alumina in the semiconducting phase (1) and polished to induce a metallic phase layer (2) are shown. It can be seen that the (111), (200), (220), (311) and (222) phases, indicated in the figure for the semiconducting phase, can be seen for both semiconducting and metallic phases, similar to the situation shown in figure 8.2B for uncoated SmS thin films. This shows that the alumina coated films are crystalline SmS, and that, by polishing alumina coated SmS thin films, we achieve the same effect as in polishing uncoated films, that is we induce a layer of the metallic phase.
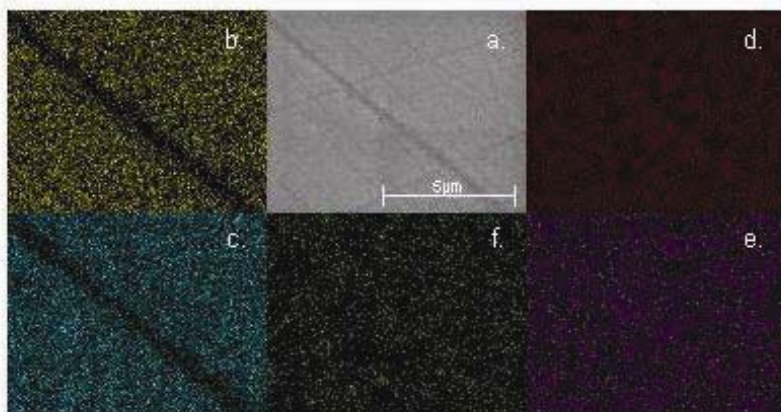
Figure 8.3. SEM-EDS of a polished confined SmS thin film on Vycor a) SEM image showing deep scratch through alumina and smaller scratches due to polishing with 0.3μm alumina powder, b-f) SEM-EDS map of b) Al, c) O, d) Sm, e) S and f) Si (from [16])

8.1.3. SEM and SEM-EDS of a polished alumina coated SmS thin film

In order to see how the surface of the alumina coated SmS thin films were affected by polishing Scanning electron microscope (SEM) and SEM-Energy-Dispersive-X-ray Spectroscopy (SEM-EDS) was used to study a SmS film confined by a 100nm thick Al_2O_3 layer as shown in figure 8.3. Figure 8.3a shows a SEM image that corresponds with the EDS map. The image is dominated by the appearance of a long scratch between the top left and bottom right hand corners. Smaller scratches can also be seen in the image. Figure 8.3.b shows the EDS map for Al and 8.3.c that of O. As the film is deposited on Vycor, a silica based glass, some of the O detected is from the substrate. However, from the Al map it can be seen that the deep scratch appears to cut through the alumina layer, while the smaller scratches are not visible in the EDS map, suggesting that they do not penetrate through the whole layer. However, despite the deep scratch, the SmS layer below indicated by maps 8.3.d for Sm and 8.3.e for S, appears to remain intact [16]. This suggests that SmS does not need to be abraded in order to generate the stresses required in order for it to switch through polishing.

All these observations suggest that SmS has applicability as a switchable material for applications such as thermochromatic glazing as not only are coated samples protected against oxidation, the fact that SmS switches by polishing without being abraded means that it is a far more practical material than would otherwise be the case.

There are still many issues regarding the properties of SmS that need to be investigated before the switching ability of this material may be utilised practically. Currently the thermally induced metal to semiconductor transition occurs upon heating, the opposite to what is required for thermochromic windows, and occurs at too high a temperature for domestic uses. Also, switching by polishing is a crude method that is difficult to reproduce exactly and impractical for use in a device. The ability to precisely control the switching ability of SmS is required and further investigations are needed in order to understand and control the polishing and thermally induced transitions. However, as electron beam deposition has several parameters which are difficult to control, it was decided to move to magnetron sputtering, which allows for greater control of the film deposition parameters. It was therefore decided to try to prepare SmS thin films in our laboratory using an AJA Orion magnetron sputtering system.

8.1.4. SmS thin films by Magnetron Sputtering

In 1998 Jin *et al* published a method for making SmS thin films by co-sputtering Sm metal sputtered using a DC source and Sm_2S_3 using a RF source in an Ar atmosphere [10]. The films sputtered in the original investigations by Jin *et al* were either semiconducting, metallic or an intermediate form of SmS. They concluded that the metallic and the intermediate phase were due to the presence of excess Sm [10, 11].

In this investigation we have sputtered Sm_xS thin films by co-sputtering an Sm metal target and a Sm_2S_3 pressed powder target using RF sputtering in order to

prepare SmS thin films in both the semiconducting and the metallic phase. RF sputtering is used for both sources as in our case it gave more stable sputtering powers for both targets. X-ray diffraction (XRD) has been used to characterise the films. Films were sputtered at both room temperature and at temperatures between 250 and 400°C.

The aim of this investigation is to sputter Sm_xS thin films under a variety of conditions, namely changing the sputtering power and the substrate temperature in order to see how the film properties and in particular the lattice parameter and semiconducting and metallic nature of SmS thin films change.


8.2. Experimental

Films were sputtered using an AJA Orion 5 Magnetron Sputtering system. Two targets were used: a Sm metal (99.99%) target, and a Sm_2S_3 powder target. Ar was used as the sputtering gas at 3mTorr of pressure. Films were sputtered on Corning 1737F glass substrates at room temperature and with the substrate heated to between 200 and 400°C by tungsten lamps. In order to achieve more uniform films, the substrate was rotated during sputtering.

8.2.1. Sm$_2$S$_3$ powder sputtering targets

No commercial Sm_2S_3 targets were available so we have made our own by pressing commercially available Sm_2S_3 powder (American Elements and DeMaCo) into a copper cup as shown in figure 8.4. The copper cup keeps the Sm_2S_3 powder contained and improves the thermal and electrical conductivity of the target. As Sm_2S_3 is air sensitive, a specially designed press meant that once the target was prepared in a N_2 glovebox, it could be kept in a N_2 atmosphere while being pressed outside the glovebox. The set-up was then moved back into the glovebox before the target was removed from the press, in an effort to reduce oxide contamination in our films.
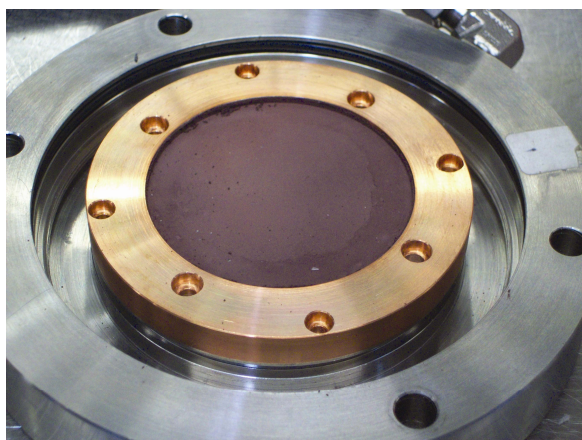
Figure 8.4. Sm$_2$S$_3$ pressed powder target
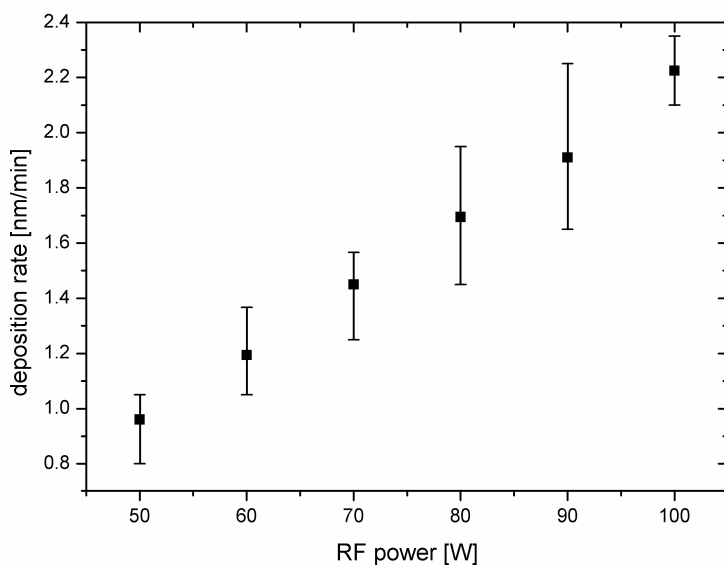
Figure 8.5. Average deposition rate in nm/min of Sm$_2$S$_3$

Due to the manufacturing process the Sm$_2$S$_3$ targets are slightly different from one another and this leads to variation in the sputtering rate. This is relatively small compared to the difference in deposition rate for Sm and Sm$_2$S$_3$, but it does mean that each target must be calibrated before use. Figure 8.5 shows the sputtering rate in nm/min of Sm$_2$S$_3$ measured using a McVac MCM-160 crystal thickness monitor and averaged for the four targets used. Error bars give an

idea of the range of sputtering rates seen. In general, although the rate is roughly linear for each of the four targets, there is a greater spread at higher sputtering powers. The reduced error bar at 100W is due to there being fewer measurements taken at this point since the fragile Sm_2S_3 targets are often damaged when sputtered at higher powers. When giving deposition rates or calculating Sm:S ratios in this chapter, the value used is that of the target used for that particular deposition.
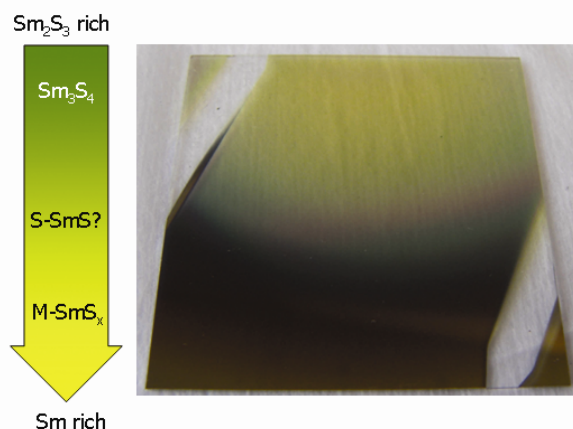
Figure 8.6. Thin film deposited using dual source RF magnetron sputtering with a gradient from a S rich (x<1) to a Sm rich (x>1) phase of Sm_xS.

8.2.2. Optimising Sputtering powers

By changing the ratio of sputtering powers and the tilt of the sputtering guns for the Sm and Sm_2S_3 targets it is possible to change the amount and distribution of material deposited on the substrate and thus the value of x for Sm_xS. For films with an excess of Sm (x>1) we expect to see more metallic behaviour, while for films where x is equal or close to 1 we should see semiconducting phase SmS. Where x drops below 1, it is a different phase, Sm_3S_4, which has both Sm^{2+} and Sm^{3+} ions that will be formed. If x drops much below 0.75 then Sm_2S_3 will start to be formed.

As an example of the range of compositions that can be seen in figure 8.6 we show a film deposited with a gradient in the ratio of the amount of Sm and Sm_2S_3 deposited, achieved by sputtering a film without rotating the substrate.

The top of the film will be Sm_2S_3 rich. As we move down the film to the Sm metal rich bottom edge, the ratio of Sm to Sm_2S_3 increases and the composition changes from Sm_3S_4 to metallic Sm_xS (x>1).

A series of films were sputtered using varying powers of Sm and Sm_2S_3. Initially Sm was sputtered using DC power, as in the investigation by Jin *et al.* [10], however we found that using RF power gave better results at low sputtering powers.

An issue arises in that as the Sm_2S_3 targets are made from pressed powder, rather than a single piece of metal or ceramic, they tend to crack very easily. In addition, the surface of the target frequently changes which leads to problems with maintaining the plasma required to sputter films. The targets tend to last longer at low powers (below 100W), but this is not ideal for sputtering semiconducting SmS thin films as the power required to deposit the same number of moles of Sm_2S_3 as Sm is far higher than that of Sm. This leaves us with a very restricted range of power ratios. There are two options to reduce the ratio of Sm to Sm_2S_3. One is to reduce the power for the Sm target and the other is to increase the power for the Sm_2S_3 target. As sputtering Sm_2S_3 at higher sputtering powers is impractical, we need to lower the sputtering rate for Sm. However, we are already sputtering close to the lower limit for the Sm target. By placing a grid in front of the Sm gun, as illustrated in figure 8.7, it was possible to reduce the sputtering rate of the Sm gun considerably. Figure 8.8 shows the difference in the thickness deposited per minute for a Sm gun sputtered with and without a grille over the front of the gun between 10 and 50W measured using a McVac MCM-160 crystal thickness monitor. The grille used reduced the sputtering rate by 85±2%.
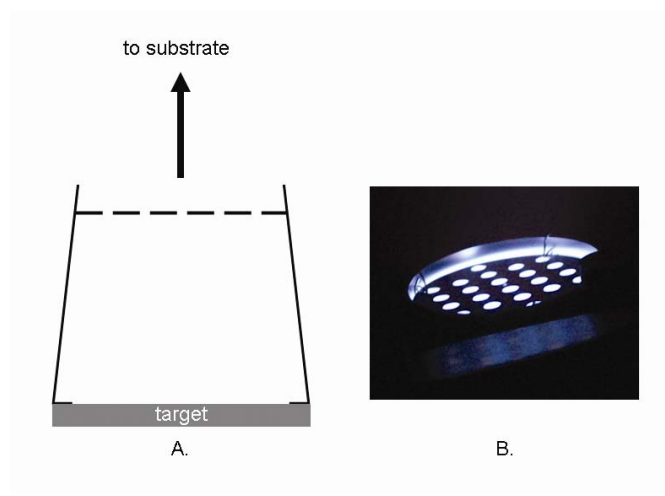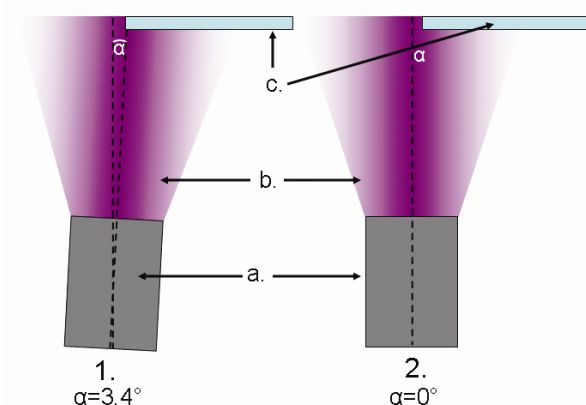
Figure 8.7. A. A schematic showing the positioning of a grille at the top of the chimney of a sputtering gun. B. A gun sputtering Sm with a grille at the top of the chimney.
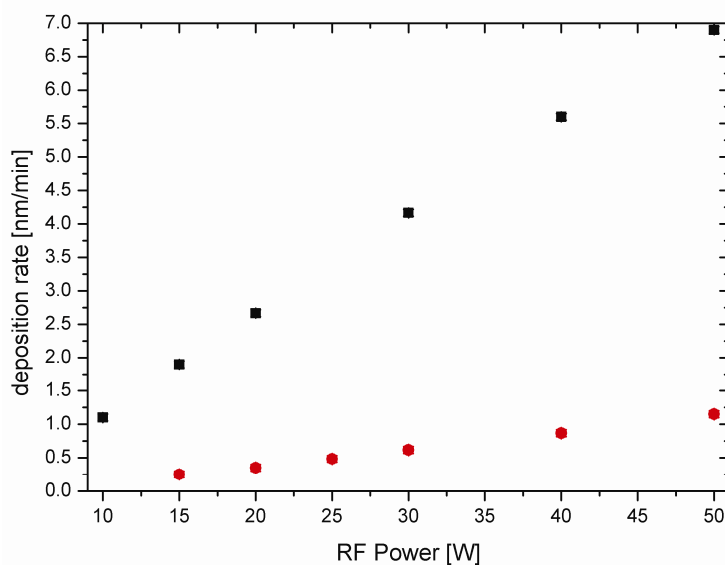
Figure 8.8. deposition rate in nm/min of a layer of Sm metal deposited with (red circles) and without (black squares) a grille placed across the opening of the sputtering gun.

Films were also sputtered with guns tilted away from the optimum angle. By changing the tilts it was possible to reduce or increase the amount of material deposited on the substrate, albeit at the cost of film uniformity. Figure 8.9 shows a schematic of two sputtering guns. The first gun is at the optimum tilt (in our case 3.4° from the vertical) so that the point where the amount of material is deposited is highest is at the edge of the film, leading to an even distribution of material if the substrate is rotated. The second gun is at a reduced tilt (~0°), so that the area where the maximum amount is deposited is now outside the substrate, leading to a reduction in the overall amount deposited on the substrate, but also a reduction in uniformity as some areas of the film will receive a net reduction compared to other areas when the substrate is rotated during deposition.

Figure 8.9. Schematic showing how changing the tilt of a sputtering gun changes the uniformity and distribution of the deposited material for 1: the optimal tilt (α=3.4°) and 2: a reduced tilt (α=0°). a= the sputtering gun, b= the sputtered material where pink= the highest and blue= the lowest concentration of sputtered atoms, c= the substrate.

In order to investigate how the distribution of material changes with tilt for our system, a series of Ti films were sputtered using the AJA Orion 5 sputtering system in our laboratory at different tilts of the sputtering gun. The substrate was not rotated, so that a wedge shaped film could be sputtered. In figure 8.10

the thicknesses of these wedge shaped Ti thin films are shown. The thicknesses
were measured by P. Brandhoff using a Dektak 3 profiler from the Department
of Chemical Engineering at TU Delft [17]. It can be seen that for films
sputtered at tilts lower than 3.4° (guns are less vertical), much more material is
deposited, and for guns with higher tilts than 3.4° (guns are more vertical)
much less material is deposited. It can also be seen that the gradient of
thickness of the wedges also changes depending on the tilt.
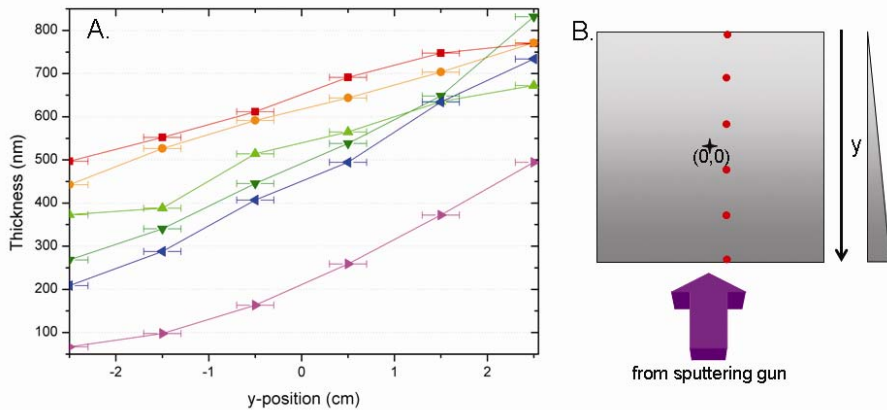
Figure 8.10. A: Change in thickness along the length from the thinnest to the thickest
part of Ti wedges sputtered with gun tilts of 16.2° (red squares), 13.1° (orange circles),
9.9° (green up triangles), 6.7° (dark green down triangles), 3.4° (blue left triangles)
and 0° (magenta right triangles) from the vertical. From [17]. B. Diagram showing
measuring points and direction of sputtering.

Figure 8.11 shows x as the RF power of the Sm and Sm_2S_3 guns changes for
different tilts of the sputtering guns. The values for x were obtained by
measuring thicknesses with a McVac MCM-160 crystal thickness monitor
present in the chamber of the magnetron sputtering system and using these
values to calculate the number of moles deposited per unit area per minute. The
ratio of Sm to S, x, could then be calculated using the relationship:

$$x = \frac{(M_{Sm} + 2M_{Sm_2S_3})}{3M_{Sm_2S_3}}$$

where M_{Sm} is the number of moles of Sm and M_{Sm2S3} is the number of moles of Sm_2S_3 deposited per unit area per minute.
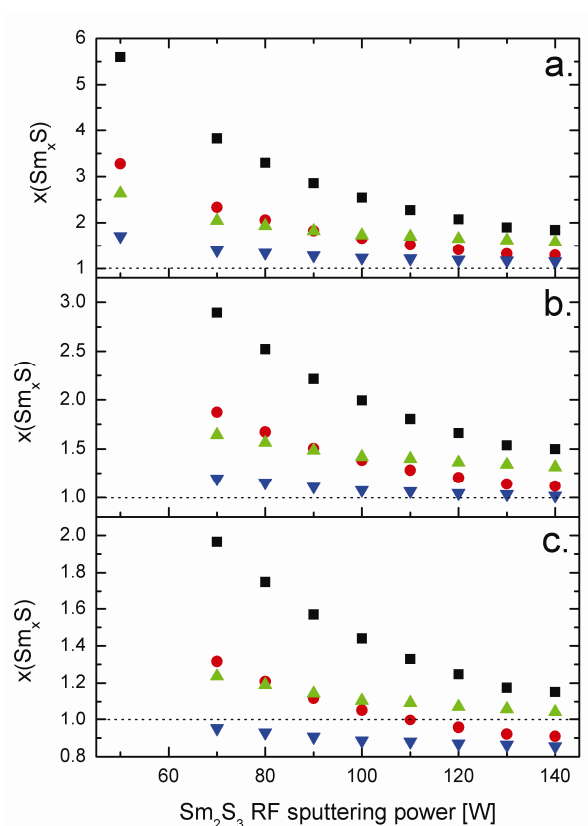
Figure 8.11. x, the ratio of Sm to S against the RF sputtering power of Sm_2S_3 for Sm powers: a=20W, b=15W and c=10W for different tilts of the sputtering guns. Black squares= 3.4° Sm and 3.4° Sm_2S_3, red circles= 0° Sm and 3.4° Sm_2S_3, green "up" triangles= 3.4° Sm and 6.7° Sm_2S_3, blue "down" triangles= 0°Sm and 6.7° Sm_2S_3

These values were then used to calculate the molar ratio of deposited Sm to Sm_2S_3. It can be seen that, according to these measurements, reducing the tilt of the Sm gun to 0° has the greatest effect, dramatically reducing the amount of Sm deposited, while increasing the tilt of the Sm_2S_3 gun to 6.7° increases the amount of Sm_2S_3 deposited. It can be seen that whereas sputtering using the optimal 3.4° tilts for both the Sm and the Sm_2S_3 guns leads for values of x greater than 1 throughout the range of sputtering powers used, by altering the

tilts, it is possible to reduce the powers required to achieve x=1, so that it is within the range of sputtering powers used.
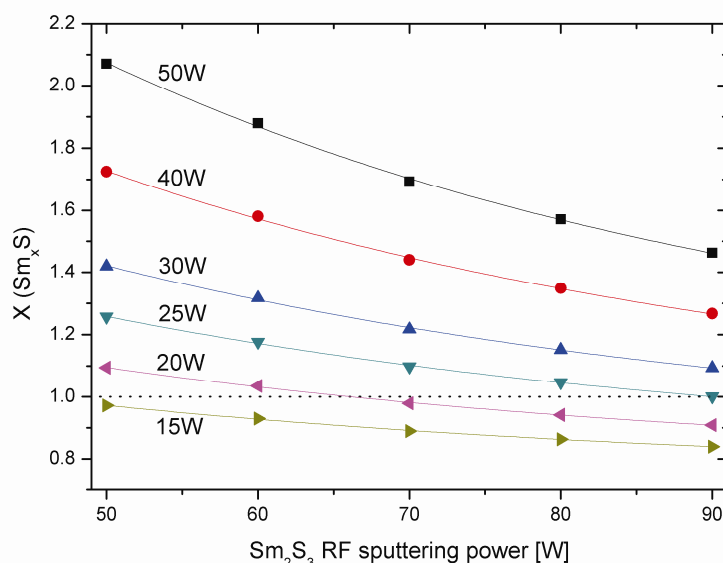
Figure 8.12. x, the ratio of Sm to S against the RF sputtering power of Sm_2S_3 when a grille has been placed over the opening of the Sm gun for Sm RF sputtering powers of: black squares= 50W, red circles = 40W, blue up triangles = 30W, dark cyan down triangles= 25W, magenta left triangles= 20W and dark yellow right triangles= 15W

Figure 8.12 shows x as the ratio between the RF power of the Sm and Sm_2S_3 guns when a grille is placed over the opening of the Sm gun. It can be seen that wherefore before x was always greater than 1 for guns at a tilt of 3.4°mm at powers between 10 and 20W RF (deposition rates of 1.4 and 3.4 nm/min) for Sm and 50 and 140W RF for Sm_2S_3 (0.825 to 3.35 nm/min) (figure 8.11), the ratio is now greatly reduced and x=1 between 60 and 65W RF power for Sm_2S_3 when Sm is sputtered at 20W RF due to the reduction in sputtering rate of the Sm gun.

Using these calibration measurements and calculations we can predict what value of x is found for a given combination of sputtering rates. When x is greater than one we expect to find metallic Sm_xS films. This is what we expect,

looking at figure 8.11, when we sputter with the guns at the optimal 3.4° tilts at powers between 10 and 20W RF power (1.4 and 3.4 nm/min) for the Sm gun and 50 and 140W RF power (0.825 to 3.35 nm/min) for the Sm_2S_3 gun. From the same figure we would expect semiconducting SmS thin films at a Sm power of 15W (1.3 nm/min) and a Sm_2S_3 power of around 130W RF (3.2nm/min) when the tilts are altered to 6.7° for the Sm_2S_3 gun and 0° for the Sm gun. If we sputter using the optimal tilts, but with the grille over the Sm gun, we expect that, from our calculations shown in figure 8.12 that we should see semiconducting SmS if we sputter Sm at 25W RF power (0.5 nm/min) and Sm_2S_3 at 90W RF power (1.7 nm/min), or between 60 and 70W RF sputtering power (1.1 and 1.3 nm/min) for Sm_2S_3 if we sputter Sm at 20W RF (0.35nm/min).
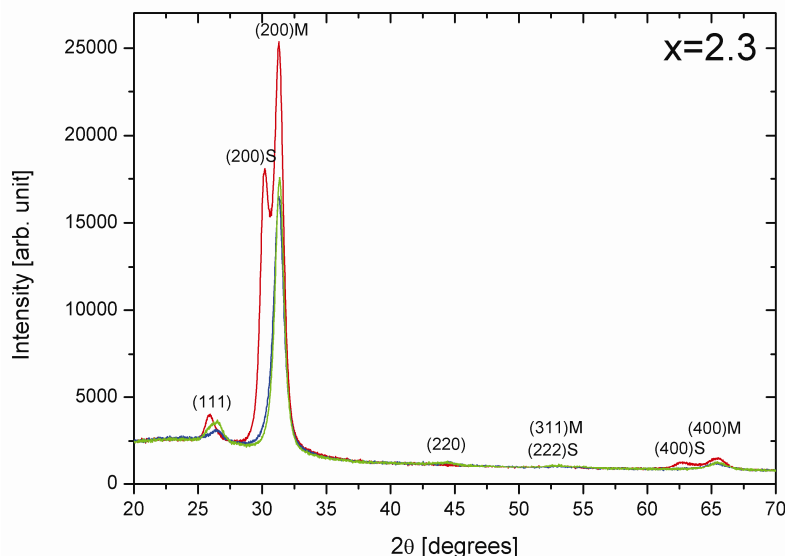
8.2.3. X-ray Diffraction (XRD)

In order to study the phase purity and lattice parameters of our films, XRD measurements were carried out using a PANalytical X'Pert Pro MPD X-ray diffractometer using Cu kα radiation. Lattice parameters were calculated from these measurements, using the SmS (200) peak.

8.3. Results

8.3.1. Sm_xS sputtered by the RF co-sputtering of Sm metal and Sm_2S_3

In figure 8.13 the XRD patterns of films sputtered with 15W RF power (1.7±0.05 nm/min) Sm and 80W RF power (1.7±0.05 nm/min) Sm_2S_3 are shown for films sputtered at room temperature, 250°C and 400°C. The strong (200) peak relative to the other XRD peaks suggests that the grains of the film are largely (200) orientated, rather than randomly orientated as was the case with the films sputtered using electron beam deposition in chapter 7. At room temperature only one metallic phase is seen with a lattice parameter measured for the (200) peak of 5.73Å. The film deposited at 250°C is very similar, although the lattice parameter for the (200) peak is shifted slightly to 5.70Å. However, for the film deposited at 400°C, two sets of peaks are seen

corresponding to a metallic phase with a lattice parameter of 5.71Å calculated for the (200) peak and a semiconducting phase with a lattice parameter of 5.91Å calculated for the (200) peak.

Figure 8.13. X-ray diffraction pattern of a Sm_xS thin film sputtered at 15W RF (1.7±0.05 nm/min) for Sm and 80W RF (1.7±0.05 nm/min) for Sm_2S_3 at: blue line = 25°C, green line = 250°C and red line = 400°C in an Ar atmosphere. Where possible the peaks have been labelled with their Miller Indices and whether they are attributable to the semiconducting (S) or the metallic (M) phase.

In figure 8.14 the XRD patterns of films sputtered with 20W RF power (2.7±0.05 nm/min) Sm and 50W RF power (1.0±0.05 nm/min) Sm_2S_3 at room temperature, 275°C and 400°C is shown. This sputtering power ratio leads to films with a much higher Sm content (higher x) than those shown in figure 8.13. The XRD patterns for films sputtered at higher temperatures with this ratio are far more complex. It is difficult to individually study the many peaks seen for the (200) reflection of the film sputtered at 400°C shown in figure 8.14. The peaks seen for the (200) reflection for the film sputtered at 275°C can be identified though and it can be seen that the film is split into three different components: a phase with a lattice parameter of 5.93Å, close to that of

semiconducting SmS, a second, more metallic phase with a lattice parameter of 5.72Å, which is close to that seen for the metallic phase of SmS obtained by polishing and a third peak with a lattice parameter of 5.42Å. This seems suspiciously small to be due to even metallic phase SmS though and may be indicative of another phase of different composition to Sm_xS in the film.
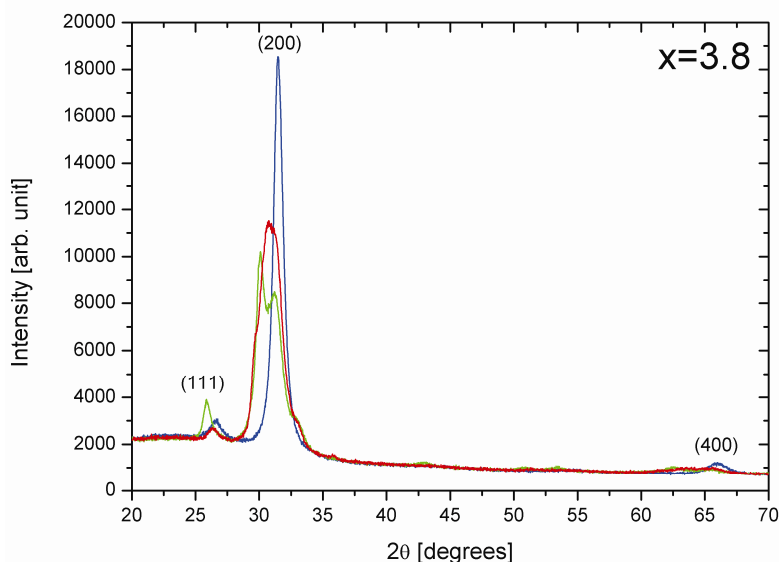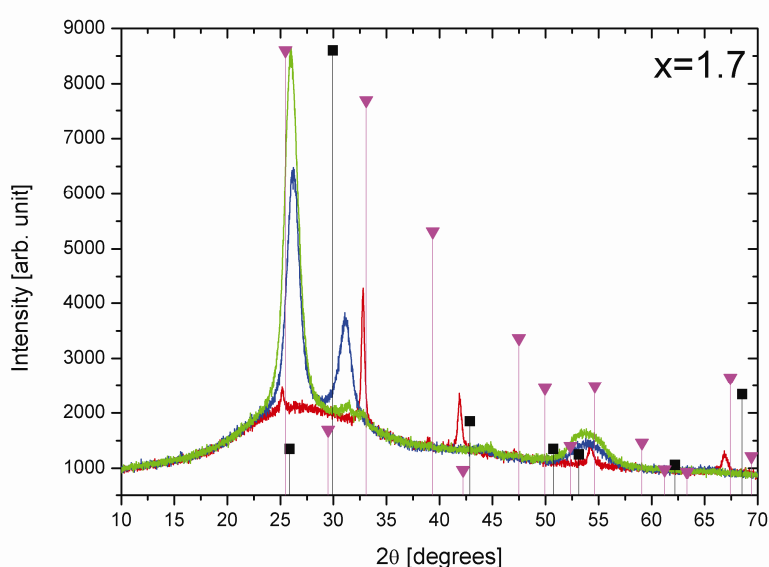

Figure 8.14. X-ray diffraction pattern of a Sm_xS thin film sputtered at 20W RF (2.7 ± 0.05 nm/min) for Sm and 50W RF (1.0 ± 0.05 nm/min) for Sm_sS_3 at: blue line = 25°C, green line = 275°C and red line = 400°C in an Ar atmosphere. Where possible the peaks have been labelled with their Miller Indices

In figure 8.15 the XRD patterns of films sputtered with 10W RF power Sm (1.1 ± 0.05 nm/min) and 60W RF power Sm_2S_3 (1.3 ± 0.05 nm/min) at room temperature, 275°C and 400°C are shown along with the diffraction patterns for S-SmS and Sm_3S_4. This ratio leads to a value for x of around 1.7, which suggests that the films are still Sm rich, but far less so than the films in figures 8.13 and 8.14 which have values for x of 2.3 and 3.8 respectively. Rather than the films splitting into different Sm_xS phases as the deposition temperature increases, the film sputtered at 275°C shows a strong Sm_3S_4 second phase while the film sputtered at 400°C shows peaks corresponding to Sm_3S_4 only.

It can also be seen that as x decreases the preferred orientation of grains in the film changes from the (200) to the (111) orientation as can be seen by the change in relative heights of these peaks.

Figure 8.15. X-ray diffraction pattern of a Sm_xS thin film sputtered at 10W RF (1.1±0.0167 nm/min) for Sm and 60W RF (1.27±0.0125 nm/min) for Sm_sS_3 at: blue line = 25°C, green line = 275°C and red line = 400°C in an Ar atmosphere. , black squares = expected pattern for semiconducting phase SmS [18], magenta triangles= expected pattern for Sm_3S_4 [19].
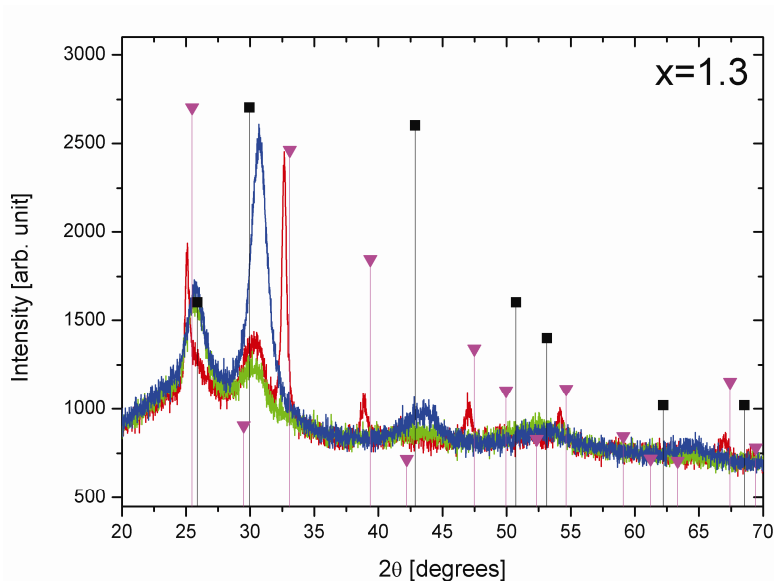
Figure 8.16. X-ray diffraction pattern of a Sm_xS thin film sputtered at 30W RF (0.6±0.05 nm/min) for Sm and 60W RF (1.1±0.05 nm/min) for Sm_sS_3 when the Sm gun has a grille over the exit at: blue line = 25°C, green line = 275°C and red line = 400°C, in an Ar atmosphere. Black squares = expected pattern for semiconducting phase SmS [18], blue triangles= expected pattern for Sm_3S_4 [19].
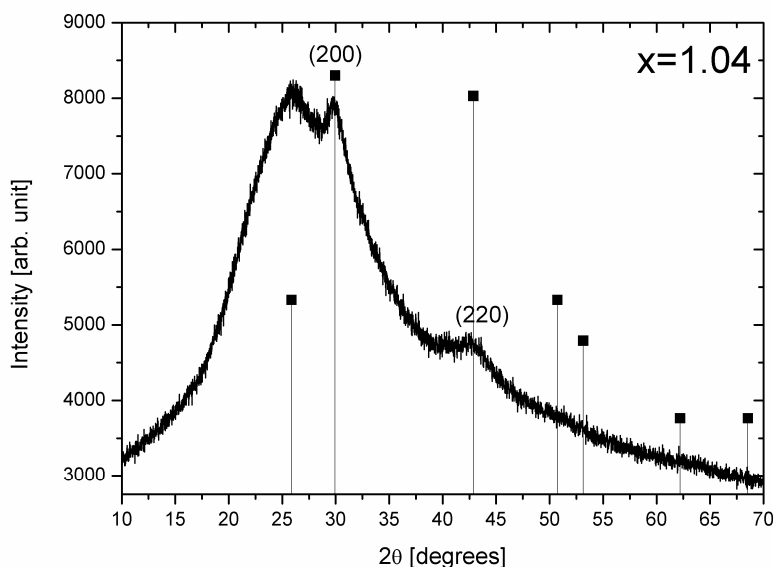
8.3.2. Sm_xS sputtered using a grille over the Sm gun

In figure 8.16 the diffraction patterns for Sm_xS films sputtered by co-sputtering Sm_2S_3 at 60W RF (1.1±0.05 nm/min) with Sm metal, where the Sm sputtering gun has a grille placed over the top so that when Sm is sputtered at 30W RF a deposition rate of 0.6±0.05 nm/min is obtained. The results are similar to figure 8.15 in that, while a Sm_xS phase is achieved at room temperature, films sputtered at elevated temperatures show an ever stronger Sm_3S_4 phase.

Using the same method to reduce the amount of Sm deposited at 60W RF (1.1±0.05 nm/min) Sm_2S_3 and 20W RF (0.35±0.05 nm/min) Sm, gives the film shown in figure 8.17. The pattern is poor in quality, due in part to the film being much thinner than the others, but the SmS (200) peak is clearly visible as is the (220) peak. The lattice parameter obtained using the (200) peak is 5.96±0.005Å, which is close to the literature value of SmS of around 5.97Å.

If we increase the sputtering power of Sm_2S_3 to 65W (1.2±0.05 nm/min) so that x=1.005, the resulting film has very poor crystallinity and no sign of the (200) or (220) peaks seen in figure 8.17 leading us to suggest that it is Sm_3S_4 rather than SmS.

Figure 8.17. X-ray diffraction pattern of a Sm_xS thin film sputtered at 20W RF (0.35±0.0083 nm/min) for Sm and 60W RF (1.1±0.0125 nm/min) for Sm_sS_3 when the Sm gun has a grille over the exit. Black squares = expected pattern for semiconducting phase SmS [18].

8.3.3. The effect of changing gun tilts on Sm_xS thin films

As well as placing a grille over the Sm gun, in section 2.2 it was also suggested that by changing the tilts of the sputtering guns we could also change the sputtering rate (figures 8.10 and 8.11) in order to approach x=1 at lower sputtering rates than would otherwise be the case. Figures 8.18 and 8.19 show x-ray diffraction patterns measured for Sm_xS thin films sputtered with the tilts of the sputtering guns changed from 3.4° to 0° for Sm and from 3.4° to 6.7° from the vertical for Sm_2S_3. Figure 8.18 shows a film sputtered using 50W RF power Sm (4.7±0.05nm/min) and 50W RF power (2.0±0.05 nm/min) Sm_2S_3 while figure 8.19 shows a film sputtered using 50W RF power Sm

(4.7±0.05nm/min) and 60W RF power (2.5±0.05nm/min) Sm_2S_3. XRD traces are shown for both the centre (black line) and the edge (red line) of both films as the edges of the films appear in all cases to contain less Sm than the centres. Also shown are the peak positions expected for semiconducting (black squares) and metallic (red circles) phase SmS and Sm_3S_4 (blue triangles).
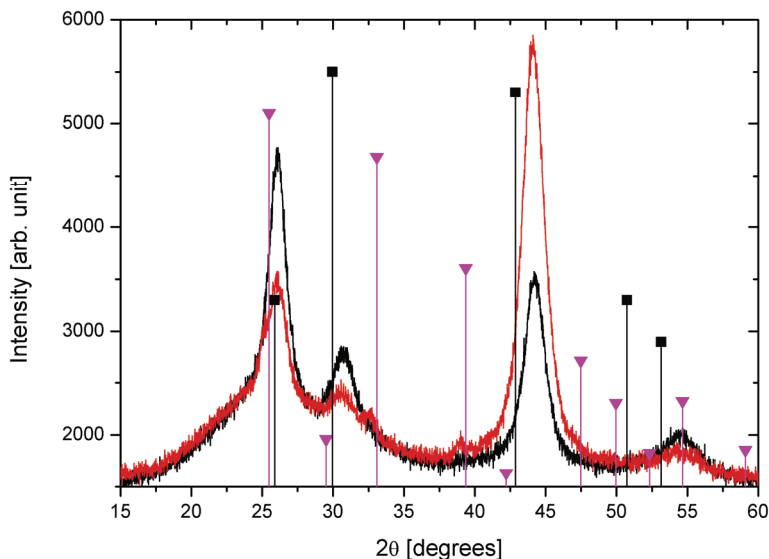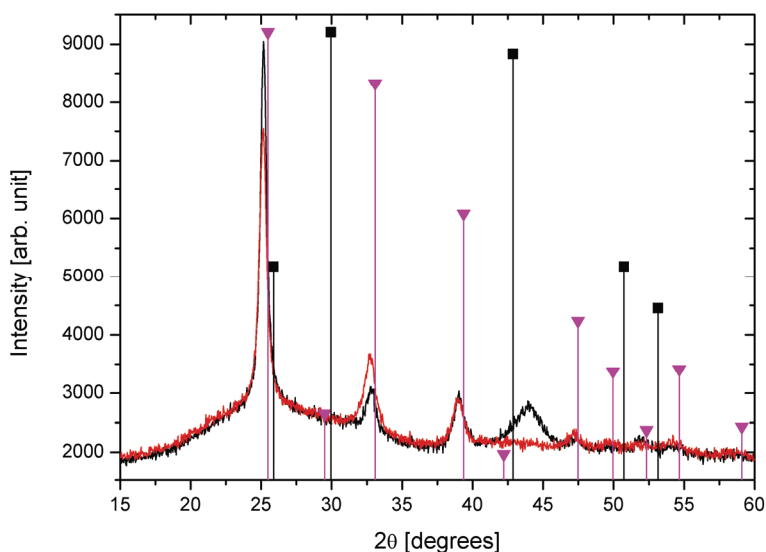

Figure 8.18. x-ray diffraction pattern of an Sm_xS thin film sputtered with 50W RF power (4.7±0.05nm/min) Sm at a tilt of 0° and 50W RF power (2.0±0.025 nm/min) Sm_2S_3 at a tilt of 6.7° in an Ar atmosphere at room temperature. Black line = centre of film, red line= edge of film, black squares = expected pattern for semiconducting phase SmS [18], magenta triangles= expected pattern for Sm_3S_4 [19].

In figure 8.18 we can see that while the centre of the film is Sm_xS, at the edges a second Sm_3S_4 phase can clearly be seen. The orientation of the films is different again, with the (220) peak appearing to be much stronger in intensity than the (111) and (200) peaks than has been seen in the earlier figures (8.13 to 8.17). For the film in figure 8.19 sputtered at 50W RF (4.7±0.05nm/min) for Sm and 60W RF (2.5±0.025 nm/min) for Sm_2S_3 it can be seen that the centre shows peaks that correspond with both the patterns for SmS and Sm_3S_4 while the edge shows peaks that correspond with Sm_3S_4 only. If we look back at

figure 8.11 we can see that when Sm was sputtered at 20W at a tilt of 0° x was predicted to be much greater than 1 even when Sm_2S_3 was 140W. However both of the films shown in figures 8.18 and 8.19 are sputtered at powers much higher than this and so x would be expected to be even greater. Instead the films both show the Sm_3S_4 phase, at least in part. The calculations for x in figure 8.11 were measured with a crystal thickness monitor positioned at the centre of where the substrate would be during a deposition. When the tilts are changed, not only is the amount of material deposited on the substrate changed, but also the distribution. This means that the rate measured in the centre of the film may no longer correspond with the average deposited across the substrate when it is rotated during deposition and therefore there is an error when the deposition rate is used to predict x in this situation.
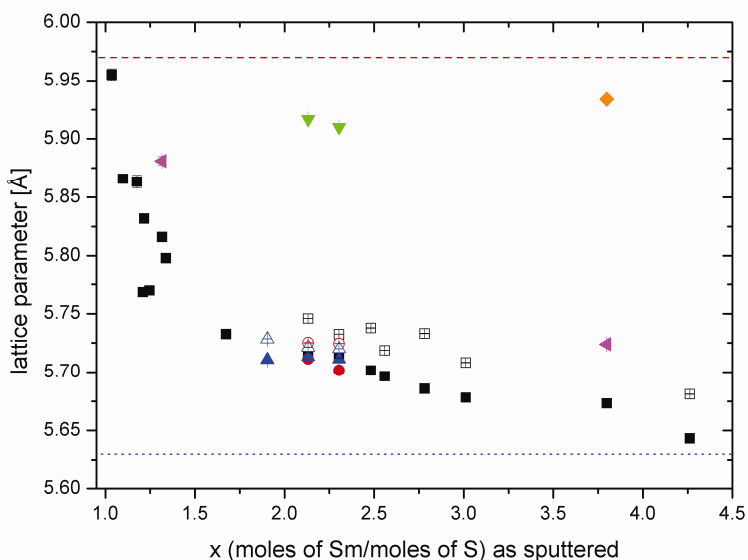

Figure 8.19. x-ray diffraction pattern of an Sm_xS thin film sputtered with 50W RF power (4.7±0.05nm/min) Sm at a tilt of 0° and 60W RF power (2.5±0.025 nm/min) Sm_2S_3 at a tilt of 6.7° in an Ar atmosphere at room temperature. Black line = centre of film, red line= edge of film, black squares = expected pattern for semiconducting phase SmS [18], magenta triangles= expected pattern for Sm_3S_4 [19].

Figure 8.20. Lattice parameters measured at the centre and edge of Sm_xS films sputtered at 25, 250 and 400°C, against x, the ratio of Sm to S. Black squares = 25°C, red circles = 250°, magenta left triangles = 275°C, orange diamonds= 275°C semiconducting phase, blue up triangles = 400°C, green down triangles = 400°C semiconducting phase. Solid symbols indicate a measurement in the centre of the film and unfilled symbols indicate a measurement at the edge of a film. The red dashed line indicates the lattice parameter of semiconducting SmS [18, 20-22] while the blue dotted line indicates the lattice parameter of metallic phase SmS.

8.3.4. Changes in the lattice parameters of Sm_xS thin films with x

Figure 8.20 shows the lattice parameters calculated using the SmS (200) peak for a series of films sputtered using RF sputtering for different ratios of Sm to Sm_2S_3 power. Also shown in figure 8.20 are the lattice parameters observed for the films deposited at elevated temperatures. As the films were slightly different at the edges compared to the centres, most of the films were measured both at the centre and at the edge. It can be seen that where there are high concentrations of Sm (high value for x) the lattice parameter is similar to that of SmS switched to the metallic phase under hydrostatic pressure (5.63Å). As

the amount of Sm is reduced the lattice parameter starts to approach that of semiconducting phase SmS (5.97Å).

Table 8.1. Lattice parameters and phases of Sm_xS films for different values at x sputtered at room temperature, between 250 and 275°C and at 400°C. Yellow= metallic Sm_xS, green= semiconducting SmS, blue= region of rapid increase in lattice parameter, red= Sm_3S_4, pink= suspected Sm_3S_4, grey = unknown phase, white= not measured

x	RT (25°C)	250-275°C			400°C	
4.26	5.643	---			---	
3.80	5.673	5.934	5.724	5.416	Multiple phases	
3.01	5.678	---			---	
2.78	5.686	---			---	
2.56	5.697	---			---	
2.48	5.701	---			---	
2.30	5.712	5.702			5.91	5.711
2.13	5.717	5.711			5.917	5.713
1.90	---	---			5.711	
1.67	5.733	?				
1.34	5.798	---			---	
1.32	5.816	5.881				
1.25	5.770	5.728			5.75	
1.22	5.832	5.820			---	
1.21	5.768	---			---	
1.18	5.863				---	
1.10	5.866	---			---	
1.04	5.955	---			---	
1.005		---			---	

In table 8.1 we display whether each film contains metallic Sm_xS, semiconducting SmS or Sm_3S_4 along with the lattice parameters for the Sm_xS and SmS phases for the different deposition temperatures studied. Lattice parameters which correspond to a metallic Sm_xS phase are shaded yellow, those corresponding to a semiconducting SmS phase are shaded green and cells corresponding to a film that was Sm_3S_4 are shaded red. The cells shaded blue

correspond to the films in the region where the lattice parameter increased rapidly over a small range of values for x. The cell shaded grey for x=3.80 is due to a peak that could not be attributed to a Sm_xS phase and too many peaks were seen to be able to separate for x=3.80 sputtered at 400°C. The cell marked ? was for a film where there was evidence of a Sm_xS phase but we were unable to identify its lattice parameter. The cells shaded pink were for films where the XRD pattern was not measured or the film was not synthesised, but, considering the surrounding films in the table, were considered to most likely be Sm_3S_4. It can be seen from the table that semiconducting phase SmS is only found in a few cases, either when the film is heated and it is seen along with metallic Sm_xS or when x=1.04 sputtered at room temperature. The film with a lattice parameter closest to that of pure metallic phase SmS switched under hydrostatic pressure (5.63Å) was found when x=4.26.

It can also be seen that the synthesis of Sm_xS is highly temperature dependent and what phase is seen for films deposited at elevated temperatures also depends strongly on x. As x decreases, Sm_3S_4 is produced at high temperatures rather than Sm_xS or a mixture of Sm_xS and S-SmS. In figure 8.21 a photograph of the front and rear of a film deposited at 400°C at 15W RF (1.7±0.05 nm/min) for Sm and 80W RF (1.7±0.05 nm/min) for Sm_2S_3 whose diffraction pattern was shown in figure 8.13. There is a visible colour difference between the bluey-purple front side of the film and the golden colour of the side closest to the substrate. Possibly when the films are sputtered on to the heated substrate the excess Sm diffuses through the film to the warmer area closer to the substrate. This would explain why two sets of XRD peaks are seen, one for semiconducting SmS, and the other for metallic SmS. Films deposited at elevated temperatures when Sm_3S_4 is produced, appear green on either side.
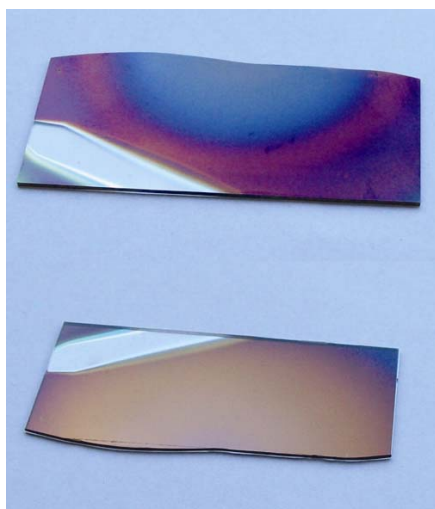
Figure 8.21. SmS thin film sputtered at 20W RF Sm and 80W RF power Sm_2S_3 at 400°C. Top: front, bottom: back

8.4. Discussion

8.4.1. The effect of x on the lattice parameter of Sm_xS

The magnetron co-sputtering of Sm metal and Sm_3S_3 powder targets can be used to make films with different compositions, from Sm deficient Sm_3S_4 to Sm rich Sm_xS (x>1). The results in figure 8.20 can be divided into three sections. Where x is ≥ 1.67 the lattice constant decreases steadily as x increases, in the second section where $1.04<x\leq1.34$, there is a rapid increase in lattice parameter, until in the third region where x=1.04, we see a lattice parameter that is close to semiconducting phase SmS.

As the change in lattice parameter for films sputtered at room temperature changes with x, it can be assumed that the excess Sm is responsible for the metallic SmS-like behaviour of these films: the lattice constant in the region of 5.7 to 5.63Å and the blue to golden colour of the films as seen in figure 8.1 for polished SmS. There are two possible causes for this effect: the excess Sm induces stresses within SmS, acting on the film in a similar way as the application of hydrostatic pressure on a sample of SmS. The second cause

could be that the excess Sm is acting as an electron donor. It is likely that both of these effects are acting on our films. However, the question is, where does the excess Sm fit in our films?

The first situation to consider would be the creation of grains of Sm metal mixed in with grains of SmS in the films. In this case we would expect to see some sort of effect in the XRD patterns, either in the appearance of a secondary Sm metal phase in the pattern or in an increasingly large amorphous background as x increases, neither of which has been observed.

The other way that the excess Sm could be incorporated in the films would be within the SmS lattice, either filling up defect sites, or sitting in interstitial sites, charge compensated by an electron in a corresponding site. For instance when a Sm^{2+} ion is replaced by a Sm^{3+} ion and an e^- fills a defect site to compensate.

The rapid increase in lattice parameter when $x<1.67$ is reminiscent of a phase transition as is seen for SmS doped with other lanthanides such as La or Gd [7-9], where, at a critical concentration, the lattice pressure is such that Sm^{2+} ions switch to Sm^{3+}, with a corresponding drop in ionic radius/ lattice parameter. Our situation is different as, for SmS doped with other lanthanides such as Gd or La, the Ln^{3+} ion replaces a Sm^{2+} ion, while in the case of Sm_xS thin films where $x>1$, we are adding excess Sm to the system rather than replacing an Sm^{2+} ion with a Sm^{3+} ion. It is logical that the two cases would have an overall effect that is quite similar, at least when regarding the change in lattice parameter as in both cases, we are deforming the SmS lattice by adding ions, and in both cases we are introducing excess electrons to the system. We can therefore say that the region where $1.04<x\leq1.34$ is the critical region where Sm_xS undergoes a phase transition and Sm^{2+} ions are being switched to Sm^{3+}.

However, while we see a rapid increase in lattice parameter in this region, there is no abrupt jump visible between one film and the next, which suggests a continuous transition rather than the discontinuous transition normally expected with SmS. It is probable that the addition of excess Sm ions acts differently to the substitution of Ln^{3+}, either masking or preventing a discontinuous semiconducting to metallic phase transition as x increases.

8.4.2. Effect of substrate temperature

The deposition temperature has a strong effect on the sputtered films. Films sputtered at higher temperatures appear to separate into two or more phases, which can include S-SmS, M-SmS and Sm_3S_4. The temperature at which this phase separation takes place varies from film to film. For films with a lot of extra Sm, a M-SmS and a S-SmS phase appears, while for films with less excess Sm, Sm_3S_4 appears as the second phase. As x approaches 1 still further, Sm_3S_4 appears as the dominant or only phase in the film.

A possible explanation is that when we sputter at elevated temperatures the excess Sm ions diffuse through the film, forming regions with higher and lower concentrations of Sm. This corresponds with what we see in figure 8.21 where it can clearly be seen that the region of the film closest to the substrate is golden while the area closest to the film-air interface is bluey-purple and in the slightly lower lattice parameter of the metallic Sm_xS phase for this film compared to the corresponding film deposited at room temperature.

For films with less excess Sm (i.e. x=1.25) we see Sm_3S_4 and a metallic Sm_xS phase with a lattice parameter much smaller than that of the corresponding film deposited at room temperature. The film deposited at room temperature has a lattice parameter that lies in the critical region highlighted in table 8.1. The separation of the film into a lattice parameter corresponding to the metallic Sm_xS region in figure 8.20 and Sm_3S_4 suggests that the films in the critical region are less stable and that the other compositions are more favourable. This would correspond with the region where $1.04 < x \leq 1.34$ being the region where the phase transition occurs and Sm^{2+} is beginning to be switched to Sm^{3+}.

8.4.3. Future applications

The manufacture of Sm_xS thin films where $x \geq 1$ by the RF magnetron co-sputtering of Sm metal and Sm_2S_3 pressed powder targets can successfully produce films that are similar to metallic phase SmS switched by either the application of hydrostatic pressure or by polishing to induce stresses in the

material. This is desirable as this makes a systematic study of how optical, thermal or electrical properties of Sm_xS vary as a function of x possible.

The separation of phases for films deposited at elevated temperatures is both interesting regarding future investigations into how the separation occurs and is possibly also interesting technologically as it may be possible to utilise this effect. S-SmS and M-SmS have very different optical and thermal properties as described in chapter 7 and there are examples in the literature of Sm_xS with a dopant gradient across a crystal, showing unusual thermoelectric properties [23, 24]. The films produced by the RF magnetron co-sputtering of Sm and Sm_2S_3 could provide a new way to investigate these effects.

8.5. Conclusions

Sm_xS thin films were produced by the co-sputtering of Sm and Sm_2S_3 targets using RF magnetron sputtering in a 3mTorr Ar atmosphere. By changing the ratio of Sm to Sm_2S_3 sputtered it was possible to control the film parameters, namely the lattice parameter, with films ranging from a phase similar to metallic phase SmS to semiconducting SmS as x approached 1. In the region where $1.04 < x \leq 1.34$ Sm^{2+} ions are increasingly switched to Sm^{3+} and when x ≥ 1.67, most of the Sm^{2+} has switched. Increasing the deposition temperature caused multiple phases to appear on one film. By controlling the ratio of sputtering powers (deposition rates) or changing the deposition temperature it is possible to control the properties of Sm_xS thin films.

References

[1]   Jayaraman A, Narayanamurti V, Bucher E and Maines R G 1970 *Physical Review Letters* **25** 1430-3

[2]   Rogers E, Smet P F, Dorenbos P, Poelman D and van der Kolk E 2010 *Journal of Physics: Condensed Matter* **22** 015005

[3]   Bzhalava T L, Zhukova T B, Smirnov I A, Shul'man S G and Yakovleva N A 1975 *Soviet Physics, Solid State* **16** 2428

[4]   Henry D C, Sisson K J, Savage W R, Schweitzer J W and Cater E D 1979 *Physical Review B* **20** 1985-90

[5]   von Molnar S, Penney T and Holtzberg F 1976 *Journal de Physique, Colloque* C4-241-C4-8

[6]   Jayaraman A. and Maines R G 1979 *Physical Review B* **19** 4154-61

[7]   Tao L J and Holtzberg F 1975 *Physical Review B* **11** 3842-9

[8]   Jayaraman A, Dernier P and Longinotti L D 1975 *Physical Review B* **11** 2783-94

[9]   Smirnov I A and Oskotskii V S 1978 *Soviet Physics Uspekhi* **21** 117-40

[10]   Jin P, Tazawa M, Huang J F and Tanemura S 1998 *Journal of Crystal Growth* **191** 285-9

[11]   Tanemura S, Koide S, Senzaki Y, Miao L, Hirai H, Mori Y, Jin P, Kaneko K, Terai A and Nabatova-Gabain N 2003 *Applied Surface Science* **212-213** 279-86

[12]   Pohl D W, Badertscher R, Müller K A and Wachter P 1974 *Applied Optics* **13** 95-7

[13]   Pohl D W and Holtzberg F 1975 *Applied Optics* **14** 1060-1

[14]   Kaminskii V V 1978 *Fiz. Tverd. Tela* **20** 1742-4

[15]   Kitagawa R, Takebe H and Morinaga K 2003 *Applied Physics Letters* **82** 3641-3

[16]   Rogers E, Smet P F, Dorenbos P, Poelman D and Van der Kolk E 2010 Reversible first order semiconductor to metal phase transition in fully and partially confined SmS thin films. In: *Novel Aspects of Surfaces and Materials 3,* pp 100-1

[17]   Brandhoff P 2012 Switchable Lanthanide-based materials: The production and characterisation of samarium monosulfide thin films. *Radiation, Detection and Medical Imaging,* (Delft: Delft University of Technology) p 90

[18]   Sipe and McCarthy 1974 *ICDD Grant-in-Aid* powder diffraction file (ICDD) 026-1479

[19]   Vantien V and Khodadad P 1969 *Bull. Soc. Chim. Fr.* powder
        diffraction file (ICDD) 04-004-1131

[20]   Bzhalava T L, Shul'man S G, Dedegkayev T T, Zhukova T B and
        Smirnov I A 1975 *Physics Letters A* **55** 161-2

[21]   Suryanarayanan R, Smirnov I A, Brun G and Shul'man S G 1976
        Journal de Physique, Colloque C4 **37** 271-4

[22]   Batlogg B, Schlegel A and Wachter P 1977 *Physica B* **86-88** 229-30

[23]   Kaminskii V V and Kazanin M M 2008 *Technical Physics Letters* **34**
        361-2

[24]   Kaminskii V V, Didik V A, Kazanin M M, Romanova M V and
Solov'ev S V 2009 *Technical Physics Letters* **35** 981-4

Summary

Knowledge on the energy of the 4f and 5d bands of lanthanide based materials is vital for understanding their properties, particularly their optical properties and electronic structures. Being able to manipulate these energies allows us to utilise these properties more efficiently.

In chapters 2 to 4 of this thesis it is shown that the electronic structure and optical properties of lanthanide based materials can be predicted using an empirical model. It is also shown that we can use results obtained by this model to understand why some materials deviate from their expected properties, namely in the non-existence of some Eu^{3+} compounds, such as Eu_2S_3 and $EuAs$, and why some materials can undergo valence changes, such as SmS and NdI_2, or have interconfigurational valences like PrI_2 or $TmSe$. It was also shown that we can use trends observed in the results obtained in these three chapters to predict the energy levels of compounds for which relevant optical data is unobtainable.

In chapter 5 it is then shown, through the measurement of the optical properties of the lanthanide diiodides NdI_2, SmI_2, EuI_2, DyI_2, TmI_2 and YbI_2, that it is possible to accurately estimate energy levels for fully concentrated lanthanide based materials using the schemes in Chapter 3, and that the schemes are accurate to within 0.11eV of the measured data. This chapter also suggests that even within such a well-known family of compounds, such as the diiodides, which had not previously been comprehensively studied optically, there are still interesting measurements to be made that can bring to light new explanations for the puzzling behaviour of some compounds, such as PrI_2.

Chapters 6 to 8 concerned the manipulation of the 4f→5d gap of lanthanide based materials. In chapter 6, $EuO_{1-x}N_x$ powders were fabricated and their lattice parameters and $4f^7 \rightarrow 4f^6 5d^1$ optical bandgaps were measured. It was

shown that as the amount of EuN in the sample increased, the bandgap and lattice parameter both decreased.

In chapter 7 the switchable material SmS was introduced. It was shown that there is a semiconductor to metal transition induced by polishing a SmS thin film in order to induce stresses in the film that acts in a similar way to applying hydrostatic pressure on the sample. This phase transition is due to the applied pressure increasing the crystal field splitting of the 5d band so that the bottom of the 5d conduction band overlaps with the occupied 4f(2+) ground state. It was then shown that when the sample is heated in a vacuum, the material switches back to the semiconducting phase by the annealing of these stresses discontinuously on a grain by grain basis.

In chapter 8, it is shown that SmS thin films can be made by the RF magnetron co-sputtering of Sm and Sm_2S_3. It is shown that an excess of Sm causes the films to appear metallic rather than semiconducting and that the lattice parameter decreases as the amount of excess Sm increases. It is also shown that the process is temperature sensitive, with films deposited at elevated temperatures showing multiple phases under XRD.

This part of the thesis shows that it is possible to control the 4f→5d bandgap of a Ln based material, either internally, by alloying a compound with a similarly structured one ($EuO_{1-x}N_x$) or with excess Ln metal ions (Sm), or by a perturbation in the material's external environment (SmS). The second of these suggests that, if such a perturbation can be controlled and optimised, Ln based materials could be useful in applications where a semiconductor to metal transition is needed, for instance in temperature controlled switchable glazing, where a coating of a material such as SmS switches from a more transparent semiconducting phase to a highly reflective metallic phase when the external temperature exceeds a certain value. The manipulation of the 4f→5d bandgap may also be useful in other non-switching applications. In particular it could be used in luminescent materials, such as phosphors or scintillators, to tune the wavelengths absorbed and/or emitted.

Samenvatting

Kennis over de energie van de 4f en 5d banden van lanthanide materialen is cruciaal om hun eigenschappen te begrijpen, met name de optische eigenschappen en de elektronische structuur. Het kunnen manipuleren van deze energieën stelt ons in staat deze eigenschappen efficiënter te gebruiken.

In de hoofdstukken 2 tot en met 4 van dit proefschrift wordt aangetoond dat de elektronische structuur en optische eigenschappen van op lanthanide gebaseerde materialen kunnen worden voorspeld met behulp van een empirisch model. Ook wordt aangetoond dat we de resultaten van dit model kunnen gebruiken om te begrijpen waarom sommige materialen afwijken van de verwachting, zoals het niet-bestaan van sommige Eu^{3+} verbindingen zoals Eu_2S_3 en EuAs, of waarom sommige materialen valentieveranderingen kunnen ondergaan zoals SmS en NdI_2, of waarom PrI_2 of TmSe interconfigurationele valenties hebben. Verder wordt aangetoond dat de trends die volgen uit de resultaten van deze drie hoofdstukken kunnen worden gebruikt om energiebanden te voorspellen van materialen waar geen betrouwbare optische data van beschikbaar is.

In hoofdstuk 5 wordt aan de hand van metingen van de optische eigenschappen van de lanthanide di-jodiden NdI_2, SmI_2, EuI_2, DyI_2, TmI_2 en YbI_2 duidelijk dat het mogelijk is om nauwkeurige schattingen te maken van energieniveaus van volledig geconcentreerde lanthanide materialen op basis van energie schema's die zijn bepaald in hoofdstuk 3. Dit kan met een nauwkeurigheid gedaan worden die beter is dan 0.11 eV. Dit hoofdstuk laat tevens zien dat zelfs voor bekende families van verbindingen, zoals de di-jodiden, waarvan de optische eigenschappen voorheen niet grondig bestudeerd zijn, interessante metingen kunnen worden uitgevoerd die bijvoorbeeld een verklaring aan het licht brengen voor het raadselachtige gedrag van verbindingen zoals PrI_2.

Hoofdstukken 6 tot en met 8 betreffen de manipulatie van de 4f→5d energie van op lanthanide gebaseerde materialen. In hoofdstuk 6 wordt de synthese van $EuO_{1-x}N_x$ poeders beschreven evenals de experimentele bepaling van de kristalstructuur parameters en de $4f^7→4f^65d^1$ optische bandgaps. Er wordt aangetoond dat als de hoeveelheid EuN in de monsters toeneemt, de bandkloof en de roosterparameters beide afnemen.

In hoofdstuk 7 wordt het schakelbare materiaal SmS geïntroduceerd. Er wordt aangetoond dat er een overgang van halfgeleider naar metaal kan worden geïnduceerd door een SmS film te polijsten. De spanningen die door het polijsten geïnduceerd worden in de film kunnen worden vergeleken met het toepassen van hydrostatische druk, waarvan bekend is dat het de fase overgang veroorzaakt. Door de spanningen in de film ontstaat er een toename van de kristalveldsplitsing van de 5d-banden waardoor de bodem van de 5d-geleidingsband onder de bezette 4f(2+) grondtoestand zakt. Vervolgens wordt aangetoond dat wanneer de geschakelde film wordt verwarmd in een vacuüm, het materiaal discontinu en op een korrel- bij- korrel basis terugkeert naar de halfgeleidende fase als gevolg van het "annealen" van de spanningen in de film.

In hoofdstuk 8 wordt aangetoond dat SmS films kunnen worden gemaakt met behulp van RF magnetron co-sputteren van Sm en Sm_2S_3. Het blijkt dat bij een Sm overmaat, SmS films metallisch in plaats van halfgeleidend worden. Bovendien neemt de roosterparameter af naarmate de hoeveelheid Sm toeneemt. Tevens bleek dat het depositieproces temperatuurafhankelijk is omdat XRD patronen van films gedeponeerd bij hogere temperatuur meerdere kristalfasen laten zien. Dit deel van het onderzoek laat ook zien dat het mogelijk is om de 4f→5d bandgap van een op lanthaniden gebaseerd materiaal te beïnvloeden, hetzij intern door te legeren met een verbinding met een vergelijkbare structuur ($EuO_{1-x}N_x$) of met een overmaat aan Ln metaalionen (Sm), hetzij extern door een verstoring aan te brengen in de omgeving van het materiaal (SmS). Dit laatste suggereert dat indien een dergelijke verstoring kan

worden gecontroleerd en geoptimaliseerd, lanthanide materialen nuttig kunnen worden toegepast als films op bijvoorbeeld temperatuur gecontroleerd schakelbaar glas. SmS films zouden dan kunnen schakelen van een transparante halfgeleidende toestand naar een sterk reflecterende metallische toestand wanneer de buitentemperatuur boven een bepaalde waarde stijgt. De manipulatie van de 4f→5d bandkloof kan ook bruikbaar zijn in andere toepassingen waarbij het schakelgedrag geen rol speelt. In het bijzonder kan het worden benut om in luminescerende materialen de golflengten van geabsorbeerd en uitgezonden licht af te stemmen.

Acknowledgments

There have been so many people that have helped me over the past few years. I hope that I have remembered you all. Starting at the beginning I'd like to thank my family for supporting me when I decided that I'd like to do my PhD in Delft and through all the good and bad times that have followed. Four years simultaneously feels like an instant and an eternity, sometimes at the same time.

I'd also like to thank my co-promoter Erik van der Kolk for all his help over the past four years and his enthusiasm to keep things going, even when everything seemed to be going wrong.

I'd like to thank my promoter Pieter Dorenbos for his help, particularly on the more theoretical side of things. I can't count the many occasions when I came with what I thought was a simple problem and left with fewer misconceptions and a much better understanding of a subject!

Puck Brandhoff was my Masters student for over a year. We had many interesting conversations and got some good results together in the end. Thank you with putting up with my somewhat erratic supervision and good luck in your future career.

I would like to thank Dirk Poelman, Philippe Smet and the other people in Lumilab in the University of Ghent. I visited there twice and both times I was struck by how nice it was. I don't think that I would have made much progress on SmS without your help.

Anneke Delsing at Eindhoven University of Technology gave me a lot of help with both making and understanding the Europium oxynitrides. It has been a real pleasure to work with you. Thanks should also go to Dr Bert Hintzen and the other members of the Energy Materials and Devices group for all their help

and friendliness over the last couple of years, particularly Zhijun Zhang who helped with the synthesis of the last few compounds.

In Delft I also received help from Herman Shreuders from Chemical Engineering regarding magnetron sputtering, while Marnix Wagemaker, Michel Steenvoorden and Kees Goubitz from FAME gave me invaluable help with XRD.

Johan de Haas is an excellent technician and remarkably patient: Thanks! Thanks also go to Jose Buurman and Thea Miediema for all their friendliness and help.

It's been great to work with Michiel de Jong although I imagine that we'll both be glad to not have to clean the Sm_2S_3 gun again!

I would also like to thank all my colleagues in RD&M, the current ones: Mischa, Ivan, Marc, Wei-Wei, David, Pieter Vassier, Romee, Christina, Alice, Candice, Tony, Anna, Patricia, Valerio, Giacomo, Stefan, Herman, Melvin, Francesco, Marlies, Rob, Brendan, Frans, John, Jan Huizinga, Adrie, Jakob and Dennis, and those that have now gone: Jan Heemskerk, Ola, Alistair, Victor, Andreas, Lorette, Sam, Martijn, Gustavo, José, Femke, Wendy, Davy, Jan-Willem and Diederick. I hope that I haven't missed anybody! If I have it's only because of my awful memory for names. It is a pleasure to know or to have known you all!

I should also thank the members of PNR for accepting, or at least not complaining about, me on many social occasions, as well as all the other people who I have met in the Koepeltje, past and present.

Erik van der Kolk translated the summary and Juriaan Peeters translated my propositions, without which I would not have a thesis. Thank you both, I am very grateful.

Finally I'd like to thank Stuart for putting up with me for the last three-and-a-bit years. Your support has kept me going and I hope that it has been as wonderful for you as it has been for me. I remember an email that you sent me where you (jokingly) said: "The reactor physicists of TU Delft are committed, driven individuals who strive for long hours every day to ensure a safe and clean energy future for the entire world. They are an international group, with the English members in particular being worthy of extra pay, hugs and chocolate cake. One cannot fail to be impressed by their devotion to their work, charm and rugged good looks." So, chocolate cake then?

List of Publications

*E. Rogers, P.F. Smet, P. Dorenbos, D. Poelman, E. van der Kolk, Thermally induced metal-semiconducting phase transition of Samarium Monosulphide (SmS) thin films, Journal of Physics: Condensed Matter, **22**, 015005, 2010*

*E. Rogers, P. Dorenbos, E. van der Kolk, Systematics in the optical and electronic properties of the binary lanthanide halide, chalcogenide and pnictide compounds – an overview, New Journal of Physics, **13**, 093038, 2011*

*E. Rogers, P. Dorenbos, J.T.M. de Haas, E. van der Kolk, Experimental study of the $4f^n \rightarrow 4f^n$ and $4f^n \rightarrow 4f^{n-1}5d^1$ transitions of the Lanthanide Diiodides LnI_2 (Ln = Nd, Sm, Eu, Dy, Tm, Yb), Journal of Physics: Condensed Matter, **24**, 275502, 2012*

E. Rogers, E. van der Kolk, Selective deposition of metallic or semiconducting Sm_xS thin films by the RF magnetron co-sputtering of Sm_2S_3 and Sm-metal, submitted to: Thin Solid Films

Curriculum Vitae

Edith Grace Rogers was born in Newtown, Powys, in the United Kingdom, on the 28th September 1985 and was brought up in Garthmyl, Powys. She was educated at Berriew Country Primary School and Bishop's Castle Community College.

Between 2004 and 2008 she studied for a Master of Physics at Aberystwyth University, where she did a final Masters project on Surface Enhanced Ramen Spectroscopy using gold and silver colloidal solutions, obtaining a 2:1 degree.

Since 2008 she has been studying for a PhD at the Radiation, Detection and Medical Imaging section of the Radiation, Radionuclides & Reactors Department of Delft University of Technology, the results of which are presented in this thesis.